Transformation of iron oxide and hydroxide phases and its effects on contaminant mobility

A dissertation submitted in partial fulfillment
of the requirements for the degree of
Doctor of Philosophy in Engineering

by

PAUL CLARENCE MAGDAEL FRANCISCO

Division of Sustainable Resources Engineering
Graduate School of Engineering, Hokkaido University, Japan

September 2016

Transformation of iron oxide and hydroxide phases and its effects on contaminant mobility

Paul Clarence M. Francisco
Environmental Geology Laboratory
Graduate School of Engineering
Hokkaido University

ABSTRACT

Iron oxides and hydroxides [iron (hydro)oxides] are one of the most common phases in the earth's crust. Due to their ubiquity in the natural environment, they have long been recognized for their ability to regulate the concentrations of hazardous elements in nature. Furthermore, the relative ease with which they can be synthesized under controlled conditions has made them attractive materials for industrial applications like water-treatment and contaminant remediation. The feasibility of iron (hydro)oxides as long-term sinks for contaminants both in nature and in engineered environments depend on their behavior during phase transformation. In this work, the effects of foreign ligands on the transformation behavior of iron (hydro)oxides as well as on the behavior of contaminants were investigated.

Chapter 1 reviews the literature on the general properties of iron (hydro)oxides, their distributions, recognized applications as well as current knowledge on transformation mechanisms. In this chapter, the factors governing iron (hydro)oxide transformation and contaminant transport are identified.

Chapter 2 focuses on the effects of Si, one of the most common ligands present in the natural environment on the transformation kinetics of ferrihydrite. In this work, it was observed that even a small amount of Si significantly retards the crystallization of both goethite and hematite. This work provides new insights on the impacts of Si on ferrihydrite solubility as well as on the morphology of goethite and hematite. New quantitative data on transformation rates as well as activation energies are also presented in this chapter, which may be useful in predicting the crystallization behavior of goethite and hematite in alkaline environments (e.g. high-level waste disposal repositories).

Chapter 3 focuses on the behavior of selenite taken up by ferrihydrite during the crystallization of goethite and hematite, a contaminant originating from weathering of sedimentary rocks as well as from high-level wastes. In this work, a fraction of the selenite co-precipitated with ferrihydrite was released during transformation, with another fraction becoming immobilized within the crystalline phases. A combination of chemical extraction experiments as well as diffraction and spectroscopic studies show that the retention mechanism involves the incorporation of selenite within the crystalline phases. The findings presented in this chapter provides insights that can be used to predict the behavior of selenite or other contaminants during the evolution of iron (hydro)oxide sorption substrates.

Drawing from the insights presented in Chapters 2 and 3, Chapter 4 focuses on the effect of Si on the behavior of selenite during ferrihydrite transformation. The retardation of transformation by Si results in the retardation of selenite release back into solution. Furthermore, the presence of Si results in the release of more selenite back into solution. These observations are attributed to the competitive effect of Si for uptake sites on iron (hydro)oxide surfaces.

This work presents important insights on the stability of iron (hydro)oxides and their capability to retain contaminants in the presence of other elements. These findings may be useful in a broad range of contexts, such as on the behavior of iron (hydro)oxides in nature and in engineered environments.

ACKNOWLEDGEMENTS

Five years of graduate school in Japan has been definitely one of the most exciting and challenging chapters of my life and many people have supported me in this memorable journey. First, I would like to extend my deepest gratitude to my supervisor, Prof. Tsutomu Sato for accepting me to be part of his group and for supporting me through the difficulties of graduate school. All of the success and experiences that I earned during my time as a graduate student are largely due to his unwavering patience and guidance. I am also grateful that he gave me free rein to decide the course of my research, allowing me to develop the necessary initiative and skills as an independent scientist. Another person I would like to thank is my co-supervisor, Dr. Tsubasa Otake. Not only did I get useful technical advice from him, I also learned a lot about the more philosophical aspects of research from him, which helped me develop a better understanding of science and its broader implications. These two men helped me understand my research from the tiniest details to the biggest pictures, the kind of thinking that will undoubtedly help me in my career.

Some of the work that I did during the course of this PhD was done outside of the lab. I wish to thank Dr. Masami Fukushima for access to the FTIR. Dr. Keisuke Fukushi (Kanazawa University) for letting me stay in his lab for a week to do ATR-FTIR experiments. Dr. Takeshi Kasama (Technical University of Denmark) for analyzing my samples using TEM, which contributed to the publication of my first paper. Dr. Shinichi Suzuki, Dr. Hideaki Shiwaku, Dr. Toru Kobayashi and Dr. Tsuyoshi Yaita (JAEA) for giving me XAS machine time at SPring-8.

I am also grateful to Prof. Roy Wogelius and Dr. Arjen van Veelen (University of Manchester) for letting me work in their lab for two months. A huge part of this work was realized using the spectroscopic techniques that I learned from them, particularly about XAS.

I also wish to thank the past and current members of the Environmental Geology Laboratory who have contributed to my growth, both as a scientist and as a person. Ms. Yurie Ozaki, my first *kohai* (and to a lesser extent Ms. Misato Shimbashi and Mr. Jeehyun Yang), has given me an opportunity to be a mentor and pass on whatever knowledge I may have. I want to say that as much as learning from me, I also learned a lot from her (not least of which is patience). I also wish to thank Mr. Yu Arai and Ms. Kanako Toda for filling in my own shortcomings as a mentor to Ozaki. Others members are also acknowledged for providing essential experimental support (like ordering). Finally, I would like to thank Ms. Akane Ito.

I am extremely grateful to Ms. Yoshie Hoshi for her patience in helping me handle everything from administrative procedures, endless paperwork and matters of an emotional nature; she has no idea how much she has kept me sane. I also should not forget the women of L Building (formerly): Ms. Shoko Nozawa, Ms. Junko Hasegawa and Dr. Kumiko Kinoshita, essentially the mothers to the unruly kids in the lab, for providing much needed experimental support (plus coffee, sweets and the occasional levity). I also wish to thank Dr. Yoko Ohtomo, for helping me write my first paper, for reviewing my dissertation defense and for sage advice on what constitutes good beer. I wish to thank the women at the International Affairs Office: Ms. Natalya Shmakova, Ms. Mami Kaneta, Ms. Shizuko Kudo and Ms. Ayaka Ito for their assistance on matters related to graduate school and scholarship issues (and for kindly pestering forgetful students, like me, about deadlines).

I am also greatly indebted to the Filipino community at Hokkaido University. In particular, I want to thank Dr. Carlito Tabelin for helping me navigate the curiosities of this place and for letting me disturb him for the occasional, but necessary, chat (or rant). I am grateful for having people with whom I can share the hardships of graduate school and for always providing a taste, literally and figuratively, of home.

Finally, I would like to thank my family, whose emotional support and prayers helped me overcome the loneliness, the doubt and the challenges that come with studying in a foreign land. This work is dedicated to them.

My stay at Hokkaido University would not have been possible without assistance from the Ministry of Education, Culture and Sports (MEXT) of the Japanese Government.

TABLE OF CONTENTS

LIST OF TABLES

Chapter 2

Chapter 3

LIST OF FIGURES

Chapter 2

Chapter 3

Chapter 4

CHAPTER 1: General Introduction

1.1. Background

1.1.1. The Iron Oxides and Hydroxides

Iron oxides and hydroxides (hereafter referred to as iron (hydro)oxides) are one of the most common natural and synthetic compounds found on the earth's surface. Iron, being one of the most abundant elements in the earth's crust, is supplied into the surface via magmatic processes. Initially, iron phases are formed during chemical weathering of magmatic rocks in both terrestrial and aquatic environments (Cornell and Schwertmann, 2003). Reactions with water and O_2 results in the formation of dissolved aqueous species of Fe^{2+} and Fe^{3+} as well as solid iron (hydro)oxides. These phases can be observed in a wide range of environments, from terrestrial to marine environments, because of redistribution via physical and chemical processes (Cornell and Schwertmann, 2003).

Due to their ubiquity, iron (hydro)oxides play an important role in environmental and biological processes. For example, as strong sorbents, they regulate the concentrations of nutrients and contaminants soils, aquifers and streams (Cornell and Schwertmann, 2003). Furthermore, the solubility and reactivity of iron (hydro)oxides also control the concentration of bioavailable iron, especially in aquatic environments. As an important nutrient for plants and microorganisms, iron participates in cellular processes such as photosynthesis and nitrogen fixation (Perez-Guzman et al., 2010).

Apart from their wide distribution in the natural environment, iron (hydro)oxides also occur as products of aerobic corrosion of steel, which is used in a wide range of industrial or practical applications (Hazan et al., 2013). Corrosion occurs by a series oxidation-reduction processes that results in the production of aqueous metal species and the precipitation of these species into

insoluble iron (hydro)oxide phases. The formation of these phases may compromise the structural integrity of steel.

Iron (hydro)oxides occur in a broad range of structures and crystallinities. For example, the phases investigated in this research (2-line ferrihydrite, goethite and hematite) have significant variations in their structural, physical and chemical properties, resulting in widely different reactivities. These differences translate to differences in the capabilities of iron (hydro)oxides to sequester and retain environmentally important nutrients and contaminants.

1.1.2. Transformation of Iron (Hydro)oxides

Interconversion between different phases are common among iron (hydro)oxides and is dictated by both chemical conditions as well as kinetic and thermodynamic constraints. Transformations between different iron (hydro)oxides play a significant role in important environmental processes, such as the geochemical cycling of essential nutrients (e.g. phosphates) and hazardous elements (e.g. heavy metals) in diverse environments (Cudennec and Lecerf, 2006). In industrial settings, the transformation of iron phases is utilized in the production of such materials as pigments and is important in understanding changes in material properties of steel used in large-scale industrial applications (Cornell and Schwertmann, 2003).

Transformation of iron (hydro)oxides proceed by different pathways depending on chemical conditions, leading to different end products. Transformation pathways may be reconstructive, where the precursor phase is dissolved and a new phase precipitates or topotactic, where transformation proceeds within the solid phase (Cornell and Schwertmann, 2003). Reconstructive transformation pathways are driven by the solubility of the original phase and are therefore mediated by aqueous solutions. Thus, these pathways are the most commonly observed in nature and exert the most influence on environmental processes.

As an example, the aqueous transformation of poorly crystalline 2-line ferrihydrite to crystalline goethite proceeds by the dissolution of the ferrihydrite followed by the precipitation of goethite (Schwertmann and Murad, 1983). This transformation pathway occurs across a wide range of pH conditions but is favored at high pH conditions, under which ferrihydrite solubility is high (Schwertmann and Murad, 1983), or by the presence of Fe(II) ions, which promotes reductive dissolution of the ferrihydrite structure (Yee et al., 2006). On the other hand, transformation to hematite involves the aggregation and dehydration of ferrihydrite, a pathway that proceeds more readily under circum-neutral conditions and high temperatures (Cornell and Schwertmann, 2003).

The presence of other ions with strong affinities for iron (hydro)oxides is known to modify the reactivity of Fe-(hydro)oxide and their transformation pathways. For example, the presence of Al, which can be structurally incorporated by isomorphous substitution for Fe, reduces the reactivity of iron (hydro)oxides (Cornell and Schwertmann, 2003). Other ions, such as SO_4^{2-} and PO_4^{3-}, modify the morphology of resulting transformation products by selectively adsorbing on specific surfaces (Shaw et al., 2005; Tan et al., 2012). The presence of foreign ions, therefore, exerts significant influence on the properties of iron (hydro)oxides, which may modify their capacity to sequester and retain hazardous anions.

In most natural environments, one of the most common impurities associated with iron (hydro)oxides is Si, which is derived primarily from the weathering of silicate-rich rocks (Gallinari et al., 2002; Cornelis et al., 2011). Si is known to have a strong affinity to poorly crystalline iron (hydro)oxides (e.g. ferrihydrite), affecting their particle sizes (Dyer et al., 2010; Cismasu et al., 2014) and their surface reactivity (Anderson and Benjamin, 1985). Si has also been shown to stabilize poorly crystalline phases against transformation, leading to their long-term persistence in the natural environment (Cornell et al., 1987). Furthermore, due to its influence on ferrihydrite surface properties, Si also modifies the transformation pathways of ferrihydrite, resulting in the suppression of goethite and apparent promotion of hematite crystallization (Francisco et al., 2016).

1.1.3. Uptake of Hazardous Ions by Iron (Hydro)oxides

Due to their abundance, high surface reactivities, and affinity for ions, iron (hydro)oxides are well known to be particularly excellent sinks for various nutrients as well as environmental contaminants (Cornell and Schwertmann, 2003). Macroscopic geochemical studies have shown iron (hydro)oxides to be favorable sinks for hazardous anionic species such as AsO_3^{3-}, AsO_4^{3-} (e.g. Randall et al., 2001; Fukushi et al., 2003; Das et al., 2011), CrO_4^{2-} (e.g. Ding et al, 2000), PO_4^{3-} (e.g. Persson et al., 1996; Shaw et al., 2005), SeO_3^{2-} and SeO_4^{2-} (e.g. Zhang and Sparks, 1990; Su and Suarez, 1999; Rovira et al., 2008). Thus, iron (hydro)oxides have a strong potential to immobilize and control the concentrations of these environmentally important substances in natural waters (Stipp et al., 2004).

The uptake of ions by iron (hydro)oxides proceed by two main pathways, adsorption and co-precipitation (Crawford et al., 1993). Adsorption is defined as the accumulation of solutes (adsorbate) at the interface between a solid (adsorbent) and solution (Drever, 1997). There are two main modes of adsorption. Non-specific or outer sphere adsorption is mainly characterized by electrostatic interactions between adsorbates (e.g. SeO_4^{2-}, NO_3^- and ClO_4^-) and the solid surface, and is thus influenced by the ionic strength of the system. In such cases, adsorbates retain their hydration spheres, with at least one water molecule present between the adsorbate and the adsorbent. Specific or inner sphere adsorption, on the other hand, involves direct chemical bonding between the adsorbate (e.g. SeO_3^{2-}, AsO_3^{3-}, SiO_4^{4-}, PO_4^{3-}) and a metal on the solid surface, making such species less susceptible to desorption (Cornell and Schwertmann, 2003). Depending on the ion and the structure of the solid surface, spectroscopic studies have shown that the mode of attachment may vary. For example, bidentate-mononuclear complexes occur on the edges of Fe octahedra, while bidentate-binuclear complexes occur at the corners of two adjacent Fe octahedra (Manceau, 1995).

Co-precipitation with iron (hydro)oxides occurs when an anionic species is present in the same solution as the carrier element (i.e. Fe). When Fe hydrolyzes to form an iron (hydro)oxide, the anion is sequestered from solution by iron (hydro)oxide precipitates (Lu et al., 2011). Ions adsorb on incipient particles with large specific surface areas that then continue to grow over the course of the precipitation process, becoming trapped within and in between growing particles (Kelly et al., 2008; Lu et al., 2011). While co-precipitation has been found to be more effective at sequestering ions from solution compared to adsorption (Crawford et al., 1993; Lu et al., 2011), the molecular structure of anionic species co-precipitated with iron (hydro)oxides is poorly understood. Previous studies on the co-precipitation of As(V) with ferrihydrite have shown As to be present as bidentate complexes on the edges of Fe octahedra (Waychunas et al., 1992), where it retards the polymerization of ferrihydrite to more crystalline phases.

1.1.4. Impact of Iron (Hydro)oxide Transformation on the Uptake and Retention of Hazardous Ions

The utility of iron (hydro)oxide phases as long-term and stable sinks for hazardous ions in natural and engineered environments depend strongly on their ability to retain previously sequestered ions during phase transitions (Stipp et al., 2004). The conversion of one iron (hydro)oxides phase to another entails changes in the morphology, crystal structure and hence, in the potential for retention of contaminants (Bazilevskaya et al., 2012). This may result in the remobilization of contaminants that have been previously taken up by the original phase. However, delaying or inhibiting the transformation of iron (hydro)oxides may efficiently immobilize contaminants over longer durations.

Currently, there is very limited understanding of the behavior of certain anions during iron (hydro)oxide transformation. In particular, it is not known which transformation pathways favor the release or retention of hazardous ions. Ferrihydrite transformation to goethite, which readily proceeds at alkaline conditions, involves the dissolution of the ferrihydrite structure (Cornell and

Schwertmann, 2003). This may result in the release of ions that may have been incorporated within or adsorbed on ferrihydrite. On the other hand, pathways that do not involve dissolution, such as transformation to hematite may potentially allow the retention of associated ions in the transformation products. Studies on the fate of co-precipitated As(V) with ferrihydrite have shown the As(V) is expelled from the solid phase during aging and transformation (Waychunas et al., 1992). On the other hand, recent studies on U and Pb behavior (e.g. Vu et al., 2013; Marshall et al., 2014) have shown that these elements may be incorporated during transformation to hematite by being incorporated in the crystal structure or trapped between particle aggregates.

Furthermore, the presence of ions that are strongly associated with iron (hydro)oxides may also impact the behavior of previously taken up hazardous ions. For example, Si, which is known to retard ferrihydrite transformation and adsorb strongly on iron (hydro)oxide surfaces, may inhibit remobilization but may also limit the retention of hazardous ions. The presence of other strongly adsorbing ions such as phosphates may also produce similar effects.

1.1.5. Iron (Hydro)oxides in Engineered Environments

Apart from being important in natural environments, iron (hydro)oxides are also important components of many engineered environments. For example, treatment of waste discharges from municipal incinerators and electric power stations involve uptake of contaminants such as As, Se and heavy metals by processes such as co-precipitation (e.g. Merrill et al., 1987; Lundtorp et al., 2002). In waste disposal and groundwater remediation environments, reactive barriers consisting of metallic Fe are used for the *in situ* remediation of contaminated groundwater via coupled oxidation of metallic Fe and reduction of redox-sensitive contaminants such as Cr, Tc and U (Cantrell et al., 1995). The oxidation of metallic Fe results in the formation of iron (hydro)oxides that may also serve as additional sorption substrates for contaminants.

One of the engineered environments where iron (hydro)oxides are expected to play important roles is in the geological disposal of radioactive wastes. In these environments, the release of radionuclides (e.g. Se, U, Tc, etc.) from waste packages may be attenuated by uptake of these elements onto iron (hydro)oxides (e.g. Bargar et al., 1999; Jordan et al., 2009; van Veelen et al., 2015). For example, in high-level waste (HLW) disposal environments, the intrusion of groundwater into the disposal system results in the corrosion of steel components of the repository as well as the release of radionuclides immobilized within the vitrified waste matrix. Aqueous iron ions directly derived from the corrosion of steel may co-precipitate with radionuclides released by glass dissolution. In the far-field regions of the repository, radionuclides that were not sequestered by co-precipitation may be immobilized by adsorption on iron (hydro)oxides present in the surrounding host rocks. The behavior of immobilized radionuclides, in turn, may be affected by transitions between different iron (hydro)oxide phases.

The behavior of radionuclides in geological disposal repositories are taken into account in predicting dose rates for long-term safety assessments of the repositories (REF). However, these estimates account only for the release of radionuclides from the waste form. Given the potential of iron (hydro)oxides as sinks for radionuclides, accurate safety cases need to account for the possible immobilization on iron (hydro)oxides. Furthermore, the effects of phase transformation on the behavior of these radionuclides must also be understood to build more reliable safety cases.

1.2. Objectives of this Study

The overall goal of this study is to understand the mechanisms of the transformation of poorly crystalline Fe-(hydro)oxide phases, specifically, ferrihydrite, to crystalline phases in the presence of Si as well as its effect on the mobility of hazardous anions. In particular, this study investigates the following issues: (1) the pathways involved in the transformation of ferrihydrite to crystalline phases at alkaline conditions; (2) how these pathways are modified in the presence of

foreign ligands; (3) the impact of transformation on the behavior of hazardous anions; (4) how foreign ligands (i.e. Si) affect the behavior of hazardous anions on the behavior of hazardous anions.

This investigation is limited to understanding transformation behavior in the fully oxidized Fe(III) system. In the context of radioactive waste disposal, such a case may represent a worst-case scenario involving the breach of the disposal environment by fully oxygenated groundwater. Furthermore, this may also represent cases of contamination in near surface environments. Investigations in oxidized environments may also serve as limiting cases to constrain the behavior of contaminants.

1.3. Dissertation Structure

This dissertation is divided into five chapters. Chapter 1 introduces iron (hydro)oxides and their role in natural and engineered environments. This chapter also lays out the framework of this dissertation.

Chapter 2 examines the effects of Si on the transformation kinetics of ferrihydrite, which is a typical precursor phase for crystalline phases such as goethite and hematite. In this chapter, phase evolution over time and in the presence of Si was investigated using powder X-ray diffraction. The results presented in this chapter have been accepted for publication in *American Mineralogist*.

Chapter 3 investigates the behavior of Se(IV) that was co-precipitated with ferrihydrite during its transformation to crystalline goethite and hematite. In this chapter, the influence of transformation pathways on the release or retention of Se(IV) was investigated by conducting experiments at different pH conditions and looking at the speciation of Se(IV) using macroscopic and spectroscopic techniques. A manuscript based on this chapter was submitted for publication to *Journal of Colloid and Interface Science*.

Drawing from the conclusions presented in Chapters 2 and 3, Chapter 4 investigates the influence of Si on the behavior of Se(IV) co-precipitated with ferrihydrite during its transformation to goethite and hematite.

Chapter 5 summarizes the insights obtained from the previous chapters and their implications on the behavior of contaminants in the natural environment. This chapter also proposes future directions for research.

1.4. List of References

Anderson, P.R., Benjamin, M.M. (1985) Effects of silicon on the crystallization and adsorption properties of ferric oxides. Environmental Science and Technology, 19, 1048-1053.

Bazilevskaya, E., Archibald, D.D., and Martinez, C.E. (2012) Rate constants and mechanisms for the crystallization of Al nano-goethite under environmentally relevant conditions. Geochimica Et Cosmochimica Acta, 88, 167-182.

Cismasu, A.C., Michel, F.M., Tcaciuc, A.P., and Brown, G.E. (2014) Properties of impurity-bearing ferrihydrite III. Effects of Si on the structure of 2-line ferrihydrite. Geochimica Et Cosmochimica Acta, 133, 168-185.

Cornelis, J.T., Delvaux, B., Georg, R.B., Lucas, Y., Ranger, J., and Opfergelt, S. (2011) Tracing the origin of dissolved silicon transferred from various soil-plant systems towards rivers: a review. Biogeosciences, 8(1), 89-112.

Cornell, R.M., Giovanoli, R., and Schindler, P.W. (1987) Effect of silicate species on the transformation of ferrihydrite into goethite and hematite in alkaline media. Clays and Clay Minerals, 35(1), 21-28.

Cornell, R.M., Schwertmann, U. (2003) The Iron Oxides: Structure, Properties, Reactions, Occurrences and Uses, 2nd ed., 703 p. Wiley-VCH, Weinheim.

Cantrell, K.J., Kaplan, D.I., Wietsma, T.W. (1995) Zero-valent iron for the in situ remediation of selected metals in groundwater. Journal of Hazardous Materials, 42, 201-212.

Crawford, R.J., Harding, I.H., Mainwaring, D.E. (1993) Adsorption and coprecipitation of single heavy metal ions onto the hydrated oxides of iron and chromium. Langmuir, 9, 3050-3056.

Cudennec, Y., and Lecerf, A. (2006) The transformation of ferrihydrite into goethite or hematite, revisited. Journal of Solid State Chemistry, 179(3), 716-722.

Das, S., Hendry, M.J., and Essilfie-Dughan, J. (2011) Effects of adsorbed arsenate on the rate of transformation of 2-Line ferrihydrite at pH 10. Environmental Science & Technology, 45(13), 5557-5563.

Ding, M., de Jong, B.H.W.S., Roosendaal, S.J., Vredenberg, A. (2000) XPS studies on the electronic structure of bonding between solid and solutes: adsorption of arsenate, chromate, phosphate, Pb^{2+}, and Zn^{2+} ions on amorphous black ferric oxyhydroxide. Geochmica et Cosmochimica Acta, 65, 1209-1219.

Drever, J.I. (1997) The Geochemistry of Natural Waters: Surface and Groundwater Environments, 3rd ed., 436 p., Prentice-Hall, New Jersey.

Dyer, L., Fawell, P.D., Newman, O.M.G., and Richmond, W.R. (2010) Synthesis and characterisation of ferrihydrite/silica co-precipitates. Journal of Colloid and Interface Science, 348(1), 65-70.

Francisco, P.C.M., Sato, T., Otake, T., Kasama, T. (2016) Kinetics of Fe(III) mineral crystallization in the presence of Si at alkaline conditions. American Mineralogist, in press, DOI:http://dx.doi.org/10.2138/am-2016-5589.

Fukushi, K., Sato, T., and Yanase, N. (2003) Solid-solution reactions in As(V) sorption by schwertmannite. Environmental Science & Technology, 37(16), 3581-3586.

Gallinari, M., Ragueneau, O., Corrin, L., DeMaster, D.J., and Treguer, P. (2002) The importance of water column processes on the dissolution properties of biogenic silica in deep-sea sediments I. Solubility. Geochimica Et Cosmochimica Acta, 66(15), 2701-2717.

Hazan, E., Sadia, Y., and Gelbstein, Y. (2013) Characterization of AISI 4340 corrosion products using Raman spectroscopy. Corrosion Science, 74, 414-418.

Lundtorp, K., Jensen, D.L., Sorensen, M.A., Mogensen, E.P.B., Christensen, T.H. (2002) Treatment of waste incinerator air-pollution-control residues with $FeSO_4$: Concept and product characterization. Waste Management and Research, 20, 69-79.

Manceau, A. (1995) The mechanism of anion adsorption on iron oxides: Evidence for the bonding of arsenate tetrahedra on free $Fe(O, OH)_6$ edges. Geochimica et Cosmochimica Acta, 59(17), 3647-3653.

Marshall, T.A., Morris, K., Law, G.T.W., Livens, F.R., Mosselmans, J.F.W., Bots, P., and Shaw, S. (2014) Incorporation of uranium into hematite during crystallization from ferrihydrite. Environmental Science & Technology, 48(7), 3724-3731.

Merrill, D.T., Manzione, M.A., Parker, D.S., Petersen, J.J., Chow, W., Hobbs, A.O. (1987) Field evaluation of arsenic and selenium removal by iron coprecipitation. Environmental Progress, 6(2), 82-90.

Persson, P., Nilsson, N., Sjoberg, S. (1996) Structure and bonding of orthophosphate ions at the iron oxide-aqueous surface. Journal of Colloid and Interface Science, 177, 263-275.

Randall, S.R., Sherman, D.M., Ragnarsdottir, K.V. (2001) Sorption of As(V) on greent rust ($Fe_4(II)Fe_2(III)(OH)_{12}SO_4 \bullet 3H_2O$) and lepidocrocite (γ-FeOOH): surface complexes with EXAFS spectroscopy. Geochimica et Cosmochimica Acta, 65, 1015-1023.

Rovira, M., Gimenez, J., Martinez, M., Martinez-Llado, X., de Pablo, J., Marti, V., and Duro, L. (2008) Sorption of selenium(IV) and selenium(VI) onto natural iron oxides: Goethite and hematite. Journal of Hazardous Materials, 150(2), 279-284.

Schwertmann, U., and Murad, E. (1983) Effect of pH on the formation of goethite and hematite from ferrihydrite. Clays and Clay Minerals, 31(4), 277-284.

Shaw, S., Pepper, S.E., Bryan, N.D., and Livens, F.R. (2005) The kinetics and mechanisms of goethite and hematite crystallization under alkaline conditions, and in the presence of phosphate. American Mineralogist, 90(11-12), 1852-1860.

Stipp, S., Hansen, M., Kristensen, R., Hochella, M.F., Jr., Bennedsen, L., Dideriksen, K., Balic-Zunic, T., Leonard, D., Mathieu, H.-J. (2002) Behaviour of Fe-oxides relevant to contaminant uptake in the environment. Chemical Geology, 190, 321-337.

Su, C., Suarez, D.L. (2000) Selenate and selenite sorption on iron oxides: An infrared and electrophoretic study. Soil Science Society of America Journal, 64, 101-111

Tan, W.F., Yu, Y.T., Wang, M.X., Liu, F., and Koopal, L.K. (2014) Shape evolution synthesis of monodisperse spherical, ellipsoidal, and elongated hematite (alpha-Fe_2O_3) nanoparticles using ascorbic acid. Crystal Growth & Design, 14(1), 157-164.

Vu, H.P., Shaw, S., Brinza, L., Benning, L.G. (2013) Partitioning of Pb(II) during goethite and hematite crystallization: Implications for Pb transport in natural systems. Applied Geochemistry, 39, 119-128.

Yee, N., Shaw, S., Benning, L.G., and Nguyen, T.H. (2006) The rate of ferrihydrite transformation to goethite via the Fe(II) pathway. American Mineralogist, 91(1), 92-96.

Zhang, P., Sparks, D.L. (1990) Kinetics of selenate and selenite adsorption/desorption at the goethite/water interface. Environmental Science and Technology, 24, 1848-1856.

CHAPTER 2: The effects of Si on the aqueous transformation of Fe(III) minerals at alkaline conditions

Part of this chapter has been accepted for publication in *American Mineralogist* as:

P.C.M. Francisco, T. Sato, T. Otake, T. Kasama (2016) Kinetics of Fe(III) mineral crystallization from ferrihydrite in the presence of Si at alkaline conditions, in press, DOI: http://dx.doi.org/10.2138/am-2016-5589

2.1. Introduction

Fe(III) hydroxide and oxide phases such as goethite (α-FeOOH) and hematite (α-Fe_2O_3) are widely distributed in different natural (e.g. soils, sediments) and engineered environments (e.g. geological waste disposal, water treatment technologies). Due to their high surface areas and surface reactivity, these phases have excellent sorption capacities for anions (e.g. sulfate, phosphate, arsenate, etc.), metals (e.g. Pb, Cu, Ni) as well as organic compounds, exerting significant controls on the transport and availability of these substances (Cornell and Schwertmann, 2003).

In engineered environments such as deep geological repositories for high-level nuclear wastes, initially reducing conditions may eventually give way to more oxidizing conditions in the long-term due to influx of oxygenated groundwater. In such cases, poorly ordered Fe(II,III) hydroxysalts, ferrihydrite, goethite and hematite are among a suite of corrosion products expected to form during aqueous corrosion of important steel components of the repository, such as the steel overpack (Refait et al., 2003; Kwon et al., 2007; Hazan et al., 2013). In Japanese disposal concepts, the use of cement as structural liners for tunnels, as mechanical support for the backfill and as grouting material for fractures arising from the country's active geologic setting (NUMO, 2004b) is expected to generate alkaline fluids around the repository. A breach in the canister, coupled with the presence of alkaline fluids, could result in the dissolution of vitrified waste and the release of high-yield radionuclides (e.g. U, Se, Tc) into the wider environment. Formation of Fe(III) phases from steel corrosion, however, may provide a sink for these elements, which exist as oxyanions, via adsorption and/or co-precipitation (e.g. Bargar et al., 1999; Rovira et al., 2008; Marshall et al., 2014). In particular, ferrihydrite, a poorly ordered Fe-oxyhydroxide that forms by the hydrolysis of

Fe(II) and Fe(III) ions (Cudennec and Lecerf, 2006; Dyer et al, 2010), has exhibited superior sorption properties for these elements due to its high specific surface area (Das et al., 2013). In aqueous systems, oxide phases such as goethite and hematite typically crystallize via the transformation of the metastable and poorly ordered intermediate phase ferrihydrite. Crystallization of goethite and hematite, however, may potentially modify the ability of corrosion products to scavenge hazardous metals from solution due to differences in surface area and reactivity (Buekers et al., 2008; Bazilevskaya et al., 2012).

The crystallization mechanisms of goethite and hematite from ferrihydrite in aqueous systems involve mutually exclusive and competitive processes that depend on parameters such as pH and temperature. Goethite forms through direct nucleation from aqueous solutions following the dissolution of the ferrihydrite precursor. Under high pH conditions (pH > 10), this crystallization mechanism is pronounced due to the increased solubility of the ferrihydrite precursor and the high concentration of $Fe(OH)_4^-$ species favorable for goethite crystal growth (Schwertmann and Murad, 1983). On the other hand, hematite crystallization proceeds by the aggregation, dehydration and solid-state transformation of ferrihydrite particles. This transformation pathway is promoted at higher temperatures, which favor dehydration and at near neutral to mildly alkaline (pH < 10) conditions, under which ferrihydrite particles tend to aggregate (Cudennec and Lecerf, 2006).

The kinetics of crystallization of goethite and hematite from ferrihydrite at alkaline conditions and in the absence of foreign compounds has been investigated extensively, such that there is abundant quantitative data available. Data obtained from studies on Fe-oxide color change at 40°C to 85°C show that apparent activation energies for goethite crystallization are 56.1 kJ/mol and 48.2 kJ/mol at pH 11.7 and 12.2, respectively (Nagano et al., 1994). More recent in-situ crystallization experiments at pH 13.7 under a broader range of temperatures (60°C to 132°C) obtained a value of 39 kJ/mol (Shaw et al., 2005). These kinetic data show that goethite crystallization is favored by increasing pH. For hematite, the availability of kinetic data across a broad pH range is more limited. Data obtained using phase quantification at pH 10 and at 25°C to

100°C estimate the apparent activation energy for hematite crystallization at 65 kJ/mol (Das et al., 2011a) while in-situ crystallization experiments at pH 10.7 and at 72°C to 137°C give a value of 69 kJ/mol (Shaw et al., 2005).

However, at the interface of the corroding steel and dissolving glass, dissolved Si may co-precipitate with and/or adsorb onto immediate corrosion products such as ferrihydrite. Early investigations have recognized that Si alters the transformation rates of ferrihydrite. Studies on solids formed from the oxidation of Fe(II) in solution showed that Si inhibited the formation of crystalline lepidocrocite and favored the formation of ferrihydrite (Schwertmann and Thalmann, 1976). Solubility studies showed that ferrihydrite formed in the presence of Si has decreased solubility in oxalate, suggesting that Si stabilizes ferrihydrite (Karim, 1984). These findings are consistent with more systematic kinetic studies that showed the degree of transformation of ferrihydrite to crystalline goethite, which is represented by the ratio of oxalate extractable Fe to the total Fe (Fe_o/Fe_t), decreases with increasing Si (Cornell et al., 1987). The mechanism of inhibition is generally thought to be the deposition of Si on the surfaces of ferrihydrite (Cornell et al., 1987; Vempati and Loeppert, 1989; Doelsch et al., 2001; Swedlund et al., 2009; Dyer et al., 2010), which may render ferrihydrite particles less soluble and less susceptible to aggregation. These studies collectively show that Si inhibits the transformation of ferrihydrite and delays the crystallization of more stable phases, potentially providing a long-term stable sink for radioactive elements released from the glass. While the qualitative effect of Si on the formation of crystalline Fe(III) phases is well known, there is however, paucity in quantitative kinetic data that may be useful in formulating predictive models and building a robust safety case for high-level radioactive waste (HLW) repositories.

The goal of this study is to obtain quantitative kinetic data for the crystallization of goethite and hematite as a function of Si co-precipitated with Fe(III) at alkaline conditions and relate them with their known formation mechanisms. In this study, we conduct the experiments at pH 10 for two main reasons. First, the use of bentonite in Japanese designs as backfill between the overpack

and the host rock (JNC, 2000; NUMO, 2004a) may buffer the pH of potential hyperalkaline fluids that may interact with the glass and steel to approximately 9 to 10 (Savage et al., 2002). Second, at pH 10 the solubility of silica begins to increase (Stumm and Morgan, 1996), such that the effects of Si on Fe(III) crystallization cannot be discounted. In addition, we also conduct the experiments in the presence of nitrates, as nitrates are principal components in Japanese groundwaters (Kumazawa, 2002). Furthermore, nitrates are also present in significant amounts in disposal systems for other waste classes such as trans-uranic (TRU) wastes (JAEA, 2007). While data obtained in this study is useful for developing safety cases for nuclear waste repositories, insights into the mechanisms involved may also be used to understand the effect of Si in natural environments.

2.2. Materials and Methods

2.2.1. Synthesis

Fe(III)) solution was prepared by dissolving reagent grade $Fe(NO_3)_3 \bullet 9H_2O$ (Kanto, 99%) in ultrapure water (18 M Ω •cm) to create a 0.05 mol/L solution. Appropriate amounts of tetraethylorthosilicate (TEOS; Alfa Aesar, 98%) were then added to the Fe solution to achieve Si concentrations of 0 (Si/Fe = 0) to 1.25 x 10^{-3} mol/L (Si/Fe = 0.025). Preliminary experiments using a broader range of Si concentrations showed that crystallization of goethite and hematite only proceeded at timescales short enough to be investigated in the laboratory at these Si concentrations.

The Si-Fe mixture was stirred for about 30 minutes to dissolve the TEOS completely before pH adjustment. The initial pH of the mixture was about 1.8, which was then adjusted to about 10.0±0.1 by titrating the solution with NaOH (Kanto, 97%). Addition of base hydrolyzed the Fe(III) in solution, forming dark brown precipitates. The slurries were stirred for an additional 15 minutes to allow the pH to stabilize. The slurries were then equally divided into 50 mL polypropylene bottles and then stored at ovens preheated to 50, 60, 70 and 80°C to induce crystallization. Samples

extracted at different reaction durations were washed with deionized water to remove the salts and freeze-dried for at least 24 hours. Selected samples from different temperatures and Si concentrations were replicated to check the reproducibility of the results.

2.2.2. Characterization of Synthetic Products

Samples were analyzed by powder x-ray diffraction (XRD) using a Rigaku RINT2000 x-ray diffractometer operating at 40 kV and 40 mA, equipped with a Cu target and graphite monochromator. Samples were mixed with approximately 20 wt. % α-Al_2O_3 (Baikowski, CR-1 grade; crystallinity: 85%) to serve as an internal standard for phase quantification. The mixtures were finely ground to minimize micro-absorption effects. Diffraction profiles were collected from 10 to 70° 2θ.

FTIR spectra were collected from 400 to 4000 cm^{-1} on a JASCO FTIR-4100 spectrometer with 1.0 cm^{-1} spectral resolution. Pellets were prepared by mixing and crushing the samples with KBr at a 1.5 mg sample: 250 mg KBr ratio. The KBr used to prepare the samples was heated at 110°C for two hours prior to use to remove the water.

To determine the zeta potential of the initial precipitates at pH 10, powders of fresh precipitates were dispersed in a $NaNO_3$ medium set at pH 10 and an ionic strength of approximately 0.15 M, which is similar to the ionic strength of the parent solution from which they were precipitated. The dilute precipitates are then transferred to a clear folded capillary cell and analyzed using a Malvern Zetasizer Nano-ZS90. The values reported in this study are taken as the average of up to 20 measurements, each consisting of 100 runs.

Selected samples were characterized using an FEI 80-300ST Titan transmission electron microscope (TEM) operated at 300 kV, in order to study the morphology of individual mineral particles. The lightly crushed samples were placed directly onto Cu TEM grids and mounted on a low-background beryllium TEM specimen holder. Annular dark-field (ADF) imaging and energy

dispersive x-ray spectroscopic (EDS) elemental mapping was performed in scanning TEM mode using an Oxford X-Max^N silicon drift detector equipped to the TEM. Each EDS spectrum was acquired with a dwell time of 3 seconds in steps of 15 nm and was processed by principal component analysis and pixel-by-pixel background subtraction (Kasama et al., 2015).

2.2.3. Quantification of Fe(III) Phases

To determine the proportion of phases in the samples, powder XRD data were refined by the Rietveld refinement method using the commercial SIROQUANT program (Taylor and Clapp, 1992). Rietveld refinement uses a non-linear least squares fitting approach to minimize the difference between observed and calculated XRD patterns. The parameters refined for this study include the half-width parameters, instrument zero, unit-cell parameters, asymmetry factors and the influence of preferred orientation and corrections were applied to account for the absorption contrast between α -Al_2O_3 and Fe-oxides. The quality of Rietveld refinement was evaluated from the values of χ^2 and R factor given by the results of the fitting.

The ferrihydrite content of the sample cannot be directly determined from Rietveld refinement due to its poorly crystalline nature. Treating it as an amorphous phase, its proportion was estimated using the internal standard method, where the proportion of an amorphous phase is related to the overestimation of the known internal standard, in this case α-Al_2O_3, defined by:

$$Fh(\%) = \frac{100}{100 - W_s}\left\{100\left(1 - \frac{W_s}{R_s}\right)\right\} \quad (1)$$

where W_s (%) is the weighted percentage of the internal standard and R_s (%) is its Rietveld measured percentage (De la Torre et al., 2001; Westphal et al., 2009). To account for the presence of an amorphous fraction in the internal standard, a modified form of Equation (1) is given by:

$$Fh(\%) = \frac{100}{100 - W_s}\left\{100\left(1 - \frac{W_{s,ct}}{R_s}\right) - W_{s,am}\right\} \quad (2)$$

where $W_{s,ct}$ (%) is the crystalline weight fraction of the standard, while $W_{s,am}$ (%) is its amorphous weight fraction, was used. The uncertainty of the derived amorphous content was estimated from the uncertainty given by the Rietveld refinement multiplied by the slope of Equation (2) (Westphal et al, 2009).

2.2.4. Kinetic Analysis

The weighted percentages of each phase over time derived from the Rietveld refinements were normalized with the maximum percentage observed for a particular system to derive the degree of reaction, α, given by the following equation:

$$\alpha = \frac{X_t}{X_{\max}} \quad (3)$$

where X_t is the percentage at time t and X_{max} is the maximum percentage. The normalized data, plotted as function of time, were fitted with the general form of the Johnson-Mehl-Avrami-Kolmogorov (JMAK) model given by the equation (Avrami, 1939; 1940; 1941):

$$\alpha = 1 - e^{-k(t-t_0)^n} \quad (4)$$

where k is the rate constant (hr^{-1}), t is the time (hr), t_0 is the induction time and n is a parameter related to the dimensionality and mechanism of growth. The parameters k, t_0 and n were used as fitting parameters. The JMAK model has been previously utilized to describe crystallization reactions of proteins (e.g. Li and Nail, 2005), solid-solid transformation (e.g. Houston et al., 2009) and nucleation and growth (e.g. Shaw et al., 2005; Davidson et al., 2008)

Using data from experiments conducted at different temperatures, apparent activation energies of crystallization for each system were derived from the Arrhenius equation, given by:

$$\ln k = -\frac{E_{a(cryst)}}{RT} + \ln A \quad (5)$$

where $E_{a(cryst)}$ is the apparent activation energy for crystallization (kJ/mol), R is the gas constant (8.314 x 10^{-3} kJ/mol•K), T is the absolute temperature (K) and A is the pre-exponential factor (hr^{-1}). The apparent activation energies provide information about crystallization mechanisms.

2.3. Results

2.3.1. Characterization of Initial Precipitates

Regardless of Si/Fe, XRD analyses of the initial dark brown precipitates extracted before heating are characterized by two broad maxima centered at approximately 35° and 62° 2θ (Fig. 1), which are consistent with 2-line ferrihydrite. No significant shift or changes in the width of the ferrihydrite 'peaks' were observed in the range of Si concentration studied.

Infrared spectra for freshly precipitated solids extracted prior to heating are generally consistent with published data on ferrihydrite (Russell, 1979; Cornell and Schwertmann, 2003). Four distinct regions can be identified in the spectra (Fig. 2). First, the area from ~2400 to ~3500 cm^{-1}, dominated by a broad absorption band with a maximum at approximately ~3200 to ~3300 cm^{-1} corresponding to bulk OH stretching vibrations. The relatively high background, which masks other vibrations in this region, is attributed to strong IR scattering from small ferrihydrite crystallites (Vaughan et al., 2012). Second, the area from ~1300 to 1700 cm^{-1}, where relatively sharp absorption bands at ~1350, ~1480 and ~1650 cm^{-1} corresponding to the vibrations of adsorbed water are observed. From ~800 to ~1200 cm^{-1}, T-O-T and T-O stretching vibrations can be observed. The low frequency region between 400 to ~700 cm^{-1} is characterized by Fe-O stretching vibrations, O-T-O bending vibrations and bulk OH bending vibrations (Doelsch et al., 2003).

The most significant changes with increasing Si concentration are observed in the third region, where a relatively sharp band at ~930 cm^{-1} corresponding to asymmetric stretching

vibrations of Si-O-Fe bonds appears and increases in intensity with increasing concentration of Si. At Si/Fe = 0.025, a shoulder at ~1060 cm^{-1} is observed, suggesting the presence of a small amount of polymeric Si (Swedlund et al., 2010).

At pH 10, initial precipitates exhibit negative surface charge due to the presence of hydroxyl groups on particle surfaces. With increasing Si, the surface charge on the initial precipitates becomes more negative (Fig. 3). The silica-free precipitates have a zeta potential of approximately -16.6 mV. This decreases to approximately -21.0 mV at Si/Fe = 0.025.

2.3.2. Crystallization Experiments

During heating of the ferrihydrite slurry, the initial precipitates undergo transformation to the crystalline goethite (α-FeOOH) and hematite (α-Fe_2O_3) as indicated by distinct color changes and the appearance of sharp x-ray diffraction peaks corresponding to crystalline phases over time. The transformation is also accompanied by an increase in pH to approximately ~11.5.

XRD results show that at a given temperature, the time at which diffraction peaks appear varies with Si/Fe ratio. At 80°C, diffraction peaks are already present after 1 hour in the pure system (Si/Fe = 0; Fig. 4A). Diffraction peaks only begin to appear after 2 hours at Si/Fe = 0.025 (Fig. 4B). In addition, the time of appearance and intensities of goethite and hematite peaks vary with increasing Si/Fe. For example, in Fig. 4, goethite peaks are observed along with those of hematite in Si/Fe = 0 after 1 hour, suggesting that goethite and hematite may have begun crystallizing simultaneously. At Si/Fe = 0.025, the (101) peak of goethite at ~24° 2θ (the most intense observed in this study) only begins to appear faintly after 6 hours, while the first appearance of hematite peaks is confirmed in the sample after 4 hours. These observations suggest that crystallization becomes increasingly delayed with increasing amounts of Si, with goethite being delayed to a higher degree than hematite. Decreasing temperatures result in a later appearance of diffraction peaks. For example, while in Si/Fe = 0 diffraction peaks of hematite and goethite are

observed after 1 hour at 80°C (Fig. 4), peaks begin to be observed after 3 hours at 50°C (Supplementary Information, Fig. S1).

Results of the Rietveld refinement show χ^2 values and R factors of less than 10 and 1, respectively (Supplementary Information, Table S1), indicating the good quality of fits. In Si/Fe = 0, amorphous content calculation using equation (2) shows that the ferrihydrite is completely consumed after 2 hours. This coincides with the time at which the pH stabilizes and the distinct color change of the sample from dark brown to deep red, indicating the completion of the transformation (Supplementary Information, Fig. S2). Although there is considerable uncertainty in the amorphous content calculated from equation (2), particularly at low ferrihydrite contents due to the low proportion of internal standard (Westphal et al, 2009), the correspondence between the time at which the pH stabilizes and the time at which the calculated ferrihydrite content drops to 0 wt. % supports the accuracy of the calculated values. On the other hand, for Si/Fe = 0.025, the ferrihydrite does not disappear until after 10 hours. This is consistent with the increase in the percentage of residual ferrihydrite after 2 hours of heating with increasing Si/Fe ratios (Fig. 5A). This indicates that the overall conversion of ferrihydrite to more crystalline phases is retarded in the presence of increasing amounts of Si.

Depending on the Si/Fe ratio and temperature, the relative proportions of goethite and hematite in the final crystalline products also vary. As seen in Fig. 4, both goethite and hematite are present in the pure system at 80°C, with the intensities of hematite peaks being higher compared to those of goethite. At higher Si/Fe ratios, the intensities of hematite increase while those of goethite decrease, becoming negligibly low at Si/Fe = 0.025. The results of the Rietveld refinement show that the percentage of goethite decreases from ~22 wt. % in Si/Fe = 0 to ~0 wt. % in Si/Fe = 0.025, while that of hematite increases from ~78 wt. % to ~100 wt. % (Fig. 5B). With increasing temperatures, the percentage of hematite tends to increase at a given Si/Fe. For example, in Si/Fe = 0, hematite percentage increases from ~26 wt. % at 50°C to ~78 wt. % at 80°C.

Plots of the reaction progress parameter α (normalized percentages) for goethite and hematite as a function of time show that crystallization proceeds by an initial rapid increase followed by a plateau (Fig. 6). Fitting the time-resolved reaction progress data with the JMAK model yielded characteristic S-shaped curves. Best fits to the data were achieved at different *n* values. For example, in Si/Fe = 0, both hematite and goethite data can be fitted with *n* values at an average of 1.07 and 1.11, respectively. The *n* values tend to increase with increasing Si/Fe. For example, in Si/Fe = 0.025, the *n* values for both hematite and goethite increase to an average of 1.70 and 1.47, respectively (Table 1). In general, induction time t_0 values for both goethite and hematite decrease with increasing temperature, indicating that nucleation occurs earlier. Increasing Si concentrations generally result in an increase in the induction time for both goethite and hematite, indicating that Si delays the nucleation of both goethite and hematite (Fig. 7).

Fitting results showed that the crystallization rates for both goethite and hematite exhibit temperature dependence at a given Si/Fe, with rates increasing with increasing temperatures. With increasing Si/Fe, the crystallization rates for both goethite and hematite exhibit a decreasing trend, indicating that the presence of Si also inhibits the crystallization of crystalline phases as well as ferrihydrite transformation. Plots of ln *k* vs. 1/T exhibit linear curves for all systems (Fig. 8), indicating that similar crystallization mechanisms operate within the temperature range studied. Apparent activation energy of crystallization $E_{a(cryst)}$ calculated using the Arrhenius equation for both goethite and hematite exhibit dependence on the concentration of Si (Fig. 9). The $E_{a(cryst)}$ of hematite increases from ~70.3 kJ/mol in the silica-free system to ~117.8 kJ/mol at Si/Fe = 0.025, while that of goethite increases from ~68.7 kJ/mol to ~168.6 kJ/mol in the same range. Since the value of $E_{a(cryst)}$ derived using the JMAK model represents contribution from both nucleation and crystal growth (Lasaga, 1998), the increase in this value with increasing Si indicates an overall retardation effect of Si on the crystallization for both goethite and hematite. In addition, the difference between $E_{a(cryst)}$ for hematite and goethite become larger with increasing Si/Fe, with

goethite increasing more drastically than hematite. This may suggest that Si retards goethite crystallization more effectively than hematite.

TEM observation of crystalline products from 70°C showed that in the absence of Si (Si/Fe = 0, 8 hours), goethite and hematite exhibit lath and disc-shaped morphologies, respectively and grow independently from each other (Fig. 10A). To index their reflections in the diffraction patterns and in other discussions in this paper, the space groups of rhombohedral $R\bar{3}c$ and orthorhombic *Pnma* were used for hematite and goethite, respectively. In the presence of Si (Si/Fe = 0.025) (Fig. 10B), the final reaction products (at 48 hours) are dominated by ellipsoidal crystals. These ellipsoidal crystals are identified to be hematite elongated along the *c* axis (Fig. 10C). Measured average particle sizes of hematite show that these ellipsoidal particles are larger (length ~320 nm, diameter ~120 nm) than the disc-shaped hematite crystals (diameter ~120 nm, thickness ~60 nm), indicating that Si modifies the crystal growth behavior of hematite (Supplementary Information, Table S2). Lath-shaped crystals with sharply terminated facets, which were overgrown epitaxially on the ellipsoidal hematite crystals, are also observed, though they are not present in significant volume fractions compared to hematite. Electron diffraction patterns were used to identify these crystals as goethite (Fig. 10D), indicating that Si likewise influences goethite growth behavior.

A STEM-ADF image and the corresponding STEM-EDS elemental map of crystals formed in the presence of Si (Si/Fe = 0.025, 48 hours) show the distribution of Si in both hematite and goethite crystals (Fig. 10E, F). The ADF signal is roughly proportional to specimen thickness, so that it can be used to examine thickness variation, surface roughness or void distribution. The ellipsoidal hematite crystal has a rough surface with voids of several to a few tens of nanometers, while the goethite crystal has a smooth and flat surface. In addition, the goethite crystal cuts through the hematite crystal, suggesting that goethite grew after the hematite formed. The Si map shows that goethite and hematite both contain Si, with concentrations of up to ~3.0 wt. %. Si appears to be present both on the surface and inside the hematite and goethite crystals, since the Si intensity

distributions are correlated with the crystal thickness, although it is difficult to assess to which site Si is bound.

2.4. Discussion

2.4.1. Characteristics of Precipitates Prior to Heating

XRD results indicate that the Si/Fe of the precipitating solution does not influence the mineralogy of the initially precipitated products. Rapid hydrolysis of the Fe(III) in solution due to the addition of NaOH resulted in the co-precipitation of Si and Fe into poorly ordered ferrihydrite. While the FTIR data show that Si became closely associated with the ferrihydrite via the formation of Si-O-Fe groups, it is not clear if Si is incorporated into the structure of ferrihydrite. However, recent studies have shown that Si occurs mostly on the surface (e.g. Seehra et al., 2004; Dyer et al., 2010, 2012; Cismasu et al., 2014). Detailed IR studies of adsorbed Si on ferrihydrite surfaces show the formation of bidentate surface complexes composed of monomeric silicate species at low Si loadings similar to the concentrations used in this study (Swedlund et al., 2009). Formation of these Si surface complexes results in a net release of protons that decreases the positive charge on the surface (Hiemstra et al., 2007). This is consistent with the changes in the zeta potential observed with increasing Si/Fe (Fig. 3). At higher Si loadings, the surface charge is expected to become more negative, as the Si polymerizes and creates more acidic surface complexes (Swedlund et al., 2010).

2.4.2. Effects of Si on Goethite Crystallization

The apparent activation energy for crystallization of goethite in the pure system (Si/Fe = 0) can be compared with available literature data to determine its crystallization mechanism. There are no published data on its $E_{a(cryst)}$ at pH 10, as most crystallization studies were conducted at higher

pH (>11). However, a study (Yee et al., 2006) extrapolated $E_{a(cryst)}$ for goethite obtained at pH 11.7, 12.0 (Nagano et al., 1994), 13.2 (Davidson et al., 2008) and 13.7 (Shaw et al., 2005) to neutral pH and obtained a value of ~94 kJ/mol at pH 7. Following this extrapolation, the predicted value of $E_{a(cryst)}$ for goethite at pH 10 would fall at approximately ~68 kJ/mol, which is in good agreement with that of Si/Fe = 0 calculated in this study (~68.7 kJ/mol). Under alkaline conditions, goethite is thought to form via the direct precipitation of Fe(III) from solution (Schwertmann and Murad, 1983). The calculated $E_{a(cryst)}$ value for goethite crystallization is consistent with apparent activation energies associated with dissolution and precipitation reactions in minerals, which typically range from ~35 to ~65 kJ/mol or as high as ~150 kJ/mol (Lasaga, 1998). Following this mechanism, goethite crystallization would require the dissolution of the ferrihydrite precursor to supply Fe(III) into solution. This is then followed by the formation of goethite nuclei in solution and the growth of these nuclei by the incorporation of $Fe(OH)_4^-$ from solution. The crystallization of goethite from ferrihydrite is known to follow a first-order reaction mechanism, with the crystallization rate dependent on the amount of remaining ferrihydrite in the system (Schwertmann and Murad, 1983; Shaw et al., 2005). The average *n* value of 1.11, derived from fitting the goethite crystallization data at Si/Fe = 0, is consistent with this interpretation.

The observed increase in $E_{a(cryst)}$ (and decrease in crystallization rate) with increasing Si/Fe (Fig. 9) is consistent with the inhibition of goethite crystallization by Si. This is in line with previous observations of ferrihydrite transformation in the presence of Si (Cornell et al., 1987). Given the mechanism of goethite crystallization, this inhibition may be due to a suppression of either nucleation or crystal growth or both. Previous studies on the sorption of inorganic ligands such as PO_4^{3-} and SO_4^- anions have shown that these ligands form inner-sphere complexes on the surface of ferrihydrite, passivating it against dissolution and limiting the supply of Fe(III) into the solution (Kandori et al., 1992; Biber et al., 1994; Barron et al., 1997; Shaw et al., 2005; Davidson et al., 2008; Zhu et al., 2014). Similarly, the sorption of Si on ferrihydrite surfaces could retard the nucleation and growth of goethite by inhibiting the dissolution of ferrihydrite. The retardation of

goethite nucleation is supported by the observed increase in induction time t_0 with increasing Si (Fig. 7). Although the value of induction time is a complex product of a number of dynamic processes occurring during nucleation, it can be generalized as being proportional to the inverse of the nucleation rate (Mullin, 2001). Increasing Si, therefore, results in a decrease in nucleation rate. Furthermore, dissolution of ferrihydrite (though limited), also likely releases Si back into solution, where it may form complexes with Fe(III) ions, limiting their availability to participate in goethite nucleation and growth (Cismasu et al., 2014).

Apart from delaying the timing of goethite nucleation, Si also influences the nucleation mechanism. The epitaxial growth of goethite on hematite substrates, observed in the TEM images (Fig. 10B), suggests that goethite does not grow homogeneously directly from solution. Previous studies on goethite grown in the presence of PO_4^{3-} (e.g. Barron et al., 1997; Shaw et al., 2005) showed a similar behavior. These studies proposed that the limited supply of Fe(III) into the solution due to the reduced solubility of ferrihydrite, which is in turn due to the sorption of foreign anions, inhibits the homogeneous nucleation of goethite in solution and promotes its nucleation on the surface of hematite crystals.

Another possible effect of Si on goethite crystallization is the poisoning of goethite growth sites by preferential Si sorption on goethite surfaces. Lath-shaped goethite crystals grown in the absence of Si are typically elongated along the *c* axis (Cornell and Giovanoli, 1985), similar to the goethite crystals observed in this study (Fig. 10A). However, the goethite crystals overgrown on hematite appear to be elongated along the *b* axis, while growth along the *c* axis appears to be stunted (Fig. 10D). Due to the higher concentration of hydroxyl groups on the {021} plane relative to other planes on goethite (Barron and Torrent, 1996), foreign anions preferentially adsorb on this plane, which may inhibit crystal growth along directions roughly perpendicular to this plane. Sorption of Si on this plane could result in retarded growth along the *c* axis, while forcing the goethite to grow along the *a* and *b* axes (Glasauer et al., 1999). This may explain the sharply terminated plane perpendicular to the *c* axis and the elongation of the goethite crystal along the *b*

axis observed in the TEM images. Due to lower concentrations of hydroxyl groups on planes perpendicular to the *a* and *b* axes (e.g. {100}, {110}, {010}; Barron and Torrent, 1996), overall crystal growth rate may be retarded compared to the pure system. Thus, apart from retarding goethite nucleation by limiting the supply of soluble Fe(III) species, Si may also retard goethite crystal growth by poisoning its growth surfaces.

2.4.3. Effects of Si on Hematite Crystallization

The calculated $E_{a(cryst)}$ for hematite at pH 10 (~70.3 kJ/mol) is comparable to published values obtained at pH 10.7 (~69 kJ/mol; Shaw et al., 2005) and pH 10 (~65 kJ/mol; Das et al., 2011a). In contrast to goethite, hematite is thought to form via aggregation and dehydroxylation of ferrihydrite (Cornell and Schwertmann, 2003). The aggregation and dehydration process is then followed by a solid-state internal transformation process (Schwertmann and Murad, 1983). However, the calculated $E_{a(cryst)}$ value is significantly lower than apparent activation energies typically associated with solid-state transformation processes, which range from ~85 to ~400 kJ/mol (Lasaga, 1998). Spectroscopic studies (Manceau and Drits, 1993) have noted that the transformation of ferrihydrite to hematite involves the movement of O atoms to different sites, necessitating the partial dissolution of the ferrihydrite framework. Later isotopic studies (Bao and Koch, 1999) similarly suggested that partial dissolution of the ferrihydrite occurs alongside solid-state internal rearrangement processes, although the extent to which this occurs is not clear. If correct, these studies suggest that partial dissolution could lower the activation barrier to hematite crystallization than if only solid-state rearrangement is involved. If partial dissolution is involved, then some Fe(III) is released into solution, which could contribute to the growth of hematite crystals by ripening. Furthermore, ferrihydrite to hematite transformation is thought to follow a first-order kinetic reaction similar to goethite (Fischer and Schwertmann, 1975). The average *n* value derived from the fitting is consistent with this interpretation.

The observed increase in hematite percentage relative to goethite in this study (Fig. 5) is consistent with a previous study showing that the presence of Si 'promotes' the formation of hematite at the expense of goethite (Cornell et al., 1987). In the previous study, this 'promotion' was explained in terms of the combined effect of Si and salts in the solution. However, in the present study, since Si was introduced as TEOS, variations in the concentration of Si did not introduce changes in electrolyte concentrations. Thus, the salt concentrations in all of the samples are approximately constant. Instead, apparent promotion of hematite relative to goethite may be understood in terms of the competitive processes that control crystallization. The critical process in hematite crystallization involves the aggregation of ferrihydrite. The aggregation rate is dependent on the particle concentration based on the equation:

$$\frac{dN}{dt} = -k_a N_i^2 \qquad (6)$$

where N_i is the initial concentration of particles and k_a is the rate constant for particle transport (Stumm and Morgan, 1996). This indicates that the number of particles in a system decreases faster (i.e. aggregation is favored) with higher concentrations of initial particles. If ferrihydrite dissolution is suppressed by the sorption of Si, the concentration of ferrihydrite particles that become available for aggregation increases, leading to the formation of hematite. Thus, there is an indirect promotion effect of Si on hematite crystallization.

However, the increase in the $E_{a(cryst)}$ for hematite with increasing Si (Fig. 9) indicates that hematite is likewise inhibited. This may indicate that hematite nucleation and crystal growth may be more directly affected by the presence of Si. Aggregation of ferrihydrite, for example, may be inhibited by ligands that introduce electrostatic repulsion. Aggregation of ferrihydrite is favored at near neutral to slightly alkaline pH conditions, close to the pH_{pzc} of ferrihydrite (Cornell and Schwertmann, 2003). At pH 10, the charge on the ferrihydrite is slightly negative, due to the presence of OH^- surface groups. However, as seen from the zeta potential data of the initial precipitates, the surface charge of ferrihydrite becomes more negative with increasing Si/Fe (Fig. 3). The increasing negative charge on the surface of ferrihydrite may inhibit the aggregation of

ferrihydrite, resulting in the retardation of hematite nucleation. This may explain the increase in induction time t_0 with increasing Si (Fig. 7).

The growth of hematite crystals may also be retarded by the presence of Si on their surfaces. Previous studies on the sorption inorganic anions such as sulfate (Sugimoto and Wang, 1998) and phosphate (Jia et al., 2005; Jia et al., 2008) and organic compounds such as amino acids (Kandori et al., 2006) and ascorbic acids (Tan et al., 2014) on hematite particles have shown that these compounds promote the anisotropic growth of hematite. Due to higher concentrations of hydroxyl groups on planes parallel to the *c* axis of hematite, the growth in a pure system proceeds more readily in the in-plane direction of the {001} plane. Preferential sorption of sulfate anions, amino acids and ascorbic acids on these planes restricts growth in the in-plane direction and forces growth to proceed along the *c* axis. This shift in growth direction may be manifested as an increase in the length of the *c* axis (Tan et al., 2014). In this study, unit cell parameters for hematite derived from Rietveld refinement show the *c* axis increases with increasing Si/Fe (Fig. 11), which could be associated with morphological change. This is confirmed by the ellipsoidal morphology and the elongation along the *c* axis assumed by hematite crystals in the presence of Si (Fig. 10B,C), indicating Si likewise promotes the anisotropic growth of hematite crystals. These observations are consistent with the mechanism of hematite crystallization involving the partial dissolution of ferrihydrite and the release Fe(III) and Si into solution. Due to the lower concentrations of hydroxyl groups on planes perpendicular to the *c* axis, growth may proceed slower along this direction. However, it is not clear to what extent this process contributes to the overall inhibition of hematite crystallization.

2.4.4. Overall Role of Si in Fe(III) Mineral Crystallization

The effects of Si on the crystallization of Fe(III) phases are summarized in Fig. 12. While it is clear both goethite and hematite are inhibited by the presence of Si, the changes in the apparent

activation energy data with increasing Si suggest that goethite is more inhibited relative to hematite (Fig. 9). As discussed in the preceding sections, Si influences different stages of the crystallization process for both phases. At a given Si/Fe, goethite nucleation may be retarded by the limited supply of Fe(III) due to retarded ferrihydrite dissolution, while hematite nucleation is retarded by inhibited ferrihydrite aggregation. The delay in the nucleation of both phases is manifested as an increase in induction time t_0 (Fig. 7). However, the delay in goethite, most evidently seen in Si/Fe = 0.025, is longer relative to hematite, indicating that the inhibition of goethite nucleation is more effective compared to hematite. This may be understood in terms of differences in activation energies associated with dissolution and particle aggregation. An estimate of the apparent activation energy for the reductive dissolution of ferrihydrite is placed at approximately ~41 kJ/mol (Erbs et al., 2010). This indicates that the dissolution process itself, which involves the removal of metal centers on the surface, is characterized by a relatively high activation barrier. In contrast, the activation energy related to overcoming electrostatic forces against ferrihydrite aggregation is estimated at ~24 kJ/mol (Shaw et al., 2005). These published values show that the activation barrier to dissolve ferrihydrite is higher compared to the barrier required to aggregate ferrihydrite particles. Thus, with increasing Si concentration, the ferrihydrite particles have a greater tendency to aggregate than to dissolve. Assuming that the relative difference between these values is true at any given Si/Fe, this may explain the greater degree of inhibition of goethite crystallization relative to hematite. However, at higher degrees of Si loading, the increasingly negative surface charge of ferrihydrite particles due to Si polymerization may eventually inhibit transformation even to hematite.

Although this study investigated very low degrees of Si loading, it may be reasonable to assume that the mechanism discussed above may become more pronounced at higher concentrations of Si. Average concentrations of Si in natural waters are in the range of a few tens to a few hundred mg/L (Iler, 1979; Treguer et al., 1995; Gallinari et al., 2002; Cornelis et al., 2011). At higher Si loading, surface coverage increases and Si polymerizes on the surfaces of oxides, forming linked silanol groups (Swedlund et al., 2009). With increasing degrees of polymerization, the acidity of

these silanol groups also increases, imparting increasingly negative surface charges to oxide surfaces (Swedlund et al., 2010). This translates to a greater degree of surface passivation and hence greater degree of inhibition. This is supported by preliminary experiments conducted for this study at Si/Fe $\geq$ 0.01, where samples exhibited the characteristic dark brown color of ferrihydrite even after more than 1 week of heating at 70°C, indicating the absence of crystallization.

2.5. Conclusions

The crystallization of goethite and hematite from ferrihydrite in the presence of Si was investigated at alkaline conditions using XRD and TEM. Mineral abundances evaluated from Rietveld refinement of XRD data show that the proportion of goethite in the final assemblage decreases relative to hematite with increasing Si. TEM observation of goethite and hematite crystals formed in the presence of Si show significant morphological differences compared to those formed in the absence of Si. Rate constants for crystallization derived from fitting of time-dependent changes in mineral abundances with the Avrami equation show a decreasing trend with increasing Si for both goethite and hematite. Apparent activation energies for crystallization for both minerals increase with increasing Si, with that of goethite increasing more drastically compared to hematite, indicating the inhibitive effect of Si on the crystallization of both minerals. The overall inhibition of crystallization may be explained in terms of the effects of Si on the surface properties of the ferrihydrite precursor. The rate constants and apparent activation energies reported in this study may be useful in estimating the crystallization behavior and timescales of Fe minerals in both natural and engineered environments. These informations may eventually be helpful in predicting the fate of hazardous elements in such environments.

2.6. List of References

Avrami, M. (1939) Kinetics of phase change I - General theory. Journal of Chemical Physics, 7(12), 1103-1112.

Avrami, M. (1940) Kinetics of phase change II - Transformation - time relations for random distribution of nuclei. Journal of Chemical Physics, 8(2), 212.

Avrami, M. (1941) Granulation, phase change, and microstructure - Kinetics of phase change. III. Journal of Chemical Physics, 9(2), 177-184.

Bao, H.M., and Koch, P.L. (1999) Oxygen isotope fractionation in ferric oxide-water systems: Low temperature synthesis. Geochimica Et Cosmochimica Acta, 63(5), 599-613.

Bargar, J.R., Reitmeyer, R., and Davis, J.A. (1999) Spectroscopic confirmation of uranium(VI)-carbonato adsorption complexes on hematite. Environmental Science & Technology, 33(14), 2481-2484.

Barron, V., Galvez, N., Hochella, M.F., Jr., Torrent, J. (1997) Epitaxial overgrowth of goethite on hematite synthesized in phosphate media: A scanning force and transmission electron microscopy study. American Mineralogist, 82, 1091-1100.

Barron, V., and Torrent, J. (1996) Surface hydroxyl configuration of various crystal faces of hematite and goethite. Journal of Colloid and Interface Science, 177(2), 407-410.

Bazilevskaya, E., Archibald, D.D., and Martinez, C.E. (2012) Rate constants and mechanisms for the crystallization of Al nano-goethite under environmentally relevant conditions. Geochimica Et Cosmochimica Acta, 88, 167-182.

Biber, M.V., Afonso, M.D., and Stumm, W. (1994) The Coordination chemistry of weathering .4. Inhibition of the dissolution of oxide minerals. Geochimica Et Cosmochimica Acta, 58(9), 1999-2010.

Brinza, L., Vu, H.P., Shaw, S., Mosselmans, J.F.W., and Benning, L.G. (2015) Effect of Mo and V on the hydrothermal crystallization of hematite from ferrihydrite: An *in situ* energy

dispersive x-ray diffraction and x-ray absorption spectroscopy study. Crystal Growth & Design, doi: 10.1021/acs.cgd.5b00173, in press.

Buekers, J., Amery, F., Maes, A., and Smolders, E. (2008) Long-term reactions of Ni, Zn and Cd with iron oxyhydroxides depend on crystallinity and structure and on metal concentrations. European Journal of Soil Science, 59(4), 706-715.

Cismasu, A.C., Michel, F.M., Tcaciuc, A.P., and Brown, G.E. (2014) Properties of impurity-bearing ferrihydrite III. Effects of Si on the structure of 2-line ferrihydrite. Geochimica Et Cosmochimica Acta, 133, 168-185.

Cornelis, J.T., Delvaux, B., Georg, R.B., Lucas, Y., Ranger, J., and Opfergelt, S. (2011) Tracing the origin of dissolved silicon transferred from various soil-plant systems towards rivers: a review. Biogeosciences, 8(1), 89-112.

Cornell, R.M., Giovanoli, R., and Schindler, P.W. (1987) Effect of silicate species on the transformation of ferrihydrite into goethite and hematite in alkaline media. Clays and Clay Minerals, 35(1), 21-28.

Cornell, R.M., Schwertmann, U. (2003) The Iron Oxides: Structure, Properties, Reactions, Occurrences and Uses, 2nd ed., 703 p. Wiley-VCH, Weinheim.

Cudennec, Y., and Lecerf, A. (2006) The transformation of ferrihydrite into goethite or hematite, revisited. Journal of Solid State Chemistry, 179(3), 716-722.

Das, S., Hendry, M.J., and Essilfie-Dughan, J. (2011a) Transformation of two-line ferrihydrite to goethite and hematite as a function of pH and temperature. Environmental Science & Technology, 45(1), 268-275.

Das, S., Hendry, M.J., and Essilfie-Dughan, J. (2011b) Effects of adsorbed arsenate on the rate of transformation of 2-Line ferrihydrite at pH 10. Environmental Science & Technology, 45(13), 5557-5563.

Das, S., Hendry, M.J., and Essilfie-Dughan, J. (2013) Adsorption of selenate onto ferrihydrite, goethite, and lepidocrocite under neutral pH conditions. Applied Geochemistry, 28, 185-193.

Davidson, L.E., Shaw, S., and Benning, L.G. (2008) The kinetics and mechanisms of schwertmannite transformation to goethite and hematite under alkaline conditions. American Mineralogist, 93(8-9), 1326-1337.

De La Torre, A.G., Bruque, S., and Aranda, M.A.G. (2001) Rietveld quantitative amorphous content analysis. Journal of Applied Crystallography, 34, 196-202.

Doelsch, E., Stone, W.E.E., Petit, S., Masion, A., Rose, J., Bottero, J.Y., and Nahon, D. (2001) Speciation and crystal chemistry of Fe(III) chloride hydrolyzed in the presence of SiO4 ligands. 2. Characterization of Si-Fe aggregates by FTIR and Si-29 solid-state NMR. Langmuir, 17(5), 1399-1405.

Doelsch, E., Masion, A., Rose, J., Stone, W.E.E., Bottero, J.Y., Bertsch, P.M. (2003) Chemistry and structure of colloids obtained by hydrolysis of Fe(III) in the presence of SiO_4 ligands. Colloids and Surfaces A, 217, 121-128.

Dyer, L., Fawell, P.D., Newman, O.M.G., and Richmond, W.R. (2010) Synthesis and characterisation of ferrihydrite/silica co-precipitates. Journal of Colloid and Interface Science, 348(1), 65-70.

Dyer, L., Chapman, K.W., English, P., Saunders, M., Richmond, W.R. (2012) Insights into the crystal and aggregate structure of Fe^{3+} oxide/silica co-precipitates. American Mineralogist, 97, 63-69.

Erbs, J.J., Berquo, T.S., Reinsch, B.C., Lowry, G.V., Banerjee, S.K., and Penn, R.L. (2010) Reductive dissolution of arsenic-bearing ferrihydrite. Geochimica Et Cosmochimica Acta, 74(12), 3382-3395.

Fischer, W.R., and Schwertmann, U. (1975) Formation of hematite from amorphous iron (III) hydroxide. Clays and Clay Minerals, 23(1), 33-37.

Fukushi, K., Sato, T., and Yanase, N. (2003) Solid-solution reactions in As(V) sorption by schwertmannite. Environmental Science & Technology, 37(16), 3581-3586.

Gallinari, M., Ragueneau, O., Corrin, L., DeMaster, D.J., and Treguer, P. (2002) The importance of water column processes on the dissolution properties of biogenic silica in deep-sea sediments I. Solubility. Geochimica Et Cosmochimica Acta, 66(15), 2701-2717.

Glasauer, S., Friedl, J., and Schwertmann, U. (1999) Properties of goethites prepared under acidic and basic conditions in the presence of silicate. Journal of Colloid and Interface Science, 216(1), 106-115.

Hazan, E., Sadia, Y., and Gelbstein, Y. (2013) Characterization of AISI 4340 corrosion products using Raman spectroscopy. Corrosion Science, 74, 414-418.

Hiemstra, T., Barnett, M.O., and van Riemsdijk, W.H. (2007) Interaction of silicic acid with goethite. Journal of Colloid and Interface Science, 310(1), 8-17.

Houston, J.R., Maxwell, R.S., and Carroll, S.A. (2009) Transformation of meta-stable calcium silicate hydrates to tobermorite: reaction kinetics and molecular structure from XRD and NMR spectroscopy. Geochemical Transactions, 10.

IAEA (2012) The Safety Case and Safety Assessment for the Disposal of Radioactive waste. IAEA Safety Standards Series. International Atomic Energy Agency Technical Report, Vienna.

Iler, R.K. (1979) The Chemistry of Silica: Solubility, Polymerization, Colloid and Surface Properties and Biochemistry of Silica, 896 p. Wiley-Interscience, New York.

JAEA (2007) Second Progress Report on Research and Development for TRU Waste Disposal in Japan - Repository Design, Safety Assessment and Means of Implementation in the Generic Phase, Japan Atomic Energy Agency Technical Report, Tokyo.

Jia, C.J., Sun, L.D., Yan, Z.G., You, L.P., Luo, F., Han, X.D., Pang, Y.C., Zhang, Z., and Yan, C.H. (2005) Iron oxide nanotubes - Single-crystalline iron oxide nanotubes. Angewandte Chemie-International Edition, 44(28), 4328-4333.

Jia, C.J., Sun, L.D., Luo, F., Han, X.D., Heyderman, L.J., Yan, Z.G., Yan, C.H., Zheng, K., Zhang, Z., Takano, M., Hayashi, N., Eltschka, M., Klaui, M., Rudiger, U., Kasama, T., Cervera-Gontard, L., Dunin-Borkowski, R.E., Tzvetkov, G., and Raabe, J. (2008) Large-scale

synthesis of single-crystalline iron oxide magnetic nanorings. Journal of the American Chemical Society, 130(50), 16968-16977.

JNC (2000) H12: Project to establish the scientific and technical basis for HLW disposal in Japan (H12 Report), Japan Nuclear Cycle Development Institute Technical Report, Tokyo.

Kandori, K., Uchida, S., Kataoka, S., and Ishikawa, T. (1992) Effects of silicate and phosphate ions on the formation of ferric-oxide hydroxide particles. Journal of Materials Science, 27(3), 719-728.

Kandori, K., Sakai, M., Inoue, S., and Ishikawa, T. (2006) Effects of amino acids on the formation of hematite particles in a forced hydrolysis reaction. Journal of Colloid and Interface Science, 293(1), 108-115.

Karim, Z. (1984) Characteristics of ferrihydrites formed by oxidation of $FeCl_2$ solutions containing different amounts of silica. Clays and Clay Minerals, 32(3), 181-184.

Kasama, T., Thuvander, M., Siusys, A., Gontard, L.C., Kovacs, A., Yazdi, S., Duchamp, M., Dunin-Borkowski, R.E., and Sadowski, J. (2015) Direct observation of doping incorporation pathways in self-catalytic GaMnAs nanowires. Journal of Applied Physics, 118, 054302.

Kumazawa, K. (2002) Nitrogen fertilization and nitrate pollution in groundwater in Japan: Present status and measures for sustainable agriculture. Nutrient Cycling in Agrosystems, 63, 129-137.

Kwon, S.K., Shinoda, K., Suzuki, S., and Waseda, Y. (2007) Influence of silicon on local structure and morphology of gamma-FeOOH and alpha-FeOOH particles. Corrosion Science, 49(3), 1513-1526.

Lasaga, A. (1998) Kinetic Theory in the Earth Sciences, 824 p. Princeton University Library, Princeton.

Li, X., Nail, S.L. (2005). Kinetics of glycine crystallization during freezing of sucrose/glycine excipient systems. Journal of Pharmaceutical Sciences, 94(3), 625-631.

Manceau, A., and Drits, V.A. (1993) Local-structure of ferrihydrite and feroxyhite by EXAFS Spectroscopy. Clay Minerals, 28(2), 165-184.

Marshall, T.A., Morris, K., Law, G.T.W., Livens, F.R., Mosselmans, J.F.W., Bots, P., and Shaw, S. (2014) Incorporation of uranium into hematite during crystallization from ferrihydrite. Environmental Science & Technology, 48(7), 3724-3731.

Mullin, J.W. (2001) Crystallization, 4th ed., 600 p. Butterworth-Heinemann, Oxford.

Nagano, T., Nakashima, S., Nakayama, S., and Senoo, M. (1994) The use of color to quantify the effects of pH and temperature on the crystallization kinetics of goethite under highly alkaline conditions. Clays and Clay Minerals, 42(2), 226-234.

NUMO (2004a) Development of repository concepts for volunteer siting environments. Nuclear Waste Management Organization of Japan Technical Report 04-03, Tokyo.

NUMO (2004b) Proceedings of the International Workshop on Bentonite-Cement Interaction in Repository Environments, Nuclear Waste Management Organization of Japan Technical Report, 04-05, Tokyo.

Peak, D., and Sparks, D.L. (2002) Mechanisms of selenate adsorption on iron oxides and hydroxides. Environmental Science & Technology, 36(7), 1460-1466.

Refait, P., Benali, O., Abdelmoula, M., and Genin, J.M.R. (2003) Formation of 'ferric green rust' and/or ferrihydrite by fast oxidation of iron(II-III) hydroxychloride green rust. Corrosion Science, 45(11), 2435-2449.

Rovira, M., Gimenez, J., Martinez, M., Martinez-Llado, X., de Pablo, J., Marti, V., and Duro, L. (2008) Sorption of selenium(IV) and selenium(VI) onto natural iron oxides: Goethite and hematite. Journal of Hazardous Materials, 150(2), 279-284.

Russell, J.D. (1979) Infrared spectroscopy of ferrihydrite - evidence for the presence of structural hydroxyl-groups. Clay Minerals, 14(2), 109-114.

Savage, D., Noy, D., and Mihara, M. (2002) Modelling the interaction of bentonite with hyperalkaline fluids. Applied Geochemistry, 17(3), 207-223.

Schwertmann, U., and Murad, E. (1983) Effect of pH on the formation of goethite and hematite from ferrihydrite. Clays and Clay Minerals, 31(4), 277-284.

Schwertmann, U., and Thalmann, H. (1976) Influence of [Fe(II)], [Si], and pH on formation of lepidocrocite and ferrihydrite during oxidation of aqueous $FeCl_2$ solutions. Clay Minerals, 11(3), 189-200.

Seehra, M.S., Roy, P., Raman, A., and Manivannan, A. (2004) Structural investigations of synthetic ferrihydrite nanoparticles doped with Si. Solid State Communications, 130(9), 597-601.

Shaw, S., Pepper, S.E., Bryan, N.D., and Livens, F.R. (2005) The kinetics and mechanisms of goethite and hematite crystallization under alkaline conditions, and in the presence of phosphate. American Mineralogist, 90(11-12), 1852-1860.

Stumm, W., Morgan, J.J. (1996) Aquatic Chemistry: Chemical Equilibria and Rates in Natural Waters, 3rd ed., 1040 p. Wiley-Interscience, New York.

Sugimoto, T., Wang, Y.S., Itoh, H., and Muramatsu, A. (1998) Systematic control of size, shape and internal structure of monodisperse alpha-Fe2O3 particles. Colloids and Surfaces a-Physicochemical and Engineering Aspects, 134(3), 265-279.

Swedlund, P.J., Miskelly, G.M., and McQuillan, A.J. (2009) An attenuated total reflectance IR study of silicic acid adsorbed onto a ferric oxyhydroxide surface. Geochimica Et Cosmochimica Acta, 73(14), 4199-4214.

Swedlund, P.J., Miskelly, G.M., and McQuillan, A.J. (2010) Silicic acid adsorption and oligomerization at the ferrihydrite-water interface: Interpretation of ATR-IR spectra based on a model surface structure. Langmuir, 26(5), 3394-3401.

Tan, W.F., Yu, Y.T., Wang, M.X., Liu, F., and Koopal, L.K. (2014) Shape evolution synthesis of monodisperse spherical, ellipsoidal, and elongated hematite (alpha-Fe_2O_3) nanoparticles using ascorbic acid. Crystal Growth & Design, 14(1), 157-164.

Taylor, J.C., and Clapp, R.A. (1992) New features and advanced applications of Siroquant: A personal computer XRD full profile quantitative analysis software package. Advances in X-ray Analysis, 35, 49-55.

Treguer, P., Nelson, D.M., Vanbennekom, A.J., Demaster, D.J., Leynaert, A., and Queguiner, B. (1995) The silica balance in the world ocean - a reestimate. Science, 268(5209), 375-379.

Vaughan, G., Brydson, R., and Brown, A. (2012) Characterisation of synthetic two-line ferrihydrite by electron energy loss spectroscopy. Journal of Physics: Conference Series 371, Electron Microscopy and Analysis Group Conference 2011, Birmingham.

Vempati, R.K., and Loeppert, R.H. (1989) Influence of structural and adsorbed Si on the transformation of synthetic ferrihydrite. Clays and Clay Minerals, 37(3), 273-279.

Westphal, T., Füllman, T., Pöllman, H. (2009) Rietveld quantification of amorphous portions with an internal standard - Mathematical consequences of the experimental approach. Powder Diffraction, 24(3), 239-243.

Yee, N., Shaw, S., Benning, L.G., and Nguyen, T.H. (2006) The rate of ferrihydrite transformation to goethite via the Fe(II) pathway. American Mineralogist, 91(1), 92-96.

Zhu, M., Northrup, P., Shi, C., Billinge, S.J.L., Sparks, D.L., Waychunas, G.A. (2014) Structure of sulfate adsorption complexes on ferrihydrite. Environmental Science and Technology, 1 (1), 97-101.

Table 1: Summary of results of the kinetic analysis of goethite and hematite crystallization at different temperatures and Si/Fe ratios.

T (°C)	Crystallization Rates *k* (1/hr)[a]									
	Si/Fe=0		**Si/Fe=0.001**		**Si/Fe=0.005**		**Si/Fe=0.01**		**Si/Fe=0.025**	
	Gt	Hm	Gt	Hm	Gt	Hm	Gt	Hm	Gt	Hm
50	0.204	0.253	0.0874	0.106	0.0404	0.0468	0.0243	0.0195	0.0026	0.0024
60	0.395	0.486	0.244	0.247	0.159	0.167	0.090	0.0689	0.0231	0.0135
70	0.857	1.081	0.529	0.619	0.403	0.357	0.335	0.166	0.0984	0.0236
80	1.758	2.301	1.548	1.361	1.091	0.908		0.504		0.127
n[b]	1.11	1.07	1.57	1.59	1.61	1.73	1.70	1.74	1.47	1.70
$E_{a(cryst)}$ (kJ/mol)[a]	68.7	70.3	89.1	81.4	102.8	91.8	120.9	100.9	168.6	117.8

Note(s): Gt: Goethite, Hm: Hematite

[a] Uncertainties from triplicate samples range from 3 to 5% of values reported in this table.

[b] *n* is reported as the average of *n* values from fitting at different temperatures.

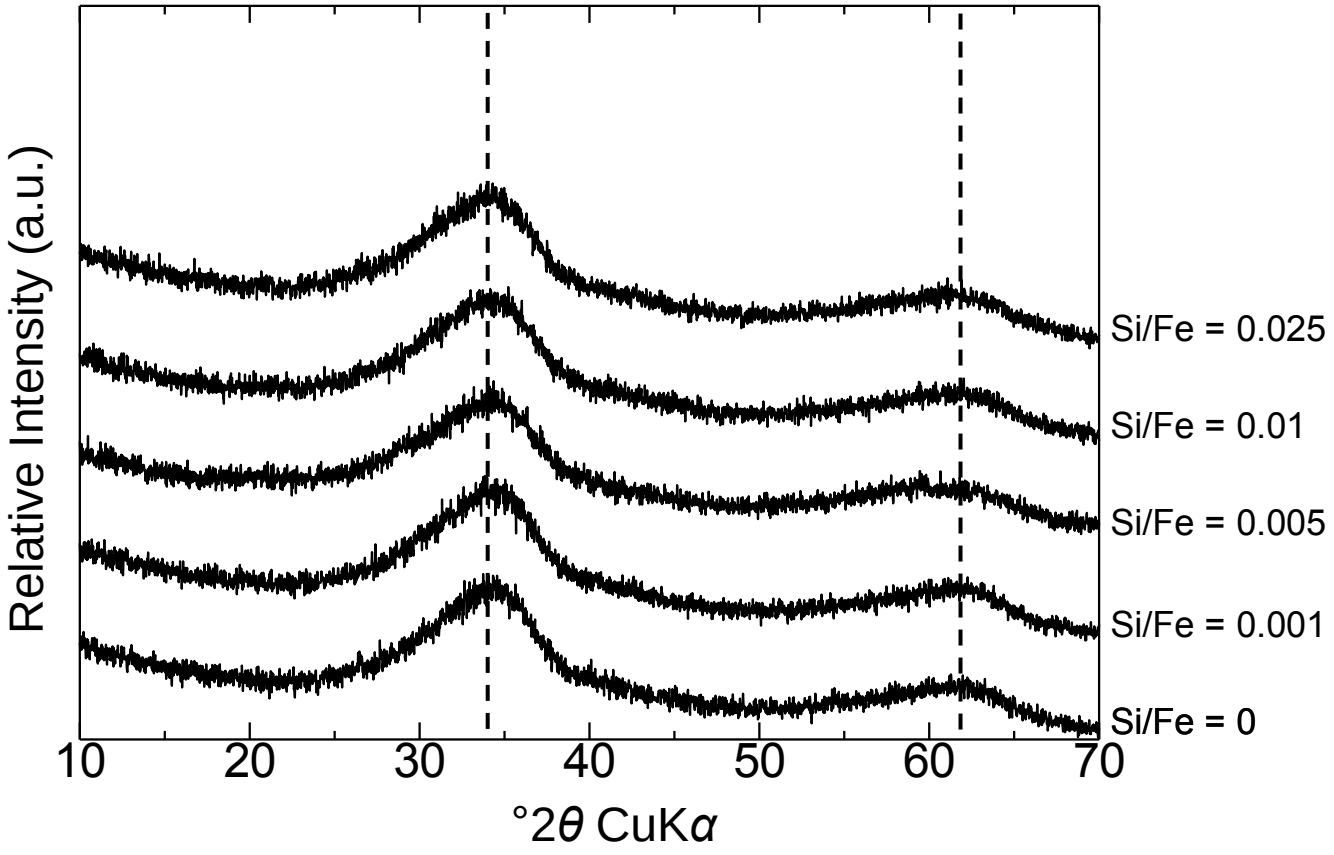

Fig. 1. XRD profiles of initial precipitates extracted prior to heating. At all Si/Fe, the precipitates are characterized by two broad humps indicative of poorly crystalline 2-line ferrihydrite.

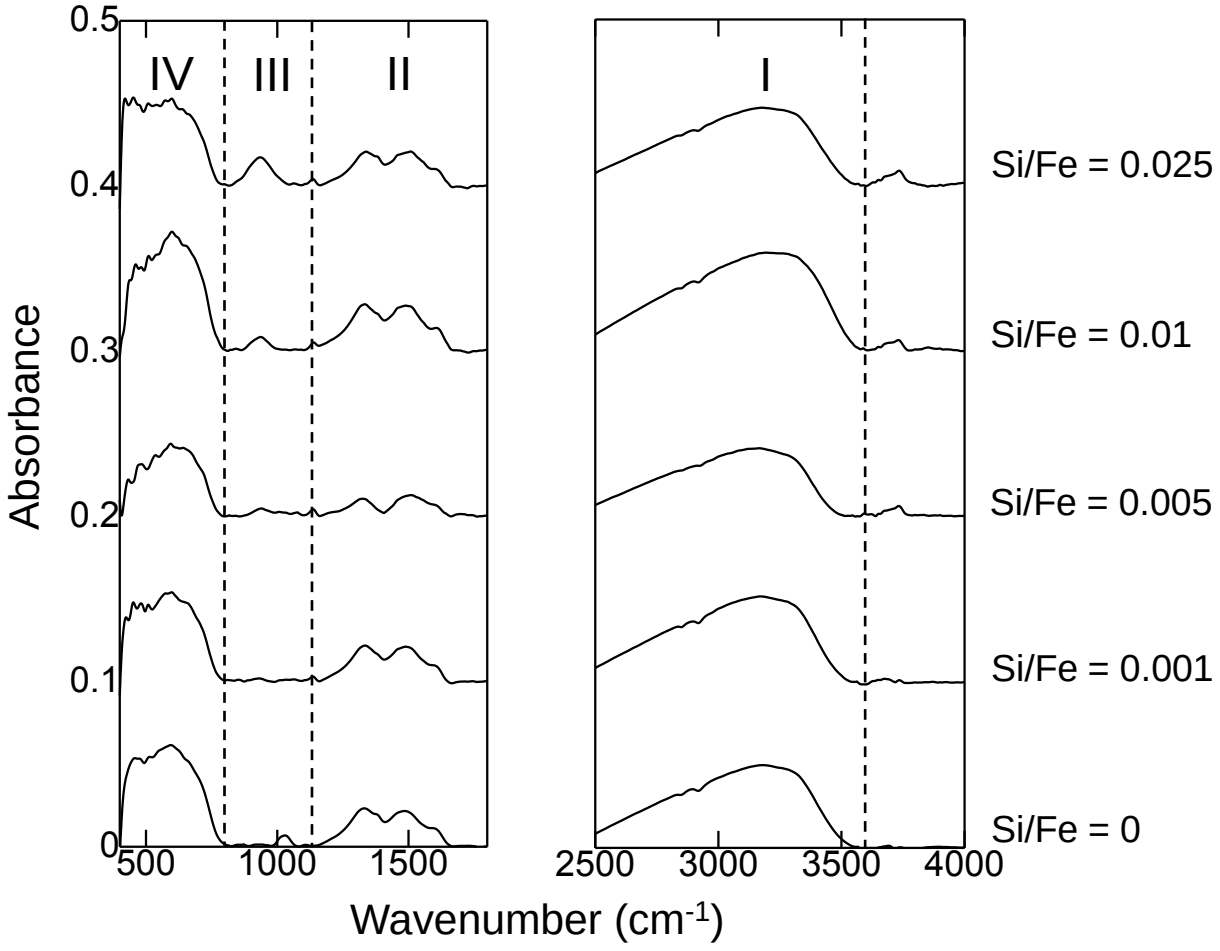

Fig. 2. FTIR spectra of initial precipitates extracted prior to heating. In region III, an absorption band corresponding to the asymmetric stretching vibrations of Fe-O-Si appears and increases in intensity with increasing Si/Fe. No significant shifts can be observed in this band.

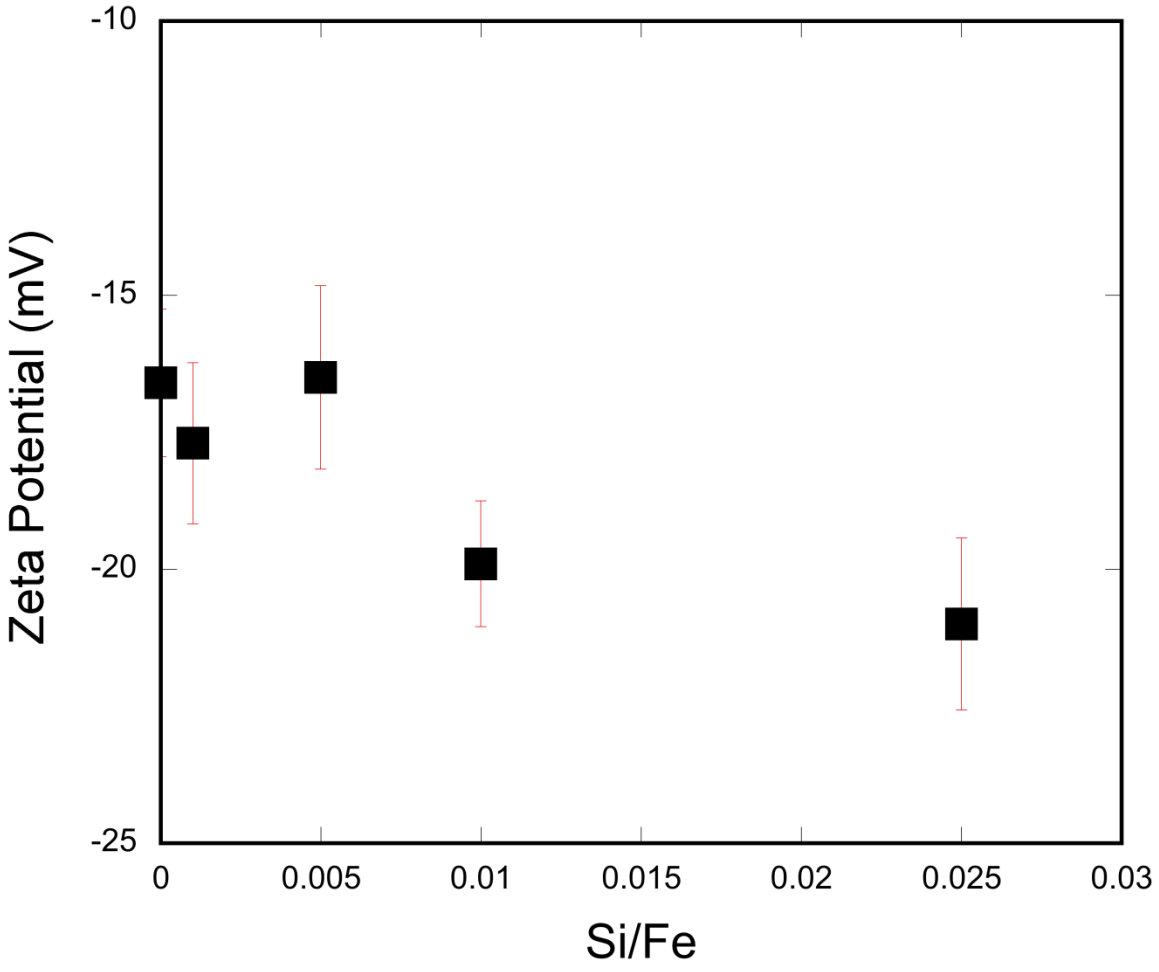

Fig. 3. Zeta potential of initial precipitates measured at pH 10. The surface charge of the precipitates at alkaline conditions becomes more negative with increasing Si.

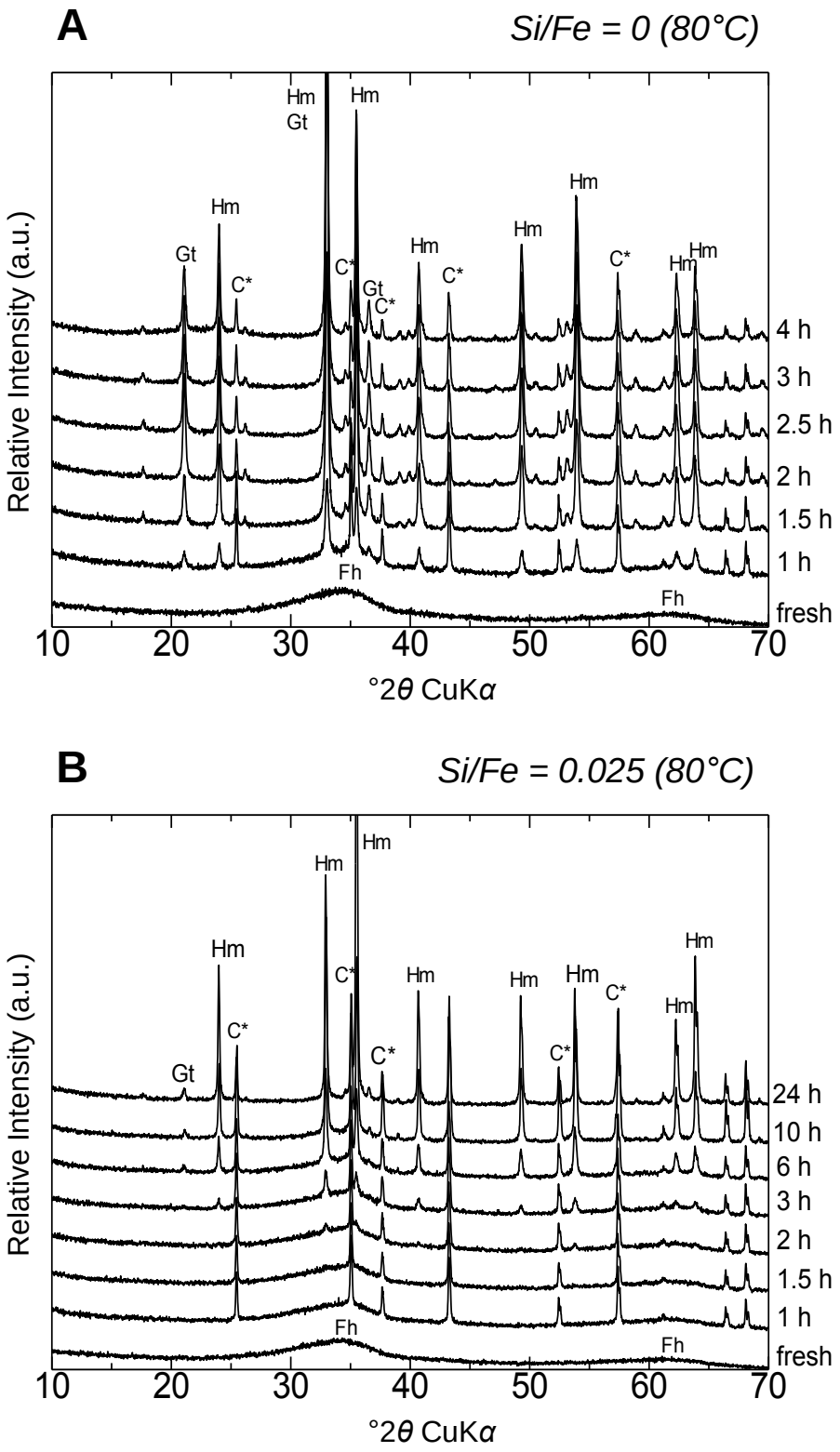

Fig. 4. XRD profiles for samples with different Si/Fe ratios (A. Si/Fe=0, pure system; B. Si/Fe=0.025) heated at 80°C showing the crystallization over time of goethite and hematite from ferrihydrite. (*Fh*: Ferrihydrite; *Gt*: Goethite; *Hm*: Hematite; *C**: Corundum internal standard).

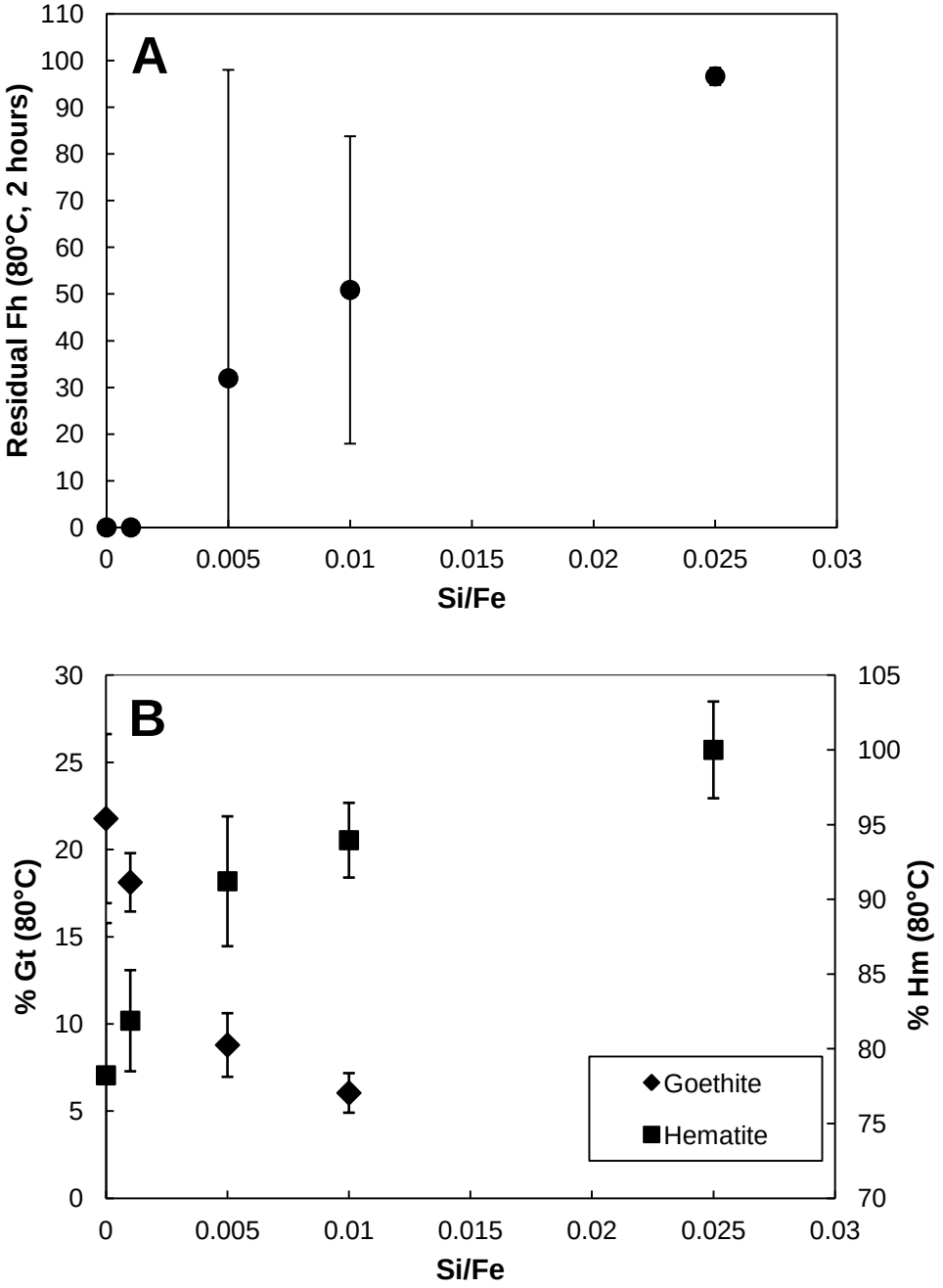

Fig. 5. (A) Residual ferrihydrite after 2 hours of heating at 80°C. Error bars correspond to the uncertainties propagated from the amorphous calculation formula and Rietveld refinement. (B) Percentage of goethite and hematite in the final products at 80°C. Error bars correspond to uncertainties derived directly from Rietveld refinement.

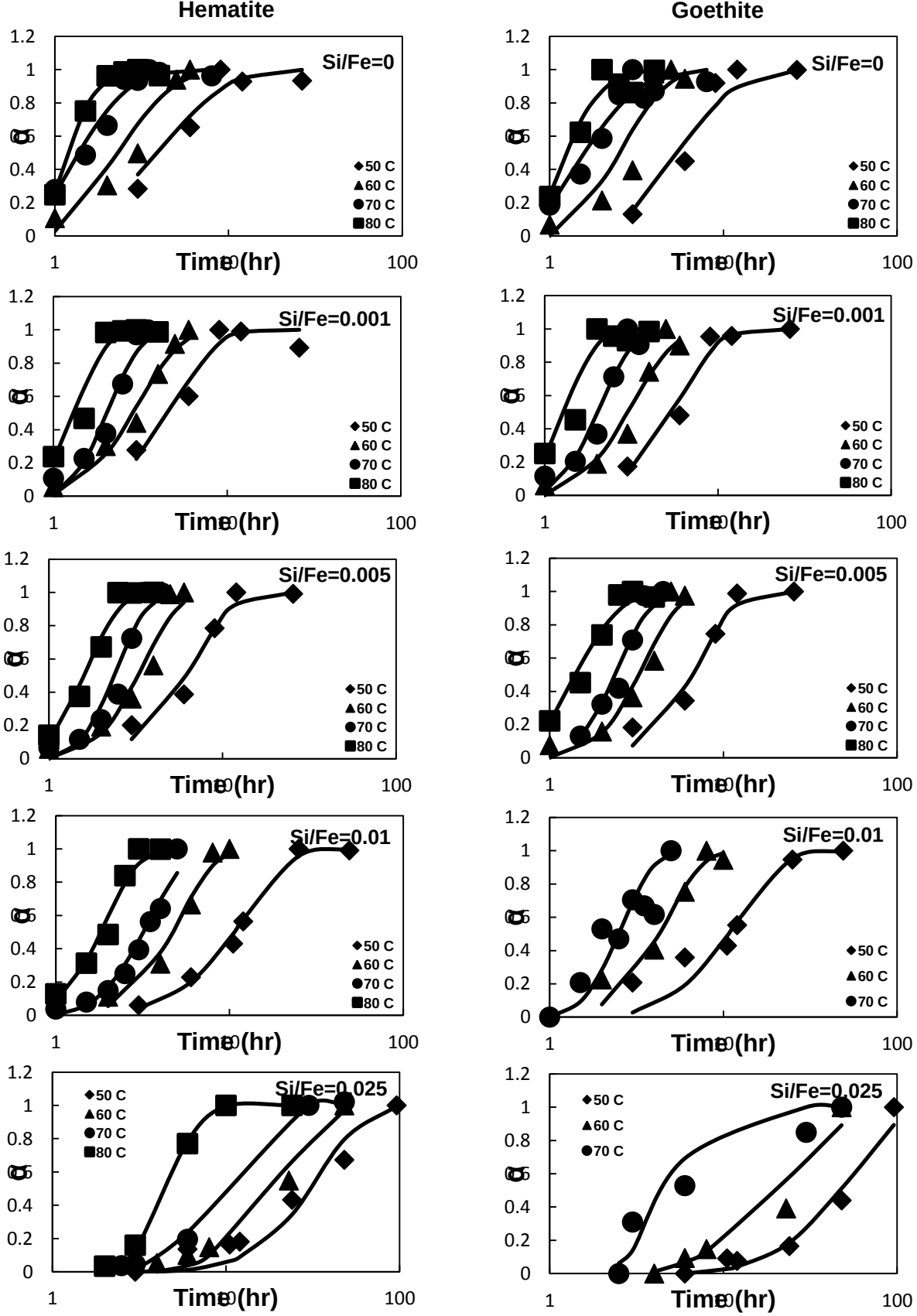

Fig. 6. Plots of reaction progress α as a function of time for goethite and hematite at different Si/Fe ratios. The solid lines represent the fits of the JMAK kinetic model.

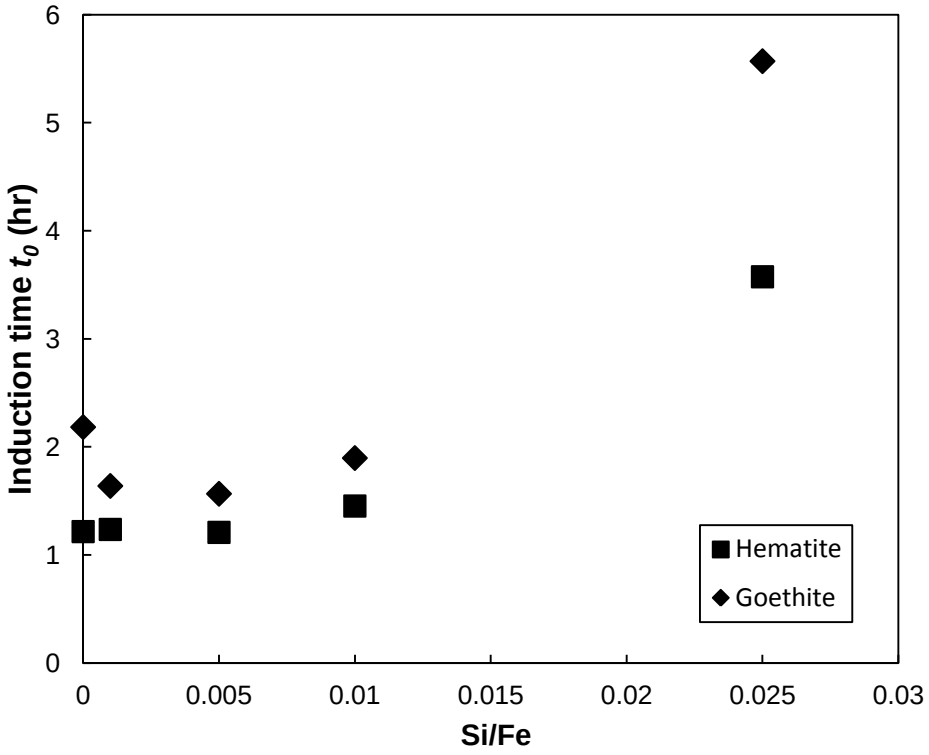

Fig. 7. Induction times for hematite and goethite at 50°C as a function of Si/Fe.

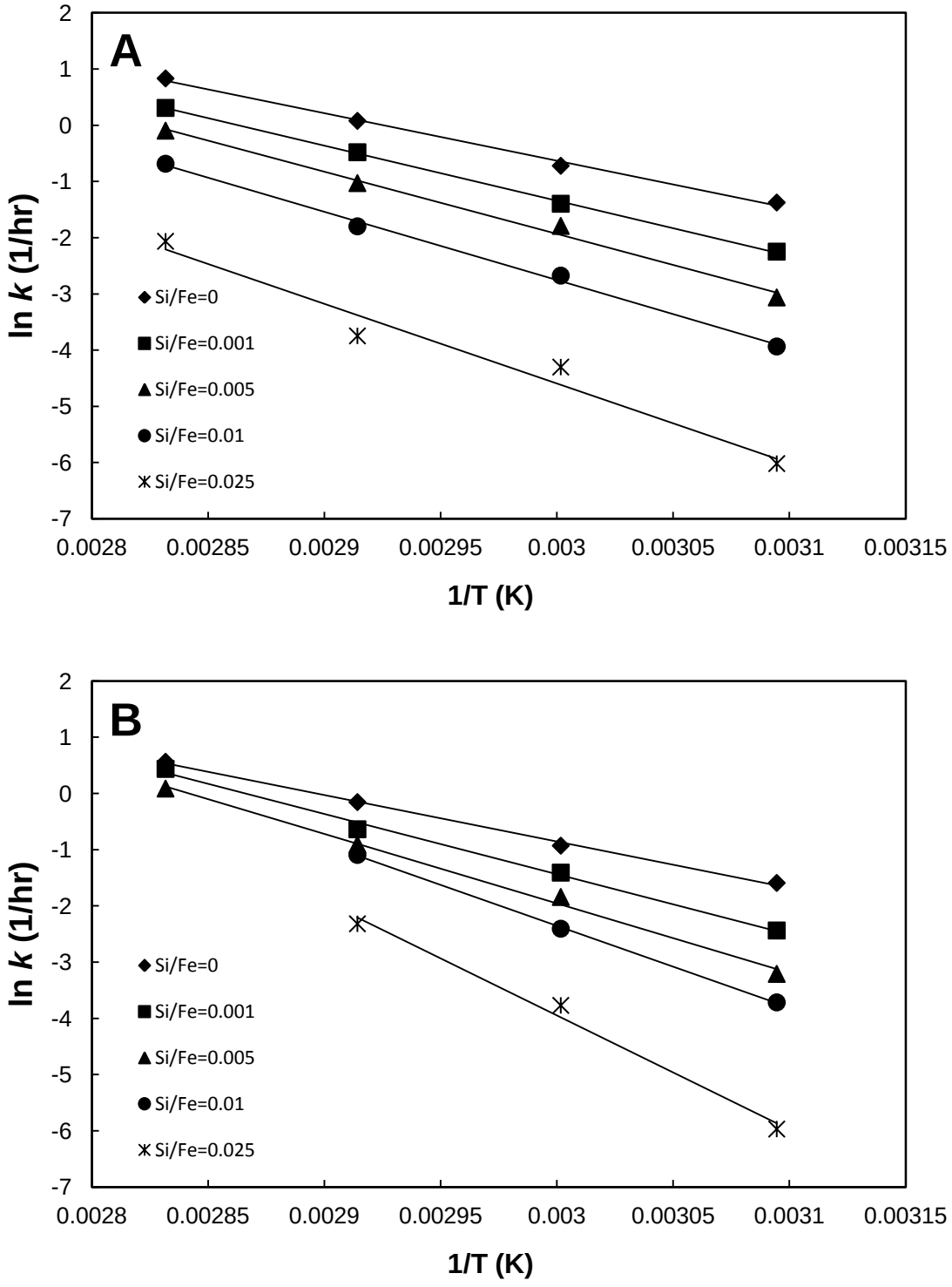

Fig. 8. Arrhenius plots of (A) hematite and (B) goethite crystallization.

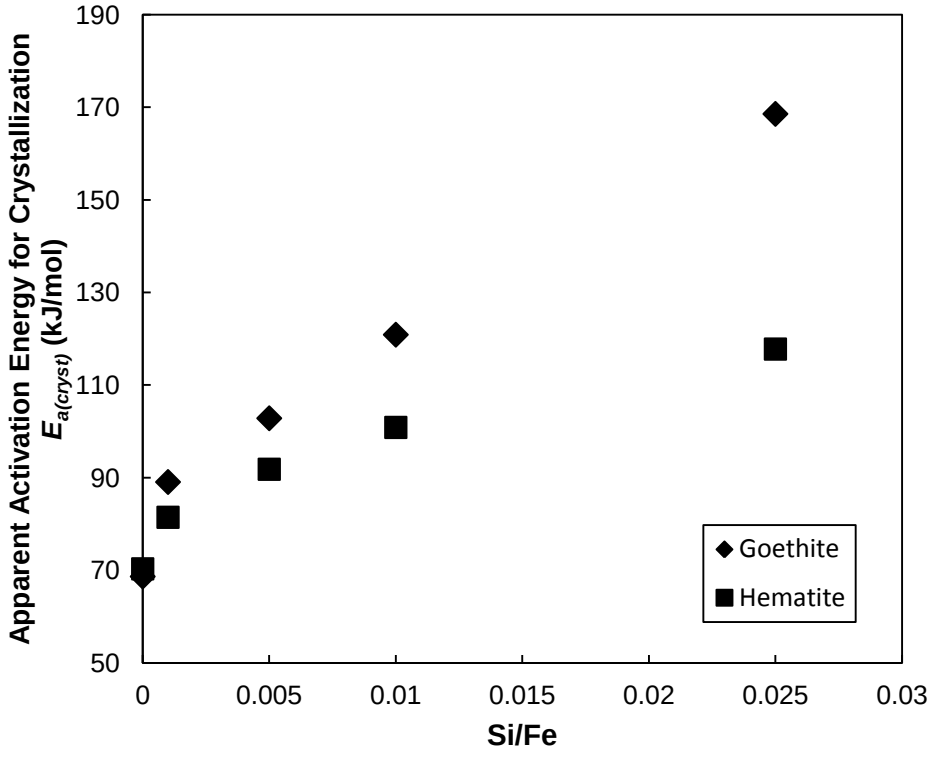

Fig. 9. Apparent activation energy for crystallization of hematite and goethite as a function of Si/Fe.

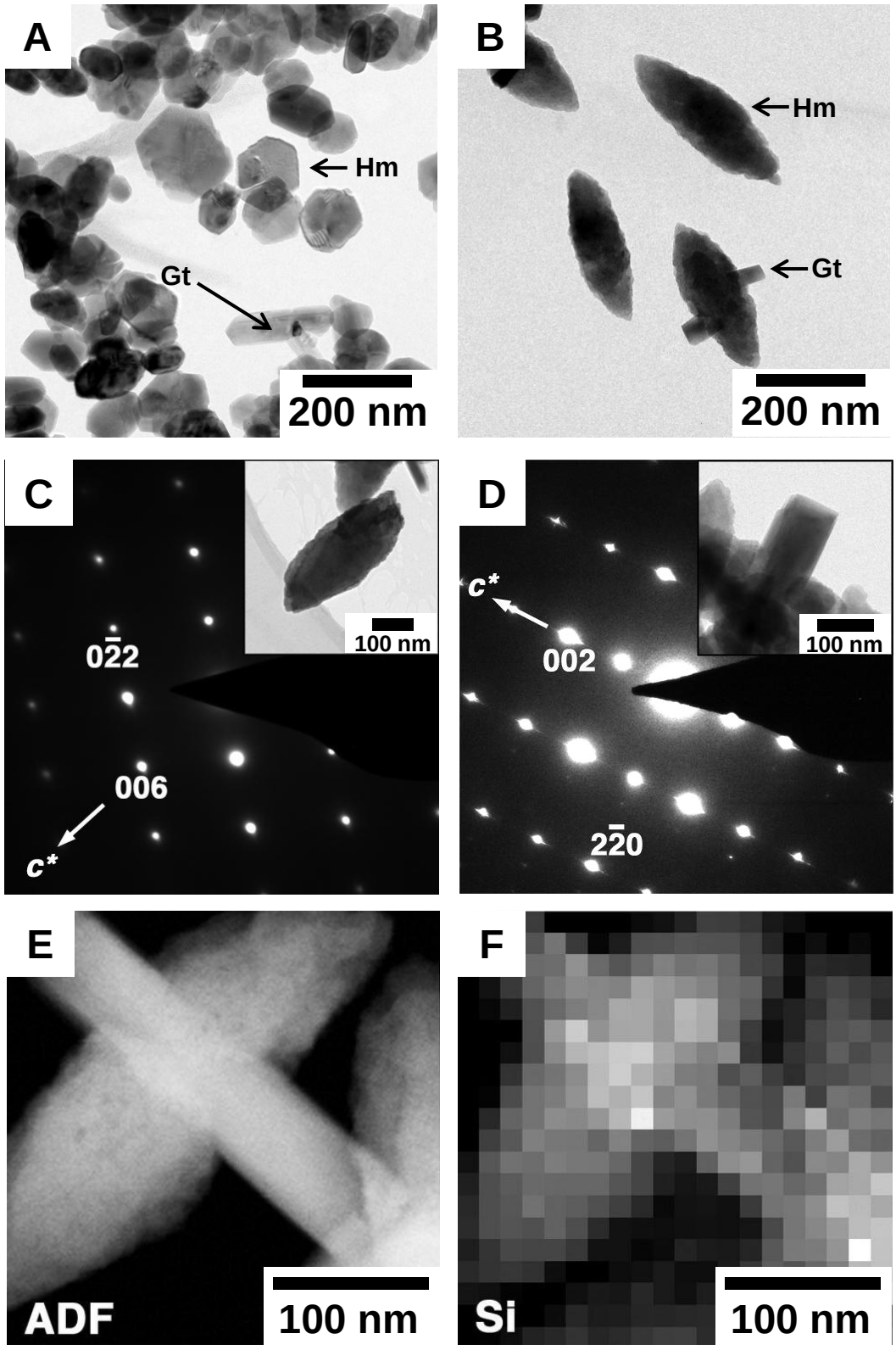

Fig. 10. TEM images of final reaction products extracted at 70°C: (A) Si/Fe = 0 after 8 hours and (B) Si/Fe = 0.025 after 48 hours. Electron diffraction patterns from (C) an ellipsoidal crystal as shown in (B) and (D) a lath-shaped crystal overgrown on the ellipsoidal crystal, which corresponds to hematite [100] and goethite [110], respectively. In (D), the forbidden reflections of 00*l* (*l*=2*n*+1) and *hk*0 (2*n*+1) appear due to multiple scattering. (E) TEM image of an ellipsoidal crystal with a lath-shaped overgrowth and a corresponding EDS map showing Si distribution in the two crystals. (*Gt*: Goethite; *Hm*: Hematite)

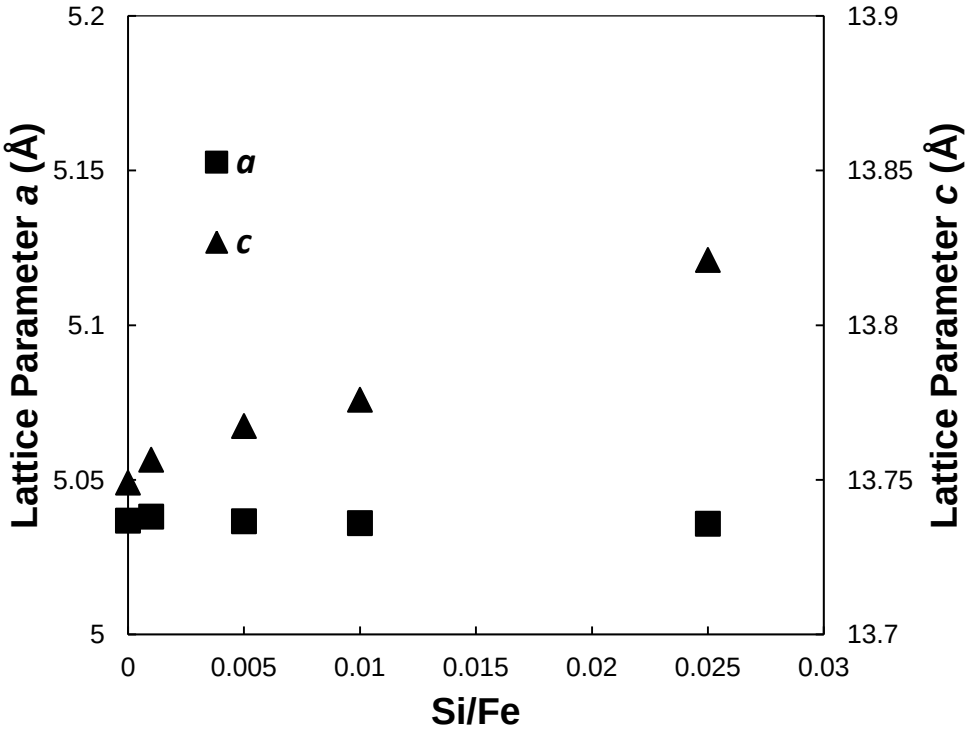

Fig. 11. Unit cell parameters for hematite as a function of Si/Fe ratio.

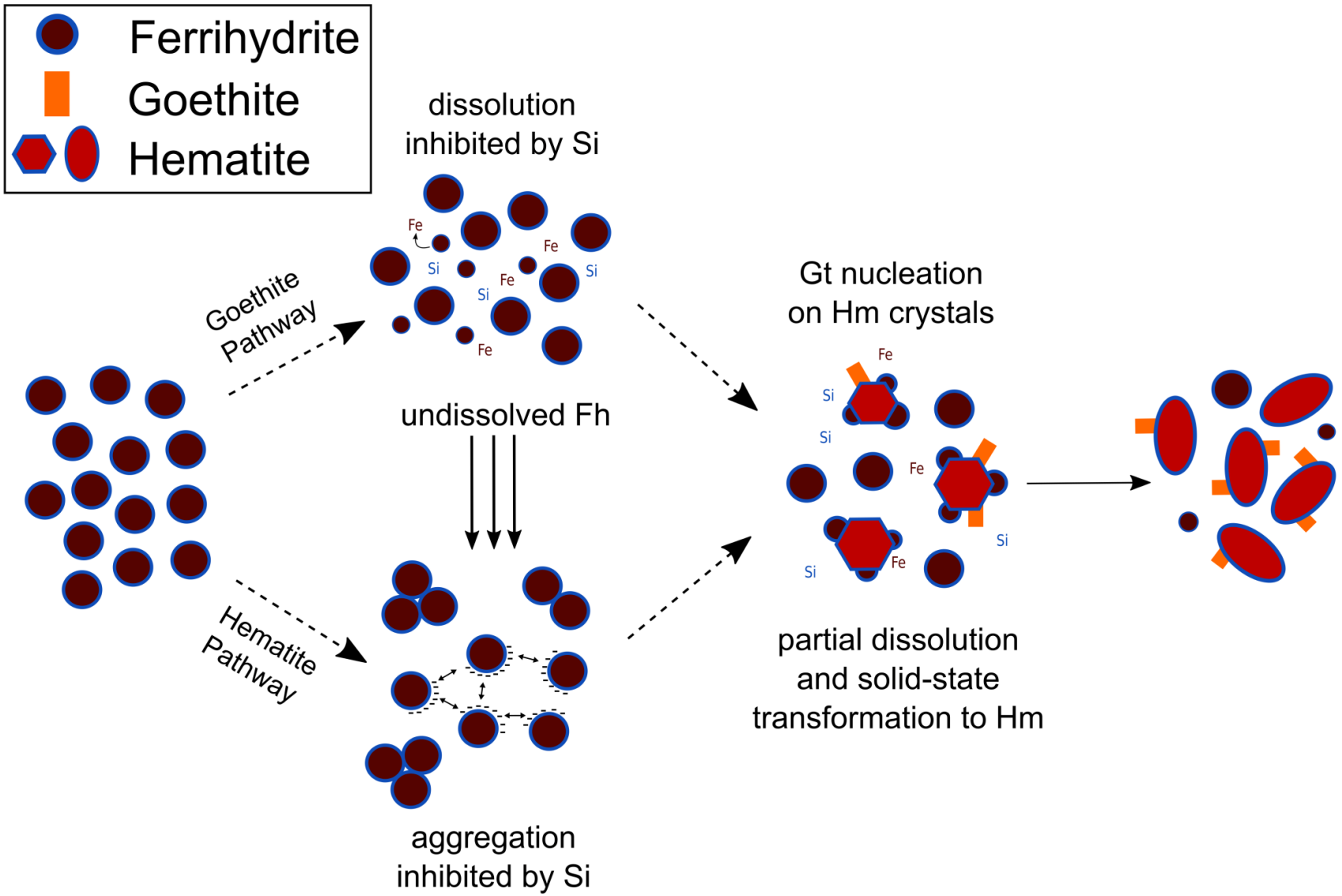

Fig. 12. Summary of the effect of Si on the crystallization of goethite and hematite

Supplementary Table S1. Table showing the relative percentages of each phases as calculated from Rietveld Refinement

50°C

Si/Fe = 0

Time (h)	Goethite	±	Hematite	±	Ferrihydrite	±	χ^2	R
3	11.06	2.82	8.23	2.24	80.72	6.42	7.03	0.346
6	34.20	13.62	18.34	7.37	47.46	39.15	8.21	0.208
9	71.38	3.59	28.62	2.06			8.02	0.205
12	74.50	3.69	25.50	1.92			8.66	0.252
26.5	74.36	3.50	25.64	1.85			7.28	0.263

Si/Fe = 0.001

Time (h)	Goethite	±	Hematite	±	Ferrihydrite	±	χ^2	R
3	12.53	1.22	8.62	0.87	78.85	7.41	4.59	0.257
6	34.75	13.31	18.65	7.16	46.60	38.13	6.31	0.189
9	68.97	135.08	31.03	60.77	0.00	195.81	9.02	0.187
12	69.28	1.74	30.72	1.03			6.05	0.195
26	72.31	2.87	27.69	1.56			7.28	0.236

Si/Fe = 0.005

Time (h)	Goethite	±	Hematite	±	Ferrihydrite	±	χ^2	R
3	7.54	1.18	11.98	1.12	80.48	6.65	5.06	0.301
6	14.17	2.83	22.95	4.37	62.88	18.61	6.01	0.224
9	30.73	26.70	46.53	40.42	22.73	86.83	4.96	0.188
12	40.71	1.27	59.29	1.55			6.04	0.188
25.5	41.21	1.16	58.79	1.44			5.18	0.199

Si/Fe = 0.01

Time (h)	Goethite	±	Hematite	±	Ferrihydrite	±	χ^2	R
3	3.06	1.74	5.19	0.92	91.75	2.67	4.24	0.396
6	5.29	1.31	19.68	2.08	75.03	9.48	4.66	0.296
10.5	6.33	1.98	37.06	9.31	56.61	24.84	5.45	0.253
12	8.16	3.84	48.55	21.51	43.29	44.16	5.47	0.244
25	13.97	1.49	86.03	3.28			5.76	0.214
49	14.75	1.64	85.25	3.62			6.08	0.223

Si/Fe = 0.025

Time (h)	Goethite	±	Hematite	Error	Ferrihydrite	±	χ^2	R
3				AMORPHOUS				
6	0	0	4.37	1.45	95.63	1.92	5.49	0.452
10.5	3.45	2.28	5.27	1.09	91.29	2.80	5.05	0.422
12	2.88	1.85	5.81	0.85	91.31	2.79	4.63	0.393
24	6.24	1.30	13.92	1.28	79.84	6.94	4.35	0.333
48	16.62	3.55	21.65	4.48	61.73	20.16	5.15	0.268
96	37.80	27.43	32.18	23.35	30.02	72.50	5.05	0.223

60°C

Si/Fe = 0

Time	Goethite	±	Hematite	±	Ferrihydrite	±	χ^2	R
1	3.70	1.24	5.25	0.94	91.05	2.99	4.93	0.386
2	11.57	1.57	14.86	1.75	73.57	10.42	4.7	0.284
3	21.38	5.96	24.24	6.73	54.38	27.53	5.62	0.211
4	52.93	1.94	47.07	1.86			8.17	0.203
5	54.16	2.69	45.84	2.39			9.86	0.216
6	51.20	2.84	48.80	2.72			8.57	0.268

Si/Fe = 0.001

Time	Goethite	±	Hematite	±	Ferrihydrite	±	χ^2	R
1	2.88	1.58	3.09	1.11	94.03	2.14	5.44	0.411
2	9.14	1.30	17.08	1.90	73.78	10.19	5.01	0.266
3	17.83	4.50	24.98	6.24	57.19	24.81	5.01	0.209
4	35.77	32.03	41.63	37.27	22.60	89.45	7.76	0.189
5	48.15	1.49	51.85	1.58			6.1	0.2
6	43.37	1.53	56.63	1.78			6.44	0.204

Si/Fe = 0.005

Time	Goethite	±	Hematite	±	Ferrihydrite	±	χ^2	R
1	2.33	1.42	4.22	0.98	93.46	2.26	4.56	0.423
2	4.83	1.09	13.63	1.18	81.54	6.18	4.96	0.324
3	11.08	2.20	25.47	4.74	63.45	18.31	4.93	0.226
4	17.77	7.65	39.49	16.92	42.74	42.77	5.4	0.2
5	30.42	1.03	69.58	1.63			5.12	0.184
6	29.67	1.37	70.33	2.32			6.07	0.214

Si/Fe = 0.01

Time	Goethite	±	Hematite	±	Ferrihydrite	±	χ^2	R
2	2.21	1.39	10.15	0.92	87.64	3.84	4.79	0.341
4	3.96	1.10	28.16	4.10	67.88	14.19	4.47	0.248
6	7.35	4.51	60.47	36.15	32.19	59.72	4.79	0.218
8	9.75	1.30	88.80	2.91			5.32	0.211
23	9.22	1.37	90.78	3.13			5.62	0.2

Si/Fe = 0.025

Time	Goethite	Error	Hematite	Error	Ferrihydrite	Error	χ^2	R
2				AMORPHOUS				
4			3.54	0.92	96.46	1.70	4.7	0.433
6	2.64	2.07	6.91	0.99	90.45	3.04	4.69	0.402
8	4.15	2.09	10.05	1.11	85.80	4.57	5.47	0.346
23	11.03	3.94	37.35	12.55	51.62	33.30	4.99	0.267
48	28.17	1.34	68.12	2.13	0.00	0.00	5.04	0.224

70°C

Si/Fe = 0

Time	Goethite	±	Hematite	±	Ferrihydrite	±	χ^2	R
1	5.31	1.81	21.34	2.74	73.35	10.57	5.21	0.296
1.5	10.66	3.90	37.17	12.32	52.17	32.71	6.43	0.223
2	16.79	11.98	50.72	35.80	32.49	70.42	7.52	0.199
2.5	24.30	1.69	71.85	2.75			6.52	0.187
3	28.62	1.51	71.38	2.77			6.05	0.222
3.5	23.69	2.30	76.31	4.31			8.14	0.227
4	24.94	4.02	75.06	7.17			8.01	0.263
8	26.56	2.95	73.44	5.12			7.06	0.24

Si/Fe = 0.001

Time	Goethite	±	Hematite	±	Ferrihydrite	±	χ^2	R
1	2.81	1.77	8.43	1.29	88.77	3.51	4.31	0.381
1.5	4.98	1.72	17.69	2.05	77.32	8.30	5.74	0.279
2	8.98	2.18	29.43	6.18	61.60	20.57	4.57	0.217
2.5	17.37	13.01	52.56	39.19	30.07	74.49	5.16	0.202
3	24.39	1.42	75.61	2.58			5.01	0.187
3.5	22.11	1.68	77.89	3.21			5.21	0.193

Si/Fe = 0.005

Time	Goethite	±	Hematite	±	Ferrihydrite	±	χ^2	R
1	3.31	2.25	5.82	1.06	90.87	2.87	4.69	0.395
1.5	1.83	1.33	10.11	1.04	88.07	3.73	5.32	0.367
2	4.49	1.21	20.37	2.12	75.14	9.35	4.93	0.288
2.5	5.83	1.60	33.61	7.11	60.57	20.87	5.77	0.225
3	9.86	7.91	62.54	49.70	27.60	79.42	5.23	0.209
3.5	13.57	1.01	86.43	2.23			4.87	0.193
4.5	13.92	1.04	86.08	2.34			5	0.187

Si/Fe = 0.01

Time	Goethite	±	Hematite	±	Ferrihydrite	±	χ^2	R
1	2.92	1.76	3.42	0.83	93.66	2.27	4.19	0.417
1.5	1.63	1.84	7.31	0.86	91.06	2.80	4.37	0.391
2	4.16	1.64	13.70	1.25	82.14	5.93	4.64	0.332
2.5	3.69	1.92	23.07	2.83	73.24	10.60	6.71	0.269
3	5.53	1.94	36.31	8.39	58.16	22.79	5.24	0.234
3.5	5.25	2.60	51.87	22.48	42.88	43.22	5.24	0.199
4	4.84	2.98	59.10	33.67	36.06	56.91	4.91	0.208
5	7.85	1.37	92.15	2.93			5.42	0.184

Si/Fe = 0.025

Time	Goethite	±	Hematite	±	Ferrihydrite	±	χ^2	R
2.5			3.25	0.85	96.75	1.83	4.56	0.384
3	3.03	1.84	3.98	0.85	92.99	2.27	4.7	0.417
5	2.53	1.75	12.41	1.12	85.06	4.83	5.12	0.332
6	5.17	2.26	17.24	1.94	77.59	8.12	6.16	0.312
30	8.30	2.55	88.34	6.09			6.28	0.291
48	9.78	1.61	90.22	3.96			5.27	0.242

80°C

Si/Fe = 0

Time	Goethite	±	Hematite	±	Ferrihydrite	±	χ^2	R
1	5.19	1.67	20.12	2.38	74.69	9.75	4.68	0.296
1.5	13.63	11.63	60.96	51.59	25.41	84.55	5.88	0.198
2	21.87	3.23	78.13	6.08			6.4	0.244
2.5	19.95	3.34	80.05	6.69			6.82	0.243
3	18.86	4.09	81.14	8.69			5.12	0.219
4	21.77	4.85	78.23	10.19			5.34	0.29

Si/Fe = 0.001

Time	Goethite	±	Hematite	±	Ferrihydrite	±	χ^2	R
1	4.63	2.02	19.73	2.52	75.64	9.31	5.64	0.305
1.5	8.36	3.04	38.80	12.16	52.85	30.93	5.68	0.237
2	18.41	1.53	81.59	3.05			5.59	0.175
2.5	17.61	2.48	82.39	5.09			6.05	0.227
3	17.11	1.73	82.89	3.63			5.89	0.236
4	18.12	1.67	81.88	3.38			5.89	0.239

Si/Fe = 0.005

Time	Goethite	±	Hematite	±	Ferrihydrite	±	χ^2	R
1	2.02	2.03	12.92	1.56	85.06	4.76	4.83	0.359
1.5	4.11	1.64	34.20	7.14	61.69	20.36	4.68	0.246
2	6.72	4.66	61.34	40.60	31.94	66.08	5.46	0.186
2.5	8.90	1.94	91.10	4.46			5.62	0.198
3	9.09	1.60	90.91	3.74			6.55	0.205
4	8.79	1.82	91.21	4.34			7.82	0.191

Si/Fe = 0.01

Time	Goethite	±	Hematite	±	Ferrihydrite	±	χ^2	R
1	2.87	2.28	12.12	1.44	85.01	4.80	4.54	0.35
1.5	3.03	2.19	29.49	4.85	67.48	14.94	6.11	0.259
2	3.42	1.81	45.71	15.16	50.87	32.93	4.57	0.204
2.5	5.48	6.27	78.99	87.48	15.53	110.69	4.75	0.195
3	5.89	1.13	94.11	2.57			4.49	0.172
4	6.04	1.13	93.96	2.50			4.34	0.189

Si/Fe = 0.025

Time	Goethite	±	Hematite	±	Ferrihydrite	±	χ^2	R
1			AMORPHOUS					
1.5			AMORPHOUS					
2			3.37	0.82	96.63	1.88	4.33	0.402
3			15.95	1.63	84.05	8.99	4.82	0.228
6			77.03	36.67	22.97	47.56	4.82	0.211
10			100.00	17.92			7.68	0.406
24			100.00	3.24			5.2	0.218

Supplementary Table S2. Average hematite crystal sizes measured from TEM

Average Hematite Sizes (nm)				
Sample	**Diameter[a]**	**σ**	**Length[b]**	**σ**
Si/Fe = 0[c]	122	27.3	63.4	14.1
Si/Fe = 0.025[d]	125	17.8	319	111.9

[a] Measured along the in-plane direction of the (001) plane (*a* axis).

[b] Measured along the *c* axis.

[c] Formed after 8 hours.

[d] Formed after 48 hours.

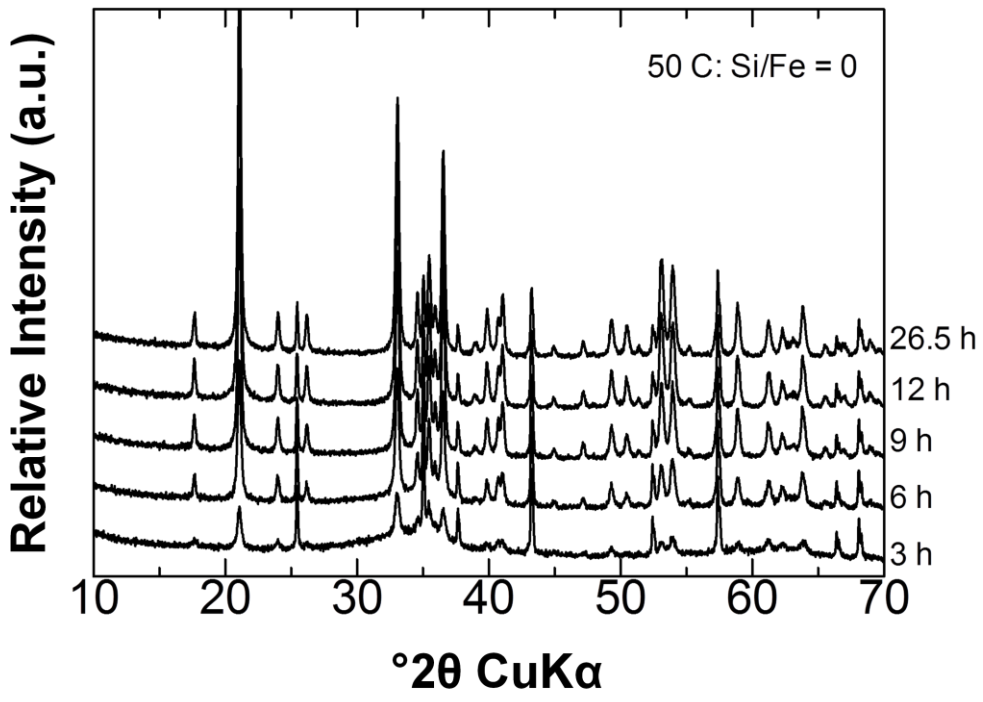
50 C: Si/Fe = 0
Relative Intensity (a.u.)
26.5 h
12 h
9 h
6 h
3 h
10
20
30
40
50
60
70
°2θ CuKα

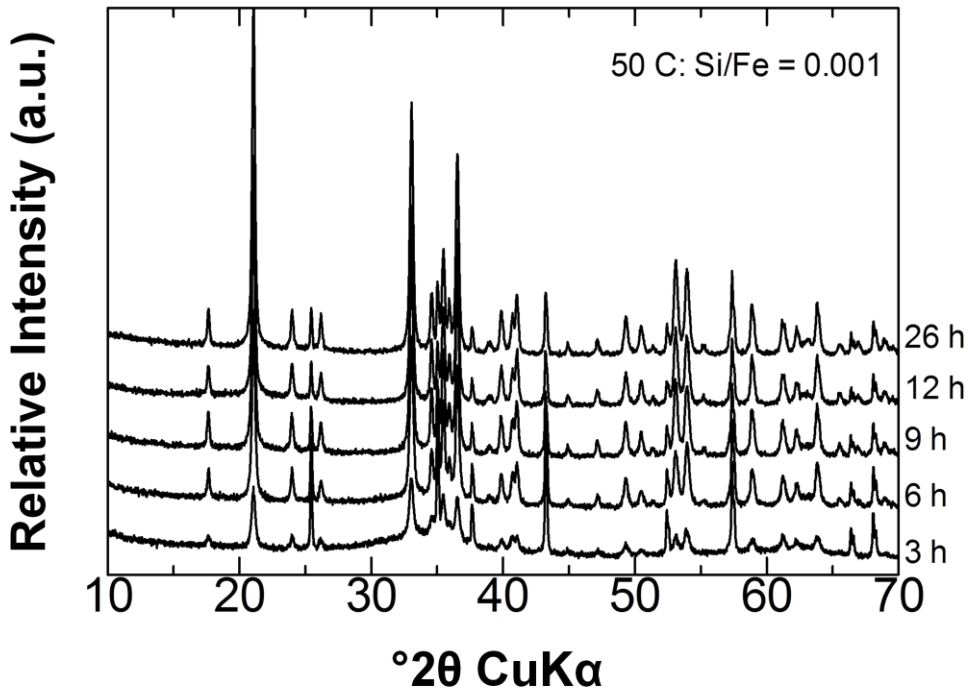
50 C: Si/Fe = 0.001
Relative Intensity (a.u.)
26 h
12 h
9 h
6 h
3 h
10
20
30
40
50
60
70
°2θ CuKα

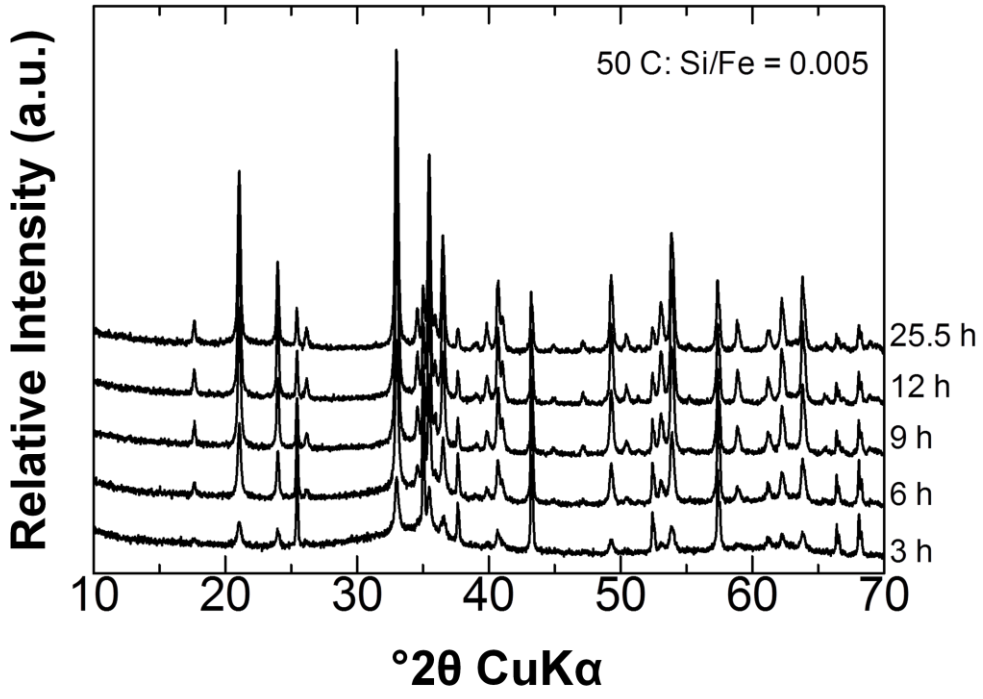
50 C: Si/Fe = 0.005
Relative Intensity (a.u.)
25.5 h
12 h
9 h
6 h
3 h
10
20
30
40
50
60
70
°2θ CuKα

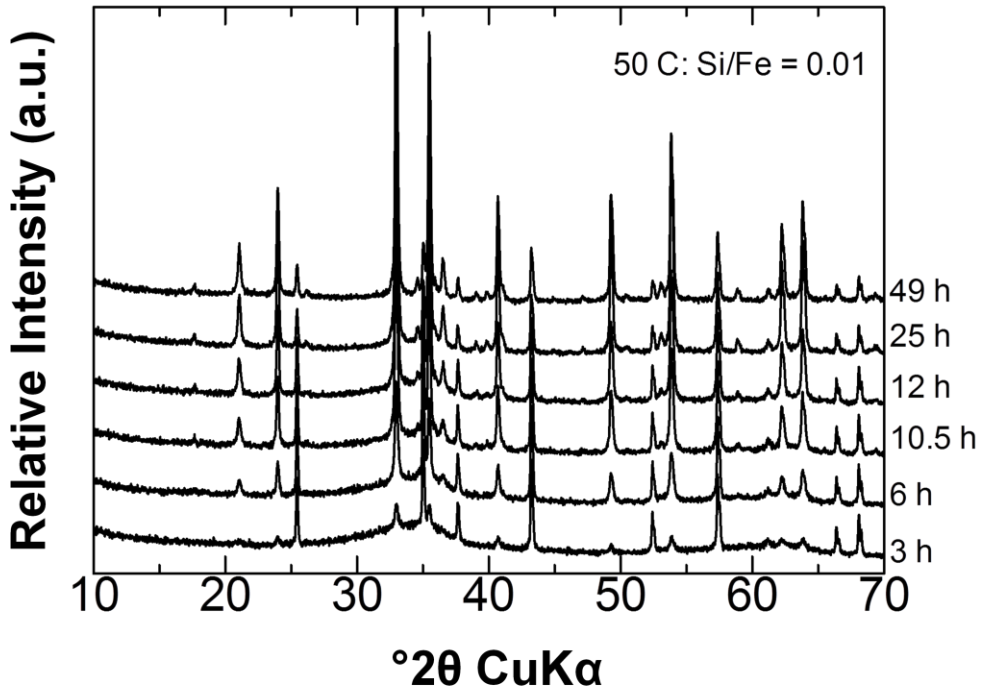
50 C: Si/Fe = 0.01
Relative Intensity (a.u.)
49 h
25 h
12 h
10.5 h
6 h
3 h
10
20
30
40
50
60
70
°2θ CuKα

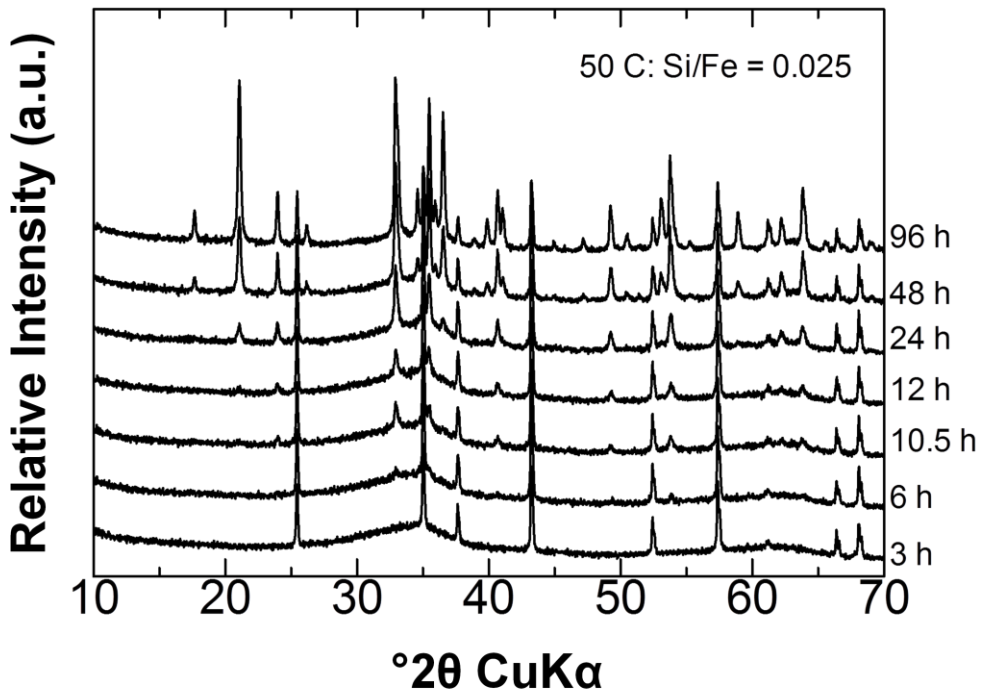
50 C: Si/Fe = 0.025
96 h
48 h
24 h
12 h
10.5 h
6 h
3 h
Relative Intensity (a.u.)
10
20
30
40
50
60
70
°2θ CuKα

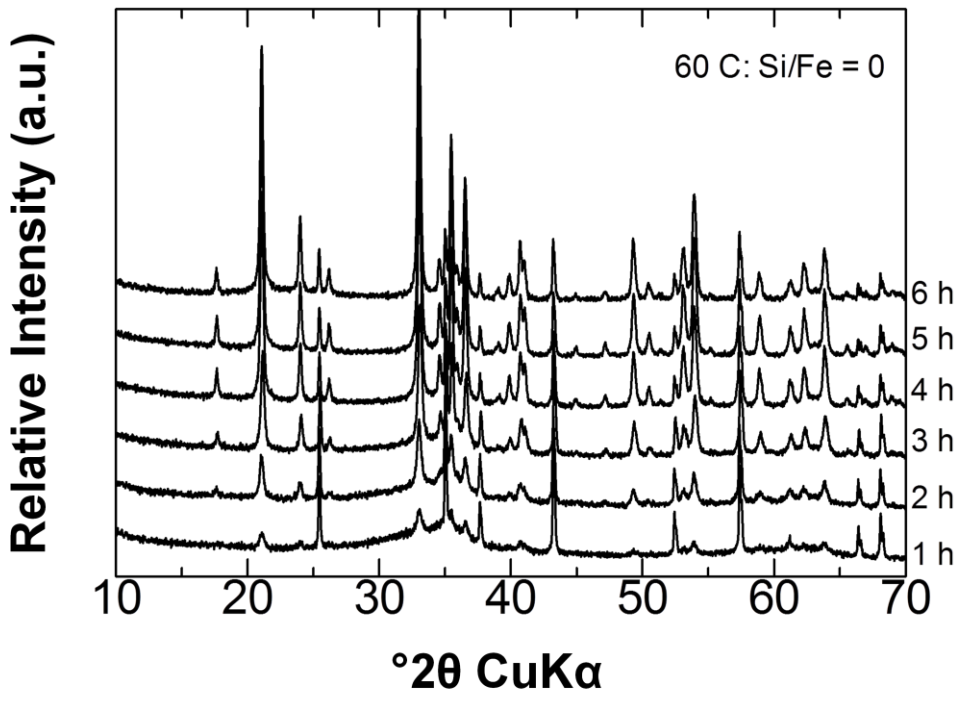
60 C: Si/Fe = 0
6 h
5 h
4 h
3 h
2 h
1 h
Relative Intensity (a.u.)
10
20
30
40
50
60
70
°2θ CuKα

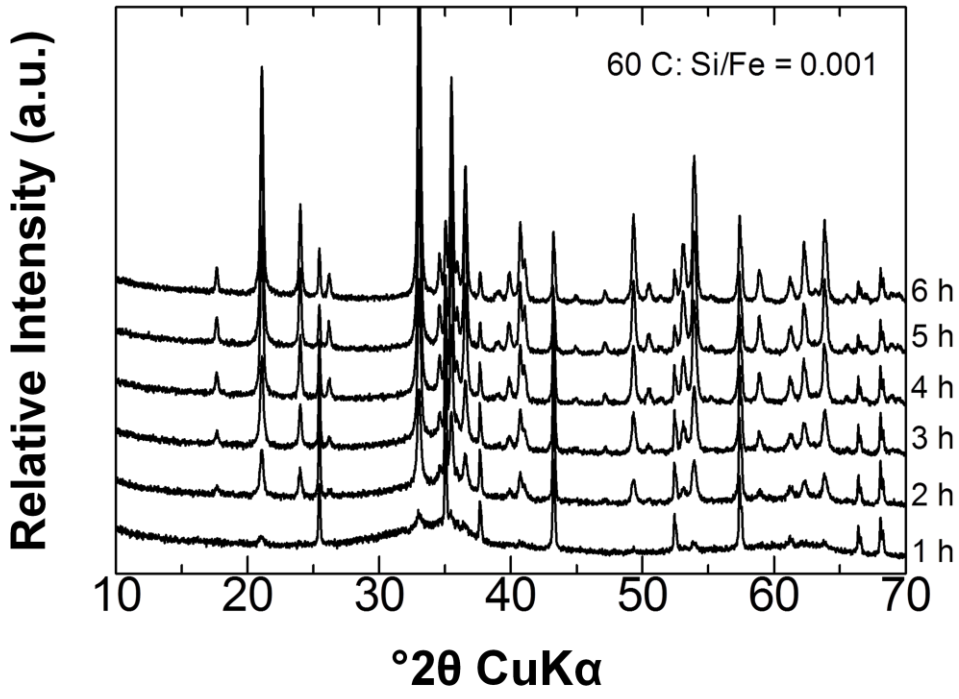
60 C: Si/Fe = 0.001
6 h
5 h
4 h
3 h
2 h
1 h
Relative Intensity (a.u.)
10
20
30
40
50
60
70
°2θ CuKα

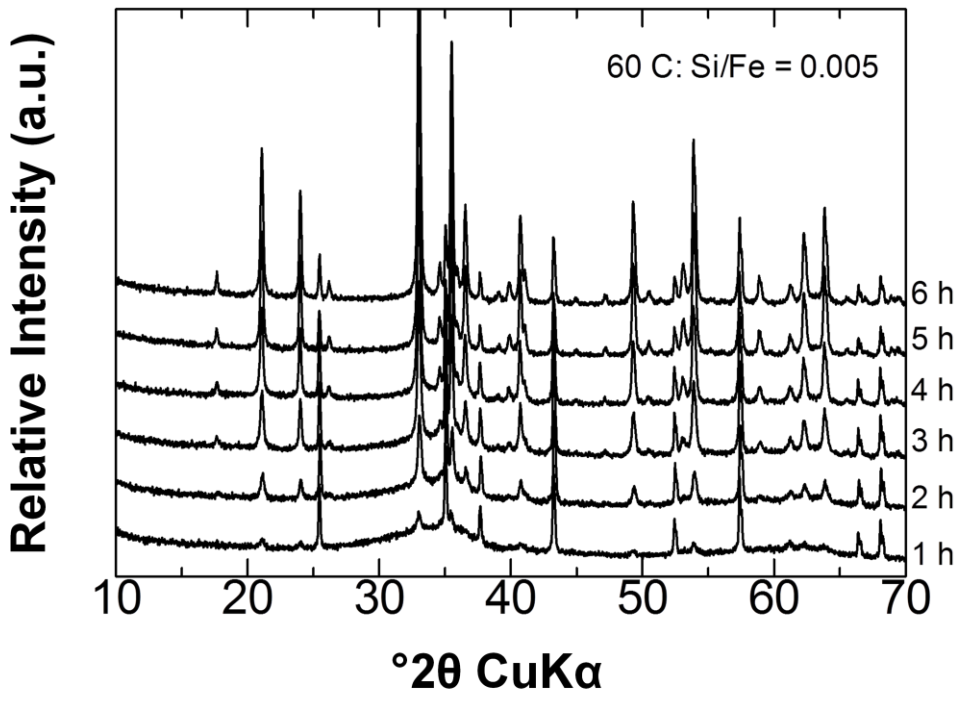
60 C: Si/Fe = 0.005
6 h
5 h
4 h
3 h
2 h
1 h
Relative Intensity (a.u.)
10
20
30
40
50
60
70
°2θ CuKα

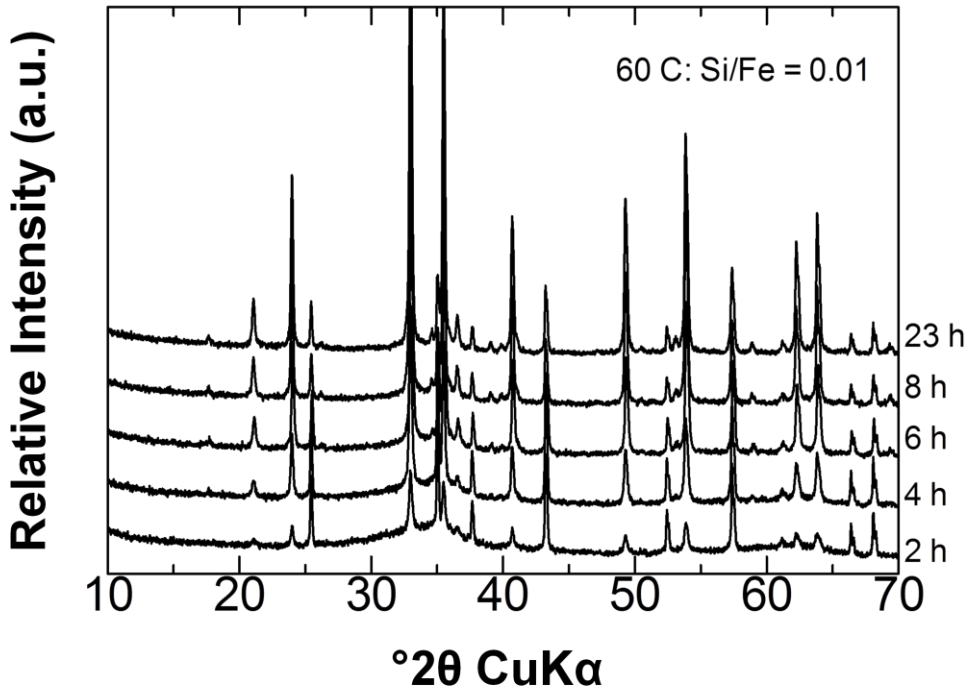
60 C: Si/Fe = 0.01
23 h
8 h
6 h
4 h
2 h
Relative Intensity (a.u.)
10
20
30
40
50
60
70
°2θ CuKα

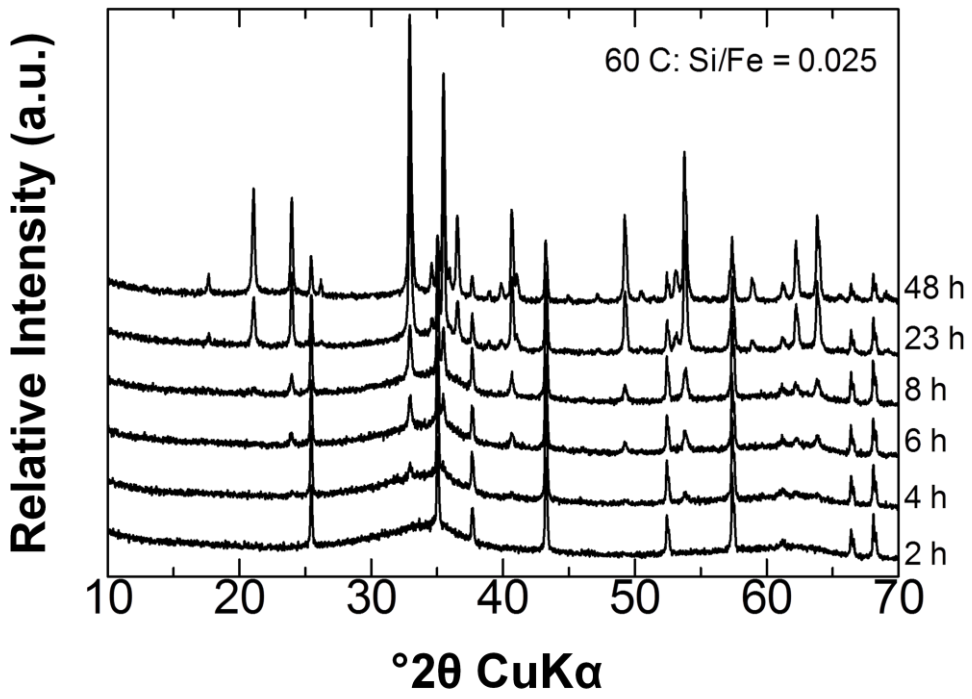
60 C: Si/Fe = 0.025
48 h
23 h
8 h
6 h
4 h
2 h
Relative Intensity (a.u.)
10
20
30
40
50
60
70
°2θ CuKα

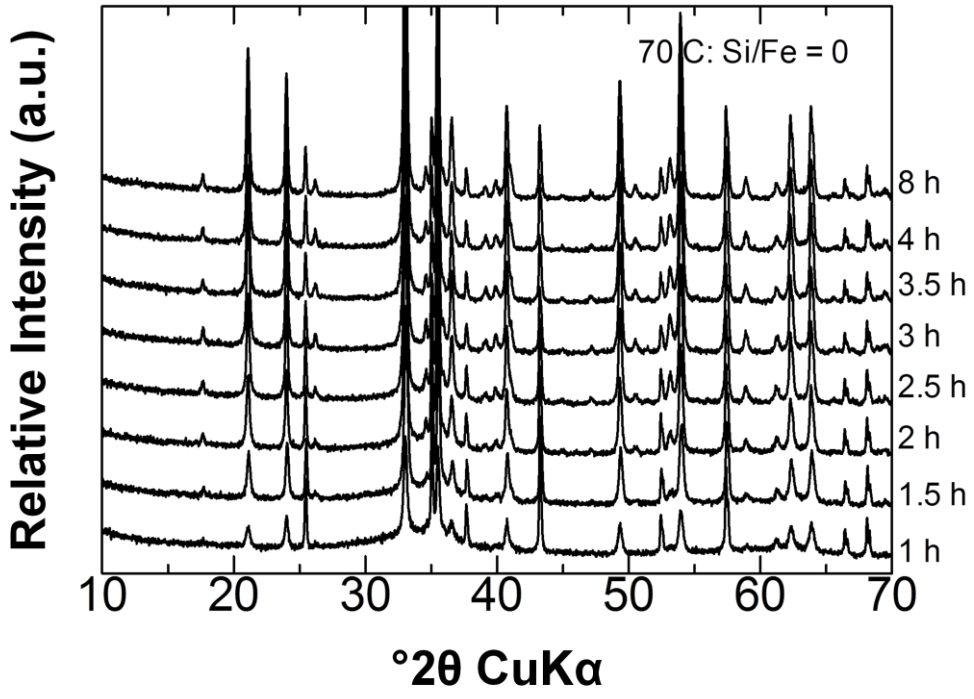
70 C: Si/Fe = 0
8 h
4 h
3.5 h
3 h
2.5 h
2 h
1.5 h
1 h
Relative Intensity (a.u.)
10
20
30
40
50
60
70
°2θ CuKα

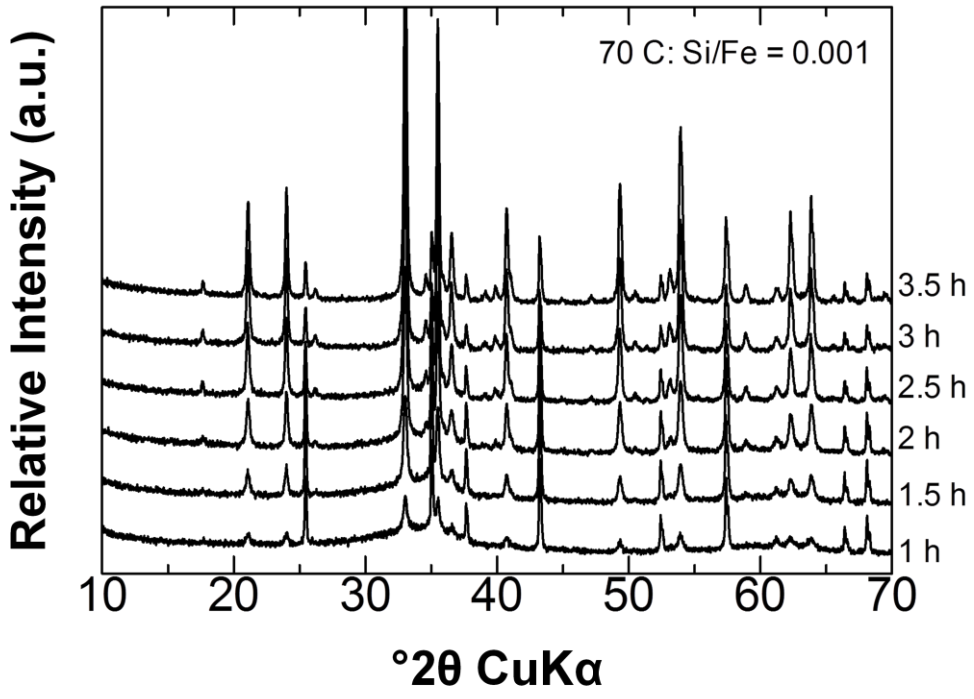
70 C: Si/Fe = 0.001
3.5 h
3 h
2.5 h
2 h
1.5 h
1 h
Relative Intensity (a.u.)
10
20
30
40
50
60
70
°2θ CuKα

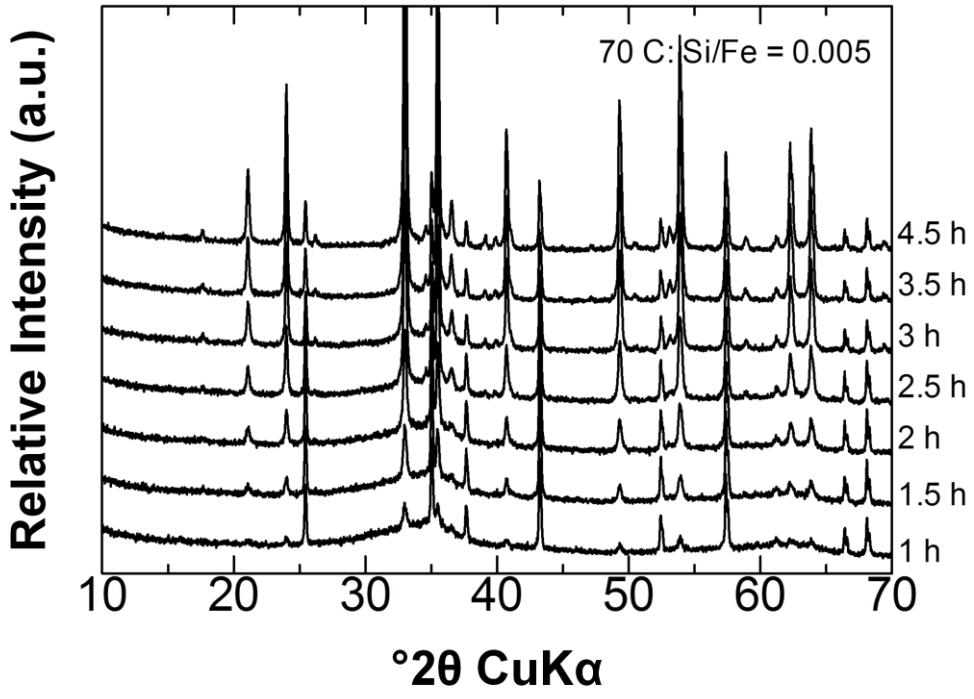
70 C: Si/Fe = 0.005
4.5 h
3.5 h
3 h
2.5 h
2 h
1.5 h
1 h
Relative Intensity (a.u.)
10
20
30
40
50
60
70
°2θ CuKα

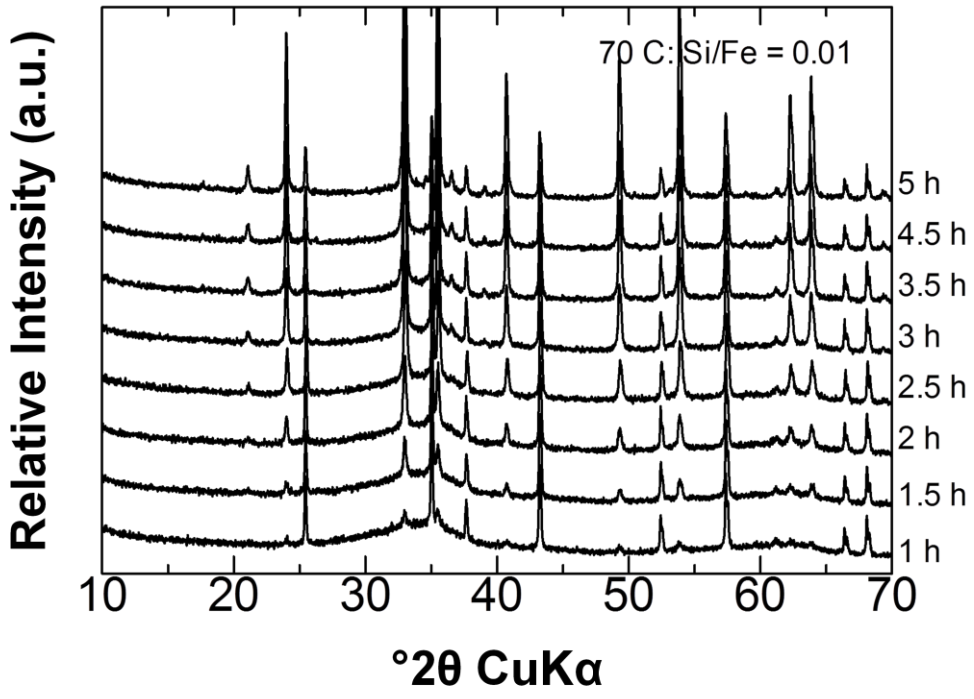
70 C: Si/Fe = 0.01
5 h
4.5 h
3.5 h
3 h
2.5 h
2 h
1.5 h
1 h
Relative Intensity (a.u.)
10
20
30
40
50
60
70
°2θ CuKα

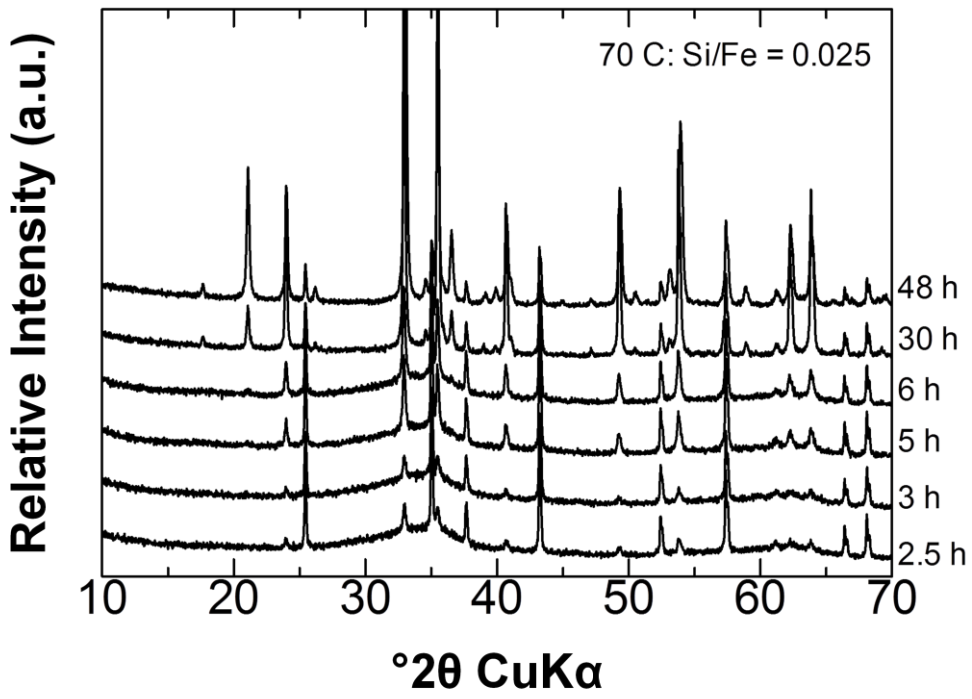
70 C: Si/Fe = 0.025
48 h
30 h
6 h
5 h
3 h
2.5 h
Relative Intensity (a.u.)
10
20
30
40
50
60
70
°2θ CuKα

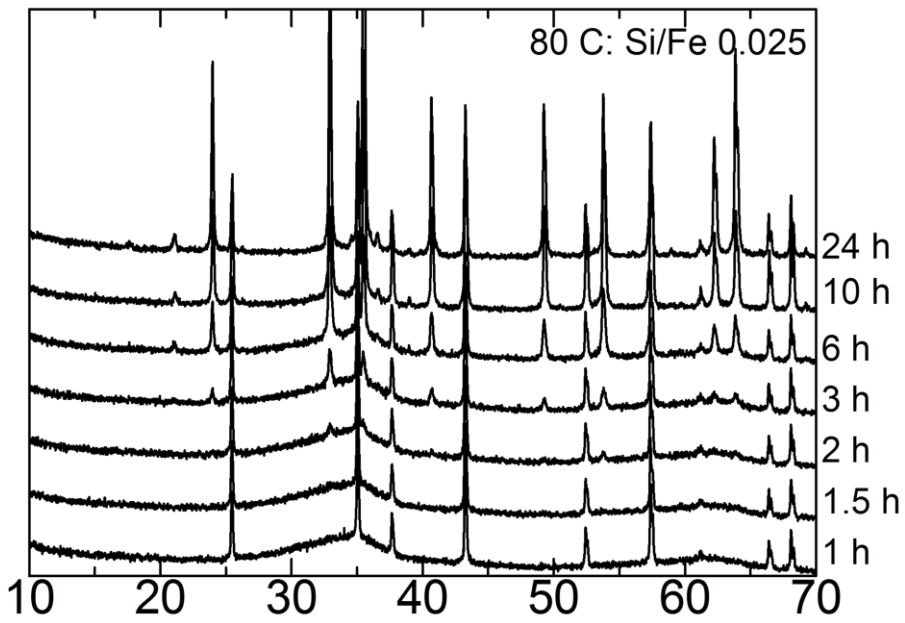

Fig. S1: XRD patterns of all the samples.

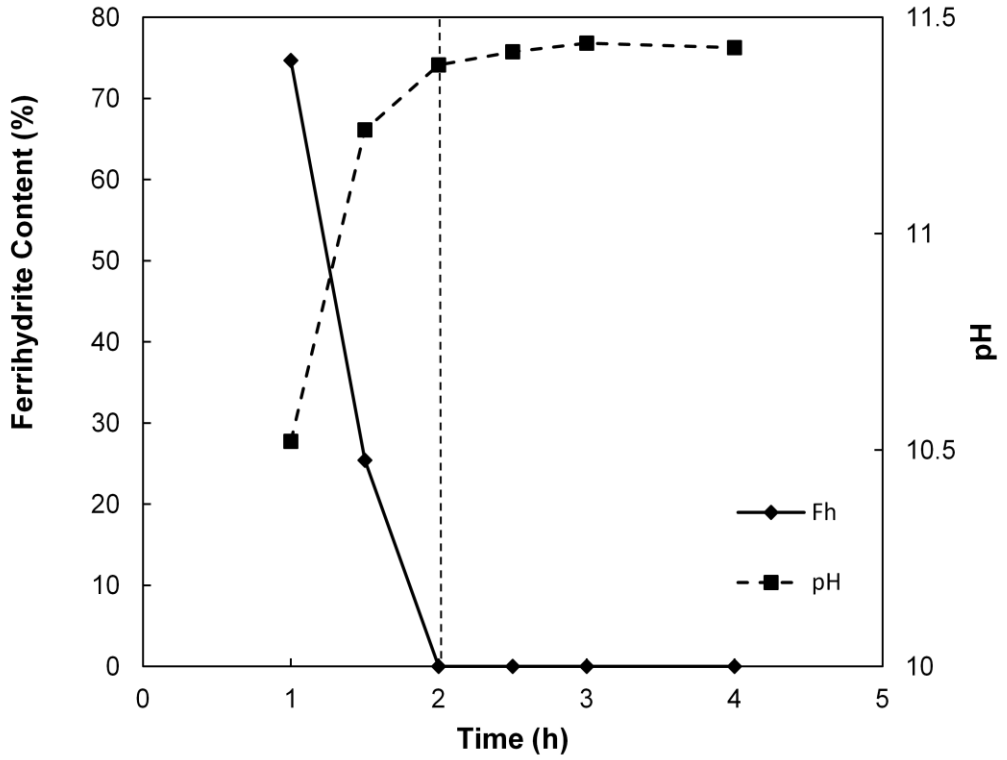

Fig. S2: Change in ferrihydrite content and pH as a function of time in Si/Fe = 0, 80°C.

CHAPTER 3: Fe(III) mineral transformation and its effects on the behavior of hazardous anions: Case study with Se(IV)

Part of this chapter has been submitted to *Journal of Colloid and Interface Science* as:

P.C.M. Francisco, T. Sato, T. Otake, S. Suzuki, H. Shiwaku, T. Yaita (2016). Behavior of co-precipitated Se(IV) during Fe-oxide transformation at alkaline conditions

3.1. Introduction

Iron (hydro)oxides are one of the most abundant minerals in the environment. Due to their high surface area and strong affinity for ions, they have been known as favorable sinks for environmentally important ions such as AsO_4^{3-}, PO_4^{3-}, CrO_4^{2-}, allowing them to control the transport and availability of these ions in natural waters (Stipp et al., 2002; Erbs et al., 2010). Fe-(hydro)oxides have also been used in industrial settings such as water and waste treatment facilities to minimize the concentrations of contaminants that may be released into the environment. In the context of geological disposal of radioactive wastes, the corrosion of the steel components of the engineered barrier system (e.g. the steel canister enclosing the vitrified waste) as a result of groundwater intrusion leads to the formation of crystalline Fe-(hydro)oxide phases such as goethite, hematite, magnetite and maghemite (Refait et al., 2003; Kwon et al., 2007; Hazan et al., 2013). These phases have been shown to be favorable sinks for radionuclides that may be released from the dissolving vitrified waste matrix (van Veelen et al., 2014).

^{79}Se is one of the long-lived fission products expected to be released from the vitrified waste. The speciation of Se is strongly dependent on the redox conditions as well as the pH. Under high pH and partly oxidized conditions in disposal environments, Se is likely present as the highly mobile selenite (SeO_3^{2-}) anion. The adsorption of selenite anions on crystalline Fe-oxides (e.g. magnetite, hematite, maghemite and goethite) as well as poorly crystalline Fe-hydroxides (e.g. ferrihydrite) has been the subject of numerous macroscopic geochemical investigations (e.g. Balistrieri and Chao, 1987, 1990; Zhang and Sparks, 1990; Su and Suarez, 2000; Rovira et al.,

2008; Duc et al., 2006; Missana et al., 2009; Jordan et al., 2014), which showed that Se(IV) adsorption is strongly dependent on pH, with adsorption favored at circum-neutral to acidic conditions. Detailed spectroscopic studies (e.g. Hayes et al., 1987; Manceau and Charlet, 1994; Catalano et al., 2006; Jordan et al., 2009) have shown that Se adsorbs on Fe-(hydro)oxide surfaces as inner-sphere complexes with a bidentate binding configuration.

However, at alkaline conditions expected in geological disposal repositories, uptake of Se(IV) by adsorption may be minimal. An alternative uptake mechanism that could potentially contribute to the immobilization of Se(IV) is co-precipitation with Fe phases, such as ferrihydrite. At the interface of dissolving glass and corroding steel, the hydrolysis of Fe(II) and Fe(III) may result in the rapid formation of poorly crystalline ferrihydrite (Cudennec and Lecerf, 2006). Co-precipitation occurs when the element of interest (i.e. Se(IV)) is present in the same aqueous solution when the carrier element (i.e. Fe) hydrolyzes and precipitates as iron hydroxides (Lu et al., 2011). Previous studies have shown that, compared to adsorption, co-precipitation with ferrihydrite presents a more efficient pathway to remove elements such as As, Ni (Crawford et al., 1993), Cr (Charlet and Manceau, 1992) and Zn (Waychunas et al., 2002) from aqueous solutions.

While the adsorption of Se(IV) on iron hydroxides has been extensively investigated, very little work has been done on Se(IV) co-precipitation (e.g. Merrill et al., 1987). In particular, the binding mechanism and stability of co-precipitated Se(IV) onto the ferrihydrite is poorly known. Recent studies on Se(IV) co-precipitation focused mostly on iron sulfides, such as pyrite and mackinawite (Diener and Neumann, 2011; Diener et al., 2012). These studies showed that Se(IV) was reduced to Se(0) and become incorporated into the structure of pyrite and mackinawite by substitution for S, presenting an effective retention pathway for Se. In the case of ferrihydrite, the binding mechanism of Se(IV) may be different, given that as a Fe(III) species ferrihydrite is not expected to reduce Se(IV).

The potential of ferrihydrite as a long-term sink for environmental contaminants depends on its ability to retain previously sequestered contaminants against remobilization. Remobilization may

occur if there are changes in the geochemical conditions (e.g. changes in pH; Zhang and Sparks, 1990) or by the transformation into thermodynamically stable assemblages. Due to its metastability, ferrihydrite readily transforms to crystalline phases such as goethite and hematite. The transformation process involves dissolution and re-precipitation in the case of goethite, and dehydroxylation and solid-state atomic rearrangement in the case of hematite (Cornell and Schwertmann, 2003). Depending on the transformation pathway, previously taken up ions may be retained or released. For example, while dissolution of ferrihydrite may lead to the release of contaminants immobilized by the ferrihydrite, aggregation of ferrihydrite particles may trap contaminants and prevent their release. Since these pathways operate at different pH conditions, the behavior of Se under different environments may also vary. In order to understand the long-term behavior and mobility of Se in disposal environments as well as in natural environments, it is important to investigate the behavior of previously sequestered Se during the transformation of an initial substrate. In particular, the mechanism by which Se is either released or retained is unknown. Furthermore, the mechanism of Se(IV) binding to the solid phases may change during transformation.

The main objectives of this study are to (i) investigate the uptake of Se(IV) by co-precipitation with ferrihydrite, (ii) observe the behavior of co-precipitated Se(IV) during ferrihydrite transformation to crystalline phases, and (iii) to determine the release or retention pathways for Se(IV) during transformation. To investigate the behavior of Se(IV) during phase transformation and the mechanisms of its release or retention, ferrihydrite was transformed at two different pH conditions (5 and 10), under which ferrihydrite transformation proceeds via different pathways. The binding mechanism of Se(IV) to both ferrihydrite and crystalline phases were then investigated using spectroscopic and chemical extraction methods.

3.2. Materials and Methods

3.2.1. Co-precipitation and Transformation Experiments

Co-precipitation of Se and Fe(III)-hydroxides/oxides was carried out by preparing Fe(III) solution by dissolving reagent grade $Fe(NO_3)_3 \bullet 9H_2O$ (Kanto, 99%) and mixing this solution with selenite solution prepared by dissolving Na_2SeO_3 (Kanto, 96%) to achieve concentrations of 0.05 M for Fe (III) and 50, 150, 250 ppm for Se(IV). All solutions were prepared using ultrapure water (18 MΩ•cm). The solutions were then purged of dissolved O_2 by bubbling with N_2 gas (99%) with constant stirring for approximately 24 hours until the dissolved O_2 was less than 0.1 ppm. The solutions were then titrated with NaOH (Kanto, 97%) to raise the pH to 5 and 10. During base titration, the initially clear, orange-colored solutions changed into dark brown-colored slurries, indicating the formation of poorly crystalline Fe-oxyhydroxides. The pH of the slurries was allowed to stabilize for about 30 minutes under constant stirring before the slurries were transferred into sealed, metal-jacketed, PTFE-lined bombs and stored in an oven preheated to 80°C to induce crystallization. Except for the heating step, all the experiments were conducted inside a glove box purged with N_2 gas until the ambient O_2 level is at approximately 0%.

The slurries were heated for up to 5 days. Samples extracted after the heating time underwent centrifugal separation to separate the solid and liquid fractions. Supernatants were filtered through 0.20 μm PTFE membrane filters, acidified using ultrapure HNO_3 (Kanto, 60%) and stored in a refrigerator prior to solution analyses. Solids were rapidly washed with deionized water to remove excess salts derived from the synthesis experiments and freeze-dried under vacuum conditions for at least 24 hours.

3.2.2. Sample Analyses and Characterization

Se concentrations in solution after separation from the solids were determined by inductively coupled plasma atomic emission spectroscopy using a Shimadzu ICPE-9000 ICP-AES.

The amount of Se taken up or retained by the solids was determined from the difference between the initial concentration of the precipitating liquid and the concentrations after co-precipitation / crystallization. To check the oxidation state of Se species in solution, non-acidified solution fractions were analyzed using the hydride-vapor generation method coupled with ICP-AES (Tamari, 1998). Sodium tetrahydroborate solution was prepared by dissolving $NaBH_4$ (Kanto) and NaOH (Kanto) in ultrapure water and 6.0 M acid solution was prepared from HCl (Kanto, 60%). Solution samples, along with the hydroborate and acid solutions, were fed via peristaltic pumps into a hydride vapor generator attached to a Shimadzu ICPE-9000 ICP-AES. The selective reaction of tetrahydroborate anions with reduced selenite species under acidic conditions produces volatile hydrogen selenide vapors that are then introduced into the ICP-AES via gas nebulizers. The results were then compared with the results of total Se concentration measured by standard ICP-AES.

Solid samples both before and after transformation were characterized by powder X-ray diffraction using a Rigaku RINT2000 X-ray diffractometer, which operates at 40 kV and 40 mA and is equipped with a Cu target and graphite monochromator. Rietveld refinement using the commercial SIROQUANT software (Taylor and Clapp, 1992) was performed for the post-transformation samples to estimate the proportion of crystalline products. XRD patterns were indexed according to the *Pnma* and $R\bar{3}c$ space groups for goethite and hematite, respectively. Refinement parameters include instrument zero, asymmetry factors, half-width and unit cell parameters and preferred orientation (Francisco et al., 2016).

To determine the partitioning of Se in the solid products both before and after crystallization, a series of chemical extraction experiments were conducted. The surface-bound fraction was extracted by finely disaggregating and dispersing the solids in 1.0 M Na_2HPO_4 (Kanto, 99%; pH ~9) for 12 hours. Due to the strong affinity of PO_4^{3-} anions to Fe-(hydro)oxide surfaces, PO_4^{3-} can easily exchange with surface-bound Se species. To ensure homogeneity, the suspensions were continuously agitated using a rotary mixer. The extracting solution was separated from the solids by centrifugal separation, filtered through 0.20 μm PTFE membrane filters and acidified for ICP-AES

analysis. The remaining solids were washed with deionized water, freeze-dried then completely dissolved in 6.0 M HCl at 110°C using a heating block, with the acid being allowed to evaporate (Yokoyama et al., 1983). This dissolution procedure was repeated 3 to 4 times until all of the solids have been dissolved. The residues resulting from the evaporation of the acid were then re-dissolved in 4.0 M HNO_3 for analysis by ICP-AES.

Se K-edge XAS spectroscopy was conducted at beam line BL11XU of the SPring-8 Synchrotron Facility (Hyogo, Japan), which operates at energies of up to 8 GeV. X-ray beam energy was tuned using a Si(311) crystal monochromator and calibrated using elemental selenium powder (Se^0). Samples were prepared by mixing and powdering the samples with an inert boron nitride matrix (Chameleon Reagent, 99.5%) to minimize self-absorption effects at a ratio of 10 wt. % sample to 90 wt. % matrix. The powdered mixtures were then pressed into pellets and mounted normal to the incident beam. Spectra were collected at room temperature in transmission mode using a type S-1194B1 ionization chamber (Oken). Measurements were collected up to forty times and averaged to increase the signal-to-noise ratio. Data reduction (background subtraction, normalization) and processing (Fourier transformation, EXAFS modeling) were conducted using the DEMETER software package (Ravel and Newville, 2005), which implements IFEFFIT algorithms for XAS data analysis. Modeling of normalized EXAFS data was performed using model single scattering paths generated using ATOMS from crystallographic data for Na_2SeO_3 (Wickleder, 2002) and $BiFe(SeO_3)_3$ (Zhang et al., 2012). A shell-by-shell fitting approach (Kim et al., 2004; Erbs et al., 2010) was implemented wherein the first coordination shell was first isolated and fitted to derive values for the energy shift (ΔE_0), amplitude reduction factor (S_0), coordination number (*CN*) and inter-atomic distance (*R*). The values of ΔE_0 and S_0 were then used to model the second coordination shell while fixing the *CN* and *R* values of the first shell. The values of the disorder parameter σ^2, which is highly correlated with *CN*, were initially fixed at 0.005 for the first shell and 0.01 for the second shell to derive the *CN* values and then allowed to vary later.

3.3. Results

3.3.1. Transformation of Ferrihydrite at pH 5, 10 and 80°C

At both pH 5 and 10, ferrihydrite was transformed predominantly to hematite, identified by XRD analyses. However, at pH 10, peaks corresponding to goethite are also observed in the XRD spectrum (Fig. 1). The results of Rietveld refinement show that the crystallization products at pH 10 consist of ~10% goethite and ~90% hematite (SI, Table 1). Diffraction peaks corresponding to other phases (e.g. Fe(III)-selenite) are not observed at either pH 5 or 10.

3.3.2. Fate of Se(IV) During Ferrihydrite Transformation

Analyses of solutions immediately after co-precipitation show that the majority of Se(IV) was sequestered from solution, with the uptake fraction being slightly higher at pH 5 (~100%) than at pH 10 (~94%) as shown in Figure 2. Furthermore, the behavior of Se(IV) during ferrihydrite transformation is also dependent on pH. At pH 5, the concentration of Se(IV) in solution remains low, close to the ICP-AES detection limit, indicating that it is not released during transformation and is thus fully retained in the crystalline solids. On the other hand, at pH 10, Se(IV) concentration increased during transformation, indicating the release of Se(IV) back into solution. Based on the concentration of the Se(IV), only ~43% of the original Se(IV) was retained in the crystalline solids (Fig. 2).

3.3.3. Partitioning of Se(IV) in the Solid Products

Figure 3 shows the results of chemical extraction experiments. At both pH 5 and 10, and in both the initial ferrihydrite and post-transformation crystalline solids, Se(IV) is present as phosphate

and acid-extractable species, although the proportion of each species varies with pH and the degree of crystallinity of the solids. At pH 5, the acid-extractable fraction accounts for a significant proportion of the Se(IV) co-precipitated with the ferrihydrite (~80 %), with the phosphate extractable fraction accounting for only ~20 %. In contrast, at pH 10, the Se(IV) is distributed approximately evenly between phosphate (~58%) and acid-extractable (~41%) species (Fig. 3). Following transformation, the proportion of acid-extractable Se(IV) relative to the phosphate-extractable species increased to ~93 % and ~86% at pH 5 and 10, respectively.

3.3.4. Se K-edge X-ray Absorption Spectroscopy

The Se K-edge XANES spectra of the initial ferrihydrite and post-transformation solids from pH 5 and 10 are shown in Figure 4. All samples exhibit strong white lines at ~12,660 eV, which closely matches the edge position of the Se(IV) standard, indicating that Se largely retains its tetravalent oxidation state. These results show that within the timescale of these experiments, Se(IV) did not undergo extensive oxidation. Differences in the post-edge features are also observed in the samples. In the samples from pH 5, post-edge features at ~12,740 eV appear in the ferrihydrite and post-transformation solids, indicating similarities in the coordination environment of Se(IV). In contrast, in the pH 10 samples, a weak post-edge feature is observed in the initial ferrihydrite at ~12,760 eV. This feature becomes more pronounced and shifts to lower energies in the post-transformation solids, suggesting changes in the local environment of Se(IV) following transformation at pH 10.

Normalized Se K-edge EXAFS spectra and their corresponding Fourier transforms are shown in Figure 5. Comparison of the k^3-weighted EXAFS spectra reveals differences between solids formed at different pH and between solids with different degrees of crystallinity. While initial ferrihydrite and post-transformation solids formed at pH 5 do not show significant differences, the ferrihydrite from pH 10 shows clear differences with the corresponding post-transformation product.

For example, the second oscillation in the post-transformation solid is shifted to slightly higher *k* values and is distinctly more asymmetric compared to that of the freshly co-precipitated solid. Along with the XANES spectra, this suggests that the local environment of Se(IV) changed during transformation at pH 10. Furthermore, the EXAFS spectra of the post-transformation solid formed at pH 10 resembles the spectra of those formed at pH 5, which may suggest similarities in the local environment of Se(IV).

The Fourier transforms for all the samples exhibit strong features corresponding to a first coordination shell consisting of O atoms. These features can be fitted with ~3 O atoms at distances ranging from ~1.68 to 1.70 Å (Table 1), consistent with the trigonal pyramid structure of the selenite anion (Eklund et al., 2014). Although somewhat weak, features arising from possible contributions from second coordination shells can also be observed in the Fourier transforms. In the pH 5 solids, these features can be fitted with ~2.8 Fe atoms at ~3.30 Å (Table 1). In contrast, the solids at pH 10 exhibit differences in the number of the Fe atoms. The feature in the ferrihydrite can be fitted with ~1 Fe atom at a distance of ~3.30, while the feature in the crystalline solid can be fitted with ~2.6 Fe atoms. Although there is considerable uncertainty in the second shell coordination numbers and inter-atomic distances, the fitting results may point to a bidentate, binuclear corner-sharing configuration between one SeO_3^{2-} anion to two FeO_6 octahedra (Xiao et al., 2004; Jordan et al., 2014).

3.4. Discussion

3.4.1. Mechanisms of Se(IV) Release and Retention

The difference in the behavior of Se(IV) during transformation at different pH may be explained by differences in the transformation pathway of ferrihydrite. This is supported by the observed assemblage of the post-transformation phases. The solubility of ferrihydrite is at a

minimum at circum-neutral pH (Cornell and Schwertmann, 2003). Thus, at pH 5, ferrihydrite does not dissolve significantly, which may explain the absence of goethite in the observed post-transformation products at pH 5. Furthermore, at this condition, the surface charge of ferrihydrite is approximately zero, which favors the aggregation of ferrihydrite particles, leading to the formation of hematite. In contrast, at pH 10, ferrihydrite solubility is markedly higher, leading to the formation of goethite. Thus, since Se(IV) was only released at pH 10, the release may be attributed to the dissolution of the ferrihydrite.

3.4.2. Changes in Se(IV) Speciation During Transformation

The results of the chemical extraction experiments show that the bulk of Se(IV) in the solids can only be extracted by acid dissolution, this suggests that Se(IV) are located in non-surface sites, inaccessible to phosphate exchange. The EXAFS results may reveal more information on the nature of the Se(IV) in the solids. In the ferrihydrite samples at pH 5 and 10, the second shell features can be fitted with ~1 Fe atom. While this may be consistent with a mononuclear edge-sharing complex, which is typically observed in ferrihydrite due to a high proportion of edge sites (Manceau and Charlet, 1994), the Se-Fe inter-atomic distances of ~3.25 to 3.32 Å are significantly longer than the distances typically expected for edge-sharing complexes (~2.4 to 2.9 Å; Catalano et al., 2006; Missana et al., 2009). These distances, however, fall well within the range of distances observed for bidentate binuclear corner-sharing complexes involving one Se(IV) pyramid and two Fe octahedra (~2.9 to 3.3 Å; Catalano et al., 2006; Missana et al., 2009; Jordan et al., 2014). This configuration is similar to that observed for adsorbed Se(IV) on iron (hydro)oxides (e.g. Hayes et al., 1987; Manceau and Charlet, 1994; Missana et al., 2009; Jordan et al., 2014). The rather low Se-Fe coordination numbers may be attributed to the high uncertainties associated with the fitting or to strong disorder in the ferrihydrite structure. Thus, co-precipitated Se(IV) is present mainly as an adsorbed species in the ferrihydrite samples at both pH 5 and 10.

Co-precipitation with ferrihydrite involves a complex set of processes. Recent studies on the co-precipitation of metals such as Pb (Kelly et al., 2009; Lu et al., 2011) have shown that incipient ferrihydrite particles begin to precipitate at pH of ~3 to 4. Ions in solution adsorb to these nanosized particles, which then coalesce into larger particles, trapping previously adsorbed ions between particle aggregates. The results of the EXAFS fitting, which point to Se(IV) as an adsorbed species is consistent with this mechanism. Furthermore, the trapping of adsorbed Se(IV) between particle aggregates may explain the bulk of Se(IV) that can only be liberated by acid dissolution of the ferrihydrite.

After transformation, the results of the EXAFS fitting show an increase in both the Se-Fe coordination numbers (~2.1 to 2.6 Fe atoms) and inter-atomic distances (~3.29 to 3.37 Å) at pH 5 and 10. These values are, however, within the uncertainties of the values derived for the ferrihydrite and are still consistent with bidentate binuclear corner-sharing complexes, indicating that Se(IV) is likewise present as an adsorbed species in the post-transformation crystalline solids. An alternative interpretation of Se(IV) configuration in the crystalline solids is the formation of discrete precipitates of Fe(III)-selenite. The precipitation of hydrous Fe(III)-selenite has been previously proposed as contributing to the retention of Se(IV) in iron (hydro)oxides (Duc et al., 2006, Missana et al., 2009). Based on EXAFS data, the feature corresponding to the second coordination shell in the post-transformation solids from pH 5 and 10 can be fitted with ~2.1 to 2.6 Fe atoms at a distance of ~3.29 to 3.36 Å, which is similar to the Se coordination environment observed in hydrous Fe(III)-selenite (Giester and Pertlik, 1994). However, no other phase apart from goethite and hematite was detected in the XRD patterns of the post-transformation solids, indicating the absence of a crystalline Fe(III) selenite phase. Furthermore, the lack of a Se-Se backscattering at ~4 Å, which is typical of crystalline Fe(III) selenite (Giester and Pertlik, 1994), in the transformed samples at either pH 5 and 10 indicates the absence of a Fe(III) selenite precipitate. While it is possible that amorphous Fe(III) selenite was formed, this is unlikely given that the samples have been aged at 80°C.

Another alternative interpretation is direct incorporation of Se(IV) in the crystalline phases. This may come in the form of isomorphous substitution of Se for Fe in the goethite and / or hematite structure or by incorporation in crystal defect sites. Isomorphous substitution may occur if there is a small difference in the ionic radii (< ± 18 % difference; Cornell and Schwertmann, 2003). Se may thus be able to substitute for Fe in the goethite and / or hematite structure since there is only a ~14% difference in their ionic radii (Fe^{3+}: 0.64 Å; Se^{4+}: 0.50 Å). Typically, isomorphous substitution of another ion for Fe in a mineral structure results in the distortion of the crystal lattice, which is manifested as changes in the lattice parameters of the crystal. For example, the substitution of Cd^{2+} for Fe^{3+} results in a significant increase in the lengths of all three axes of the goethite lattice (Sileo et al., 2003). In this study however, no differences were observed in the lattice parameters for goethite and hematite in the post-transformation solids relative to those formed in the absence of Se, which may be explained by the small size difference between Se and Fe. However, EXAFS data showed that the number of O atoms surrounding Se did not change during transformation, which indicates that Se retained its trigonal pyramid geometry. This would make Se structurally incompatible with either goethite or hematite, both of which are characterized by Fe in octahedral coordination (Cornell and Schwertmann, 2003), making direct incorporation of Se(IV) in the crystalline solids unlikely. This behavior of Se(IV) is in stark contrast to the behavior of previously studied elements such as U (Marshall et al., 2014) and Mo (Brinza et al., 2015), which were structurally incorporated into crystalline phases (hematite). Unlike Se(IV), these elements are able to assume an octahedral configuration, allowing them to incorporate within the structure of crystalline iron oxides by substitution for Fe. This implies that structural retention of hazardous elements depend in large part to whether an element could assume a structure compatible with a host phase.

The interpretation that Se(IV) exists as adsorbed species in the crystalline phases is apparently inconsistent with the results of the chemical extraction experiments, which showed that only a very small amount of Se(IV) can be liberated by phosphate extraction. This may suggest that

adsorbed Se(IV) may be present in sites that are not accessible to phosphate exchange. Such sites may include micro/nanopores that arise along grain and domain boundaries between goethite and hematite crystals formed from ferrihydrite transformation (Schulze and Schwertmann, 1984; Echigo et al., 2013). These features have been known to be favorable sites for metal retention (Bibak et al., 1995; Ford and Bertsch, 1999). The retention of Se(IV) in such sites may proceed under conditions at which ferrihydrite aggregation is favored. A similar mechanism was discussed previously by Vu et al. (2013) on the incorporation of Pb in hematite during ferrihydrite transformation. The aggregation of ferrihydrite, as a prelude to hematite crystallization, trapped Pb within the aggregates. During solid-state transformation to hematite, the trapped Pb was not released, being entrained in the resulting post-transformation assemblage. This scheme of Se(IV) retention in crystalline post-transformation assemblages also show that though Se(IV) is present only as an adsorbed species, it is not easily mobilized by changes in chemical conditions (e.g. changes in pH, presence of other strongly adsorbing ligands). This suggests that Se(IV) retention in crystalline phases is stable.

3.5. Conclusions

This work highlights the behavior of Se(IV) co-precipitated with ferrihydrite during phase transformations. Depending on the pH, Se(IV) may be partially remobilized, with alkaline conditions favoring the release of Se(IV) during transformation. This may be explained by the different transformation mechanisms of ferrihydrite at different pH conditions. At high pH conditions, ferrihydrite dissolution occurs more readily than at lower pH conditions, which releases Se(IV) back into solution. The pH dependence of retention suggests that contaminant remobilization may present serious concerns in high pH systems, such as in radioactive waste disposal environments. In such environments, radionuclides that may be immobilized on poorly-crystalline iron (hydro)oxides present in corroding steel canisters are at risk of being remobilized

into the wider environment. This remobilization behavior must therefore be taken into account when predicting the long-term behavior of radionuclides in disposal environments.

Even at high pH, a sizeable fraction of Se(IV) was still retained in the crystalline phases in a non-labile form. Spectroscopic data revealed that Se(IV) was retained in the post-transformation solids primarily as adsorbed species. This is in contrast to other elements such as U and Mo, which are able to incorporate within the structure of hematite following the transformation of a previous poorly crystalline substrate. This implies that element retention is dictated largely by structural constraints. However, despite being retained only as an adsorbed species, Se(IV) is not easily remobilized by the presence of strongly exchanging ligands, indicating that Se(IV) retention is largely stable.

The findings of this study also provide insights on the impacts of phase transformation on the mobility of contaminants such as Se(IV). The observations in this work may be used to predict how contaminants with similar properties as Se(IV) may behave across different pH conditions. This may have important implications on applications such as wastewater treatment and the remediation of contaminated soils.

3.6. List of References

Balistrieri, L., Chao, T.T. (1987) Selenium adsorption by goethite. Soil Science Society of America Journal, 51(5), 1145-1151.

Balistrieri, L., Chao, T.T. (1990) Adsorption of selenium by amorphous iron oxyhydroxide and manganese-dioxide. Geochmica et Cosmochimica Acta, 54(3), 739-751.

Bibak, A., Gerth, J., Borggaard, O.K. (1995) Retention of cobalt by pure and foreign-element associated goethites. Clays and Clay Minerals, 43(2), 141-149.

Catalano, J.G., Zhang, Z., Fenter, P., Bedzyk, M.J. (2006) Inner-sphere adsorption geometery of Se(IV) at the hematite (100)-water interface. Journal of Colloid and Interface Science, 297, 665-671.

Charlet, L., Manceau, A. (1992) X-ray absorption spectroscopic study of the sorption of Cr(III) at the oxide water interface. 2. Adsorption, coprecipitation, and surface precipitation on hydrous ferric-oxide. Journal of Colloid and Interface Science, 148, 443-470.

Cornell, R.M., Giovanoli, R. (1986) Factors that govern the formation of multi-domainic goethites. Clays and Clay Minerals, 34(5), 557-564.

Cornell, R.M., Giovanoli, R., Schindler, P.W. (1987) Effect of silica species on the transformation of ferrihydrite into goethite and hematite in alkaline media. Clays and Clay Minerals, 35(1), 21-28.

Cornell, R.M., Schwertmann, U. (2003) The Iron Oxides: Structure, Properties, Reactions, Occurrences and Uses, 2nd ed., 703 p. Wiley-VCH, Weinheim.

Crawford, R.J., Harding, I.H., Mainwaring, D.E. (1993) Adsorption and coprecipitation of single heavy metal ions onto the hydrated oxides of iron and chromium. Langmuir, 9, 3050-3056.

Cudennec, Y., and Lecerf, A. (2006) The transformation of ferrihydrite into goethite or hematite, revisited. Journal of Solid State Chemistry, 179(3), 716-722.

Das, S., Hendry, M.J., and Essilfie-Dughan, J. (2013) Adsorption of selenate onto ferrihydrite, goethite, and lepidocrocite under neutral pH conditions. Applied Geochemistry, 28, 185-193.

Deer, W.A., Howie, R.A., Zussman, J. (1962) Rock-forming Minerals, Volume 5: Non-silicates. Longmans.

Diener, A., Neumann, T. (2011) Synthesis and incorporation of selenide in pyrite and mackinawite. Radiochimica Acta, 99, 791-798.

Diener, A., Neumann, T., Kramar, U., Schild, D. (2012) Structure of selenium incorporated in pyrite and mackinawite as determined by XAFS analyses. Journal of Contaminant Hydrology, 133, 30-39.

Duc, M., Lefevre, G., Fedoroff, M. (2006) Sorption of selenite ions on hematite. Journal of Colloid and Interface Science, 298, 556-563.

Dyer, L., Fawell, P.D., Newman, O.M.G., and Richmond, W.R. (2010) Synthesis and characterisation of ferrihydrite/silica co-precipitates. Journal of Colloid and Interface Science, 348(1), 65-70.

Echigo, T., Monsegue, N., Aruguete, D.M., Murayama, M., Hochella, M.F., Jr. (2013) Nanopores in hematite (α-Fe_2O_3) nanocrystals observed by electron tomography. American Mineralogist, 98(1), 154-162.

Eklund, L. Persson, I. (2014) Structure and hydrogen bonding of the hydrated selenite and selenate ions in aqueous solution. Dalton Transactions, 43(17), 6315-6321.

Erbs, J.J., Berquo, T.S., Reinsch, B.C., Lowry, G.V., Banerjee, S.K., and Penn, R.L. (2010) Reductive dissolution of arsenic-bearing ferrihydrite. Geochimica Et Cosmochimica Acta, 74(12), 3382-3395.

Ford, R.G., Bertsch, P.M. (1999) Distinguishing between surface and bulk dehydration-dehydroxylation reactions in synthetic goethites by high-resolution thermogravimetric analysis. Clays and Clay Minerals, 47(3), 329-337.

Francisco, P.C.M., Sato, T., Otake, T., Kasama, T. (2016) Kinetics of Fe(III) mineral crystallization in the presence of Si at alkaline conditions. American Mineralogist, in press, DOI:http://dx.doi.org/10.2138/am-2016-5589.

Giester, G., Pertlik, F. (1994) Synthesis and crystal structure of iron(III) selenate(IV) trihydrate, $Fe_2(SeO_3)_3$ $3H_2O$. Journal of Alloys and Compounds, 210, 125-128.

Hayes, K.F., Roe, A.L., Brown, G.E. Jr., Hodgson K.O., Leckie, J.O., Parks G.A. (1987) In situ x-ray absorption study of surface complexes: Selenium oxyanions on α-FeOOH. Science, 238(4828), 783-786.

Hazan, E., Sadia, Y., and Gelbstein, Y. (2013) Characterization of AISI 4340 corrosion products using Raman spectroscopy. Corrosion Science, 74, 414-418.

Jordan, N., Lomenech, C., Marmier, N., Giffaut, E., Eherhardt, J-J. (2009) Sorption of selenium(IV) onto magnetite in the presence of silicic acid. Journal of Colloid and Interface Science, 329, 17-23.

Jordan, N., Ritter, A., Schenoist, A.C., Weiss, S., Schild, D., Hubner, R. (2014) Selenium(IV) uptake by maghemite (γ-Fe_2O_3). Environmental Science and Technology, 48, 1665-1674.

Kelly, S.D., Lu, P., Bolin, T., Chattopahyay, S., Newville, M.G., Shibata, T., Zhu, C. (2008). Molecular structure of Lead(III) coprecipitated with Iron(III) oxyhydroxide. In *Adsorption of Metals by Geomedia II* (eds. M. Barnett and D. Kent). Developments in Earth & Environmental Sciences 7, Elsevier, 67-94.

Kim, C.S., Rytuba, J.J., Brown, G.E., Jr. (2004) EXAFS study of mercury(II) sorption to Fe- and Al-(hydr)oxides: I. Effects of pH. Journal of Colloid and Interface Science, 271, 1-15.

Kwon, S.K., Shinoda, K., Suzuki, S., and Waseda, Y. (2007) Influence of silicon on local structure and morphology of gamma-FeOOH and alpha-FeOOH particles. Corrosion Science, 49(3), 1513-1526.

Lu, P., Nuhfer, N.T., Kelly, S., Li, Q., Konishi, H., Elswick, E., Zhu, C. (2011). Geochimica et Cosmochimica Acta, 75, 4547-4561.

Manceau, A., Charlet, L. (1994) The mechanism of selenate adsorption on goethite and hydrous ferric oxide. Journal of Colloid and Interface Science, 168, 87-93.

Marshall, T.A., Morris, K., Law, G.T.W., Livens, F.R., Mosselmans, J.F.W., Bots, P., and Shaw, S. (2014) Incorporation of uranium into hematite during crystallization from ferrihydrite. Environmental Science & Technology, 48(7), 3724-3731.

Merrill, D.T., Manzione, M.A., Parker, D.S., Petersen, J.J., Chow, W., Hobbs, A.O. (1987) Field evaluation of arsenic and selenium removal by iron coprecipitation. Environmental Progress, 6(2), 82-90.

Missana, T., Alonso, U., Schenoist, A.C., Granizo, N., Garcia-Gutierrez, M. (2009) Selenite retention by nanocrystalline magnetite: Role of adsorption, reduction and dissolution/co-precipitation processes. Geochimica et Cosmochimica Acta, 73, 6205-6217.

Refait, P., Benali, O., Abdelmoula, M., and Genin, J.M.R. (2003) Formation of 'ferric green rust' and/or ferrihydrite by fast oxidation of iron(II-III) hydroxychloride green rust. Corrosion Science, 45(11), 2435-2449.

Rovira, M., Gimenez, J., Martinez, M., Martinez-Llado, X., de Pablo, J., Marti, V., and Duro, L. (2008) Sorption of selenium(IV) and selenium(VI) onto natural iron oxides: Goethite and hematite. Journal of Hazardous Materials, 150(2), 279-284.

Stipp, S., Hansen, M., Kristensen, R., Hochella, M.F., Jr., Bennedsen, L., Dideriksen, K., Balic-Zunic, T., Leonard, D., Mathieu, H.-J. (2002) Behaviour of Fe-oxides relevant to contaminant uptake in the environment. Chemical Geology, 190, 321-337.

Schulze, D.G., Schwertmann, U. (1984) The influence of aluminium on iron oxides: X. Properties of Al-substituted goethites. Clay Minerals, 19, 521-539.

Sileo, E.E., Solis, P.S., Paiva-Santos, C.O. (2003) Structural study of a series of synthetic goethites obtained in aqueous solutions containing cadmium(II) ions. Powder Diffraction, 18, 50-55.

Su, C., Suarez, D.L. (2000) Selenate and selenite sorption on iron oxides: An infrared and electrophoretic study. Soil Science Society of America Journal, 64, 101-111

Tamari, Y. (1998) Methods of analysis for the determination of selenium in biological, geological, and water samples. In *Environmental Chemistry of Selenium* (eds. W.T. Frankenberger, Jr. and R.A. Engberg). Dekker, 27-46.

Taylor, J.C., and Clapp, R.A. (1992) New features and advanced applications of Siroquant: A personal computer XRD full profile quantitative analysis software package. Advances in X-ray Analysis, 35, 49-55.

van Veelen, A., Preedy, O., Qi, J., Law, G.T.W., Morris, K., Mosselmans, J.F.W., Ryan, M.P., Evans, N.D.M., Wogelius, R.A. (2014) Uranium and technetium interactions with wustite [$Fe_{1-x}O$] and portlandite [$Ca(OH)_2$] surfaces under geological disposal facility conditions. Mineralogical Magazine, 78(5), 1097-1113.

Vu, H.P., Shaw, S., Brinza, L., Benning, L.G. (2013) Partitioning of Pb(II) during goethite and hematite crystallization: Implications for Pb transport in natural systems. Applied Geochemistry, 39, 119-128.

Waychunas, G.A., Fuller, C.C., Davis, J.A. (2002) Surface complexation and precipitation geometry for aqueous Zn(II) sorption on ferrihydrite I: X-ray absorption extended fine structure spectroscopy analysis. Geochimica et Cosmochimica Acta, 66, 1119-1137.

Wickleder, M.S. (2002) Sodium selenite, Na_2SeO_3. Acta Crystallographica Section E, E58, i103-i104.

Xiao, D., Hou, Y., Wang, E., An, H., Lu, J., Li, Y., Xu., L., Hu, C. (2004) Hydrothermal synthesis and crystal structure of a three-dimensional metal selenite containing double helical chains: $Fe_3(H_2O)(SeO_3)_3$. Journal of Solid State Chemistry, 177, 2699-2704.

Yokoyama, T., Makishima, A., Nakamura, E. (1999) Evaluation of the coprecipitation of incompatible trace elements with fluoride during silicate rock dissolution by acid digestion. Chemical Geology, 157, 175-187.

Zhang, P., Sparks, D.L. (1990) Kinetics of selenate and selenite adsorption/desorption at the goethite/water interface. Environmental Science and Technology, 24, 1848-1856.

Zhang, S.-Y., Hu, C.L., Li, P.-X., Jiang, H.-L., Mao, J.-G. (2012) Syntheses, crystal structures and properties of new lead(II) or bismuth(III) selenites and tellurite. Dalton Transactions, 41, 9532-9542.

Table 1. Fitting parameters for the Se K-edge EXAFS spectra. CN: coordination number; R: inter-atomic distance; σ^2: disorder parameter

Sample	Path	CN	R (Å)	σ^2 (Å^2)
pH 5	Se-O	2.6±0.1	1.70±0.01	0.001±0.0004
Fresh	Se-Fe	1.4±0.4	3.25±0.05	0.006±0.002
pH 5	Se-O	2.3±0.1	1.72±0.01	0.001±0.0004
Trans	Se-Fe	2.1±0.4	3.29±0.05	0.008±0.002
pH 10	Se-O	2.8±0.1	1.68±0.01	0.001±0.0004
Fresh	Se-Fe	0.9±0.4	3.32±0.05	0.005±0.002
pH 10	Se-O	2.8±0.1	1.68±0.01	0.001±0.0004
Trans	Se-Fe	2.6±0.4	3.37±0.05	0.008±0.002

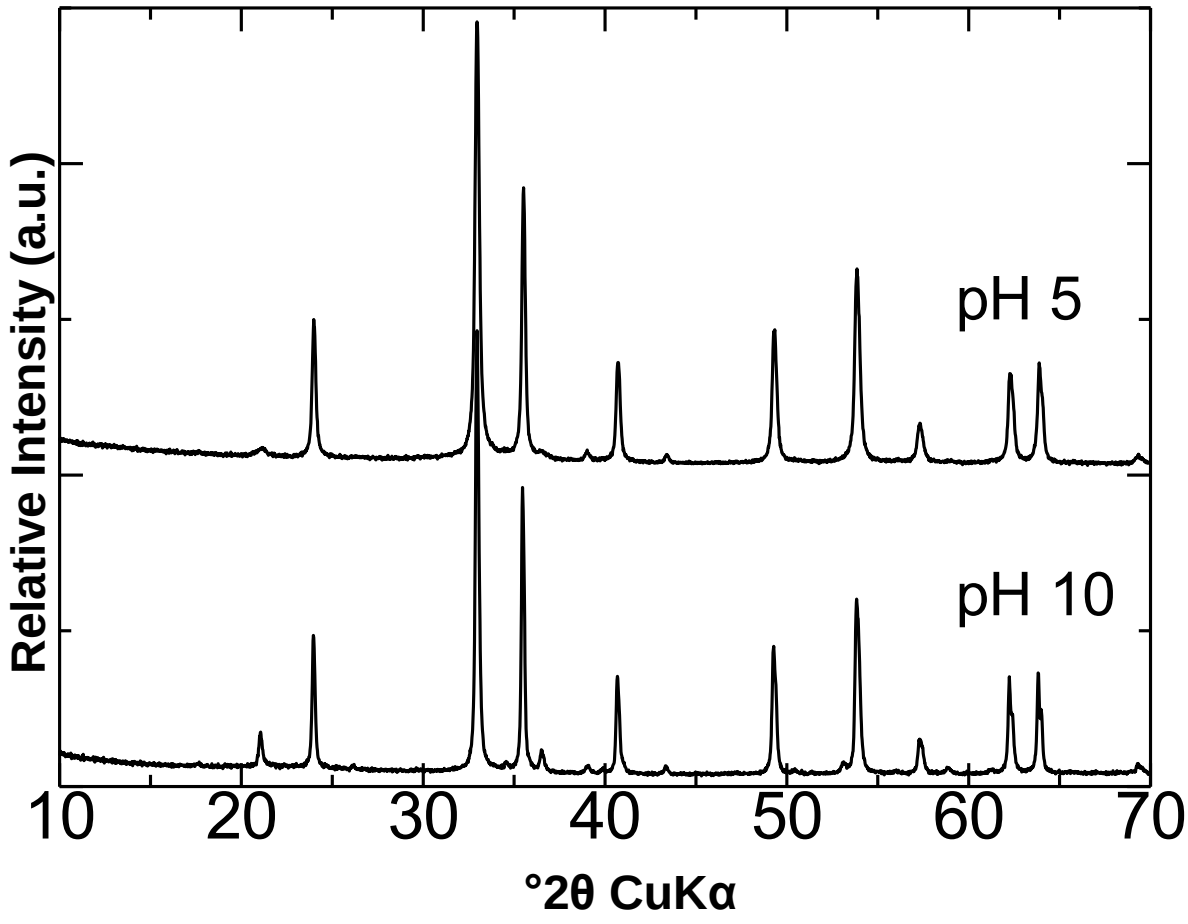

Fig. 1. XRD profiles of the final transformation products at pH 5 and pH 10. The arrow marks the position the peak corresponding to goethite.

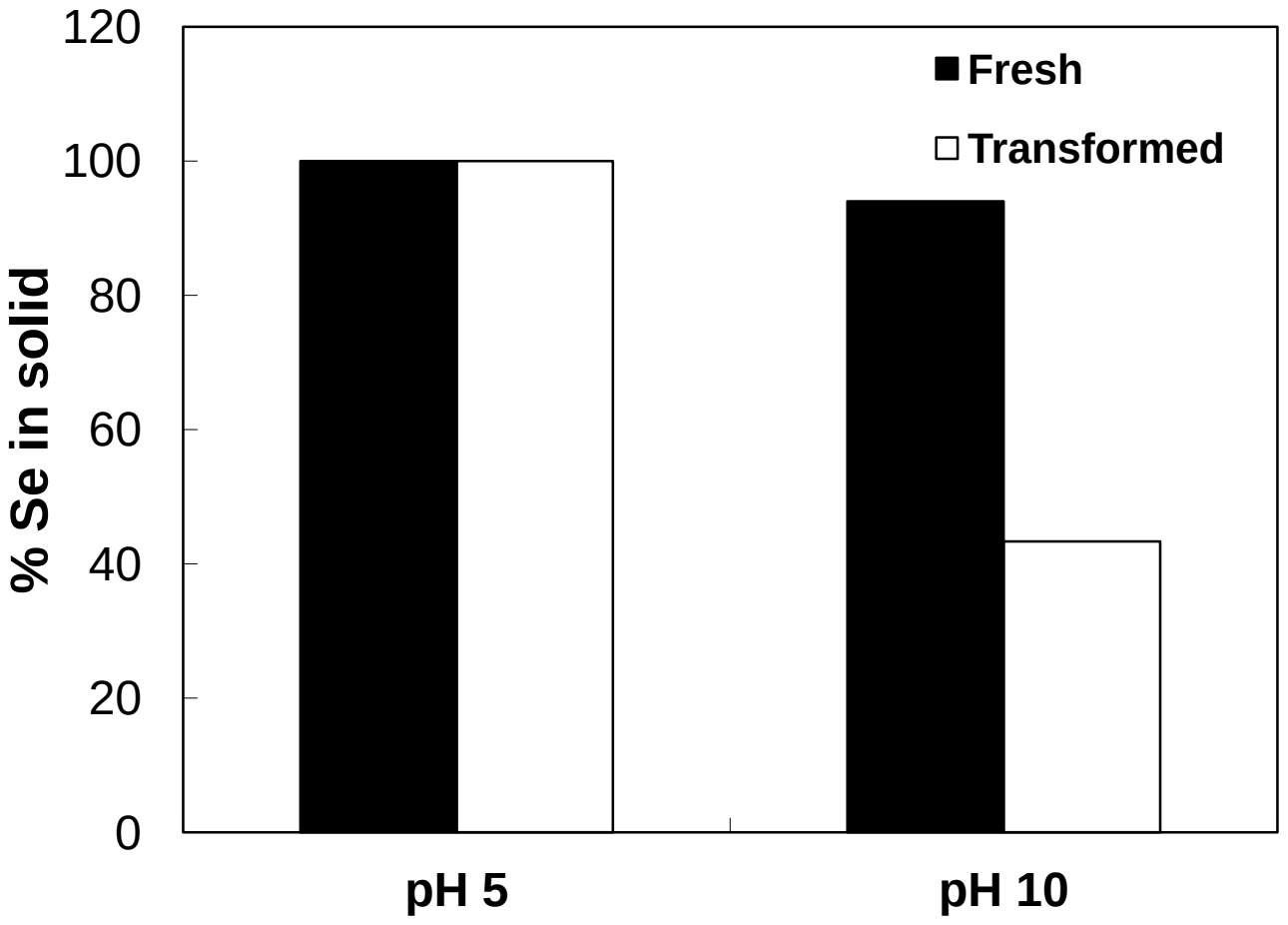

Fig. 2. Proportion of Se(IV) taken up co-precipitation (black bar) and retained after transformation (white bar). The degree of retention at pH 10 is significantly lower compared to pH 5.

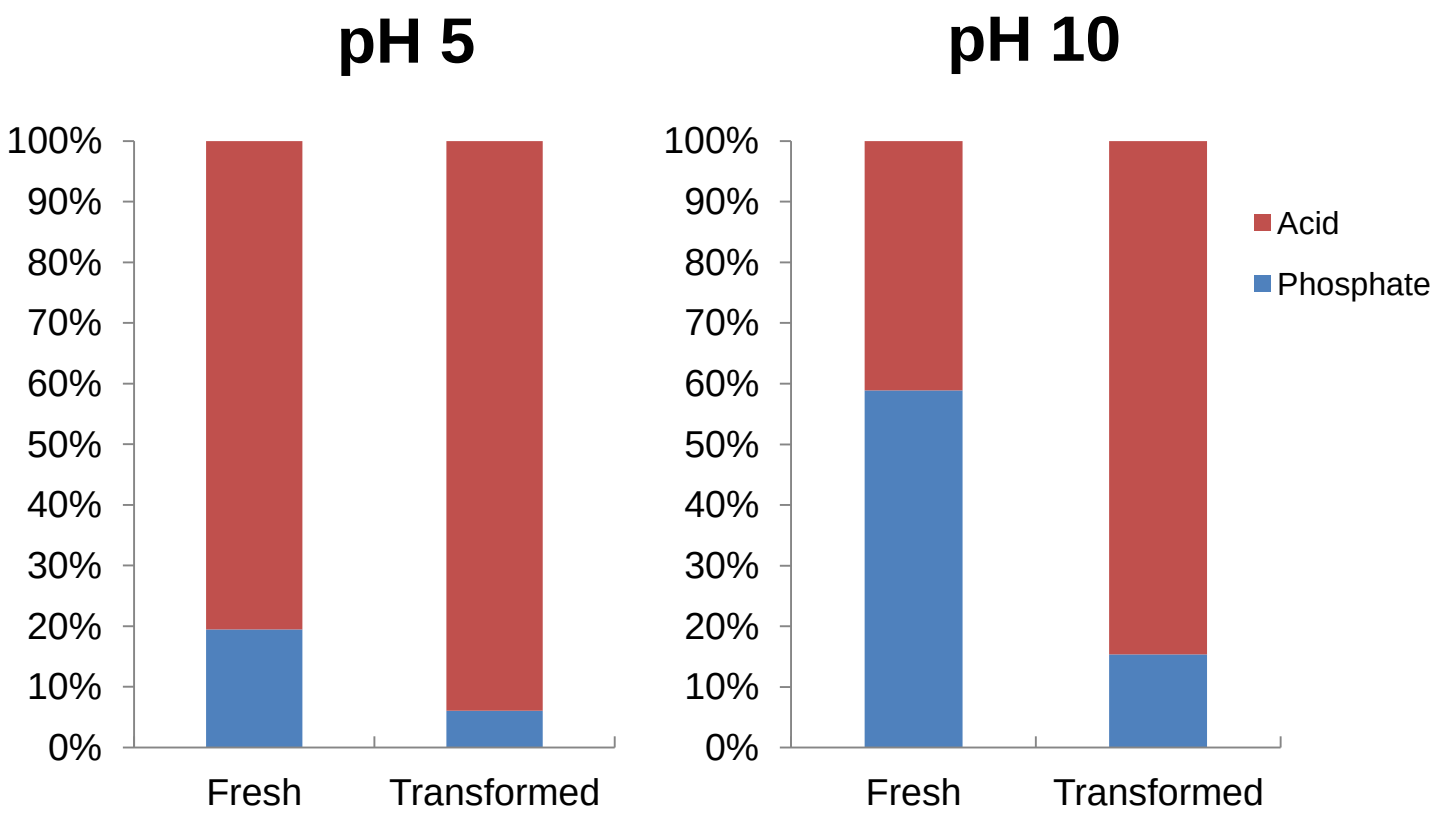

Fig. 3. Partitioning of Se(IV) in the freshly co-precipitated and post-transformation products. Se(IV) is present as both phosphate-extractable and acid-digestible species. The proportion of phosphate-extractable species decreases following transformation, with the majority of Se(IV) only being extractable by complete acid digestion.

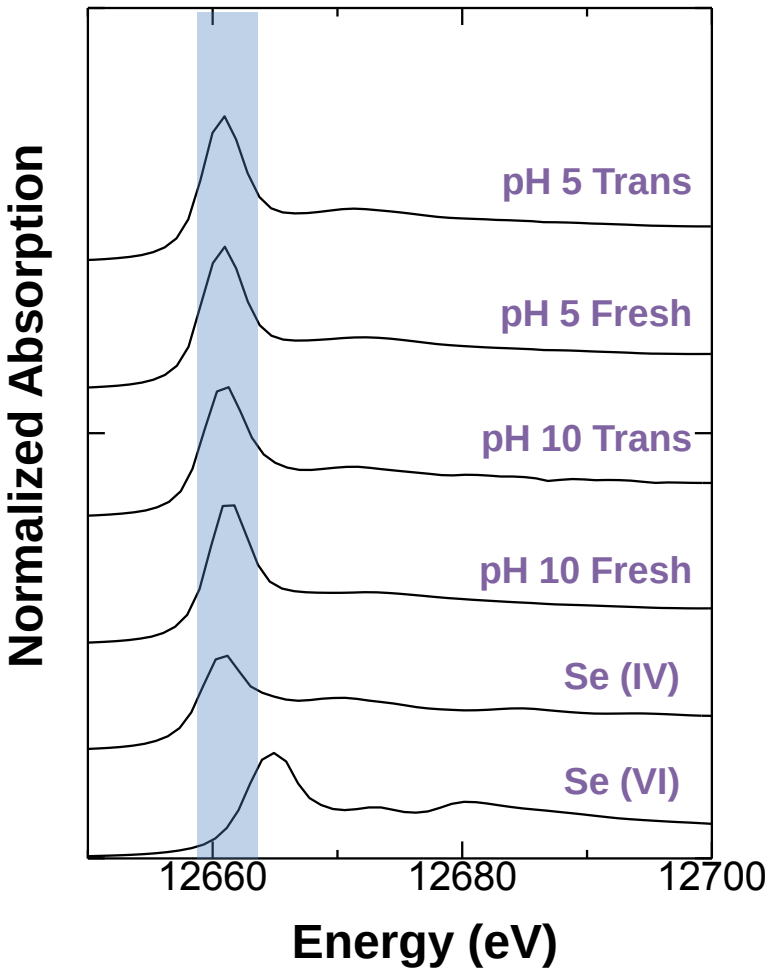

Fig. 4. Se K-edge XANES spectra of solid products from the 250 ppm starting Se(IV) samples, compared with Se(IV) and Se(VI) standards. Following transformation, a post-edge feature appears and becomes more prominent, indicating a change in the local environment of Se(IV).

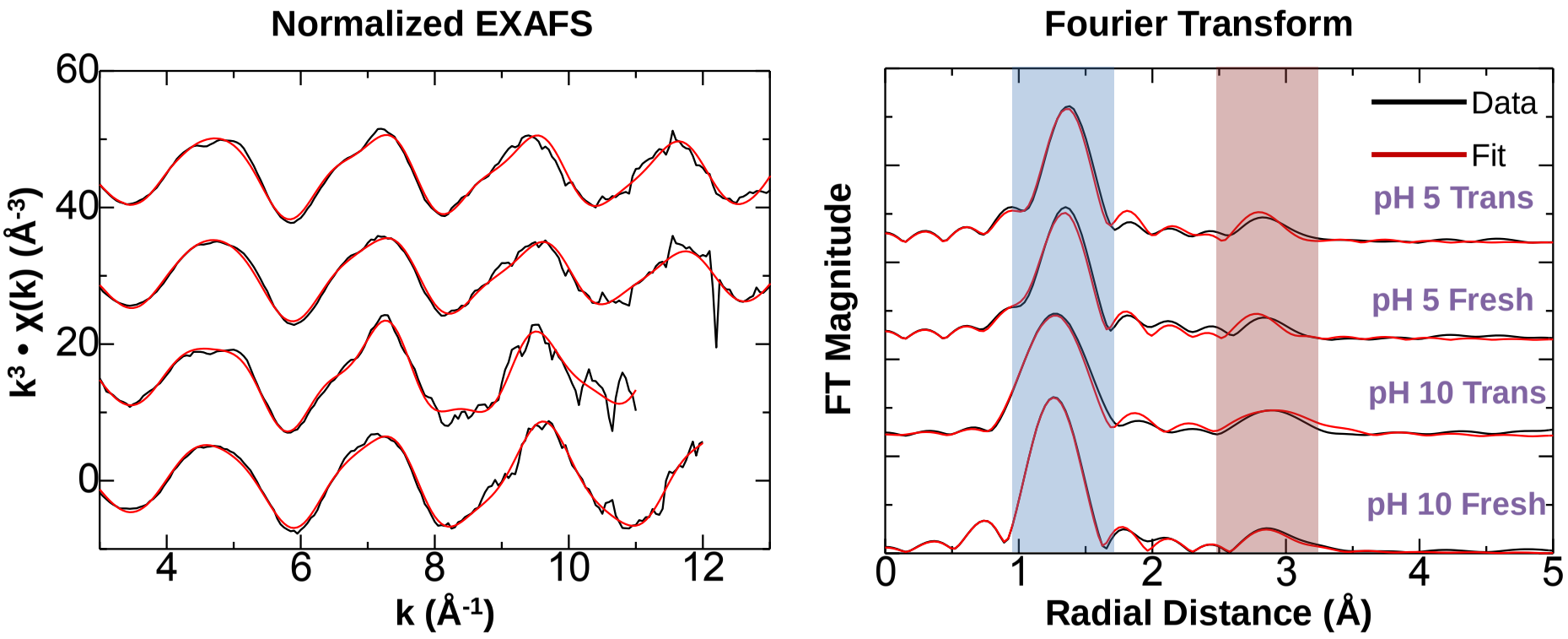

Fig. 5. Se K-edge EXAFS spectra (A) of solid products from the 250 ppm starting Se(IV) samples and the corresponding Fourier Transforms (B). The Fourier Transforms exhibit a strong first-shell contribution corresponding to Se-O backscattering and a weaker second-shell contribution corresponding to Se-Fe backscattering.

Supplementary Information Table 1. Relative proportion and lattice parameters of crystalline phases in the post-transformation solids as determined from Rietveld refinement.

pH	Goethite				Hematite		
	Percentage	Lattice Parameters (Å)			Percentage	Lattice Parameters (Å)	
		a	*b*	*c*		*a*	*c*
5	-	-	-	-	100	5.03	13.78
10	9.6	9.97	3.02	4.61	90.4	5.03	13.78
Published [a]	-	9.94 [b]	3.02 [b]	4.59 [b]	-	5.03	13.75

[a] Deer et al., 1961

[b] Published values in *Pbnm* space group. Goethite XRD data in this study were indexed using *Pnma* space group, which resulted in the following inversions: *a* → *c*, *b* → *a*, *c* → *b* (Cornell and Schwertmann, 2003)

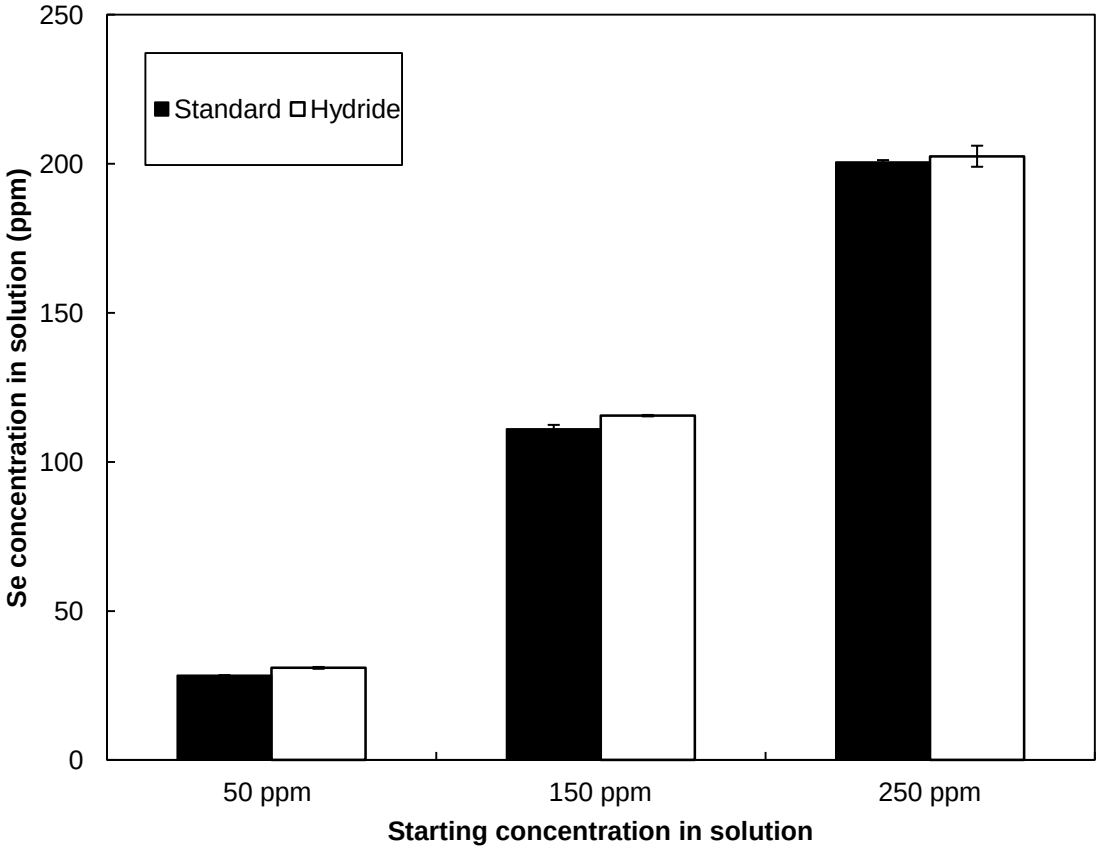

Supplementary Fig S1. Comparison between results of standard and hydride generation ICP-AES measurements. Similarity in results indicate that Se is present in Se(IV) oxidation state.

CHAPTER 4: Effects of Si on the behavior of Se(IV) during Fe(III) mineral transformation at alkaline conditions

Part of this chapter is in preparation for submission to *Environmental Science: Processes and Impacts* as:

P.C.M. Francisco, T. Sato, T. Otake (2016). Effects of Si on the behavior of co-precipitated Se(IV) during ferrihydrite transformation at alkaline conditions

4.1. Introduction

^{79}Se is one of the radionuclides that may be released from vitrified high-level radioactive wastes. Due to its long half-life, its immobilization is of great importance. In repository conditions, Se exists as mobile Se(IV) oxyanions. Its immobilization on poorly crystalline, metastable phases such as hydrous Fe(III) oxides as well as on stable, crystalline Fe(III) phases such as goethite, hematite, maghemite (e.g. Balistrieri and Chao, 1987, 1990; Zhang and Sparks, 1990; Su and Suarez, 2000; Rovira et al., 2006; Duc et al., 2006; Jordan et al., 2009; Jordan et al., 2014) has been investigated. As shown highlighted in Chapter 3, the long-term mobility of hazardous oxyanions is also controlled by the transformation of sorption substrates, which, in turn, is also affected by the presence of foreign anions or impurities. One of the most common impurities is Si. In natural environments, Si originates from the weathering of silicate rocks and is present in significant amounts in soils. Furthermore, in engineered environments such as in geologic disposal systems for radioactive wastes, Si may originate from the vitrified waste component as well as the surrounding host rock. As demonstrated in Chapter 2, Si alters the transformation rates and products of iron (hydro)oxides. Given these effects of Si on transformation behavior, it can be hypothesized that Si may also exert significant influence on the behavior of Se(IV) during ferrihydrite transformation to crystalline phases possibly by delaying the remobilization of Se(IV) during transformation. Furthermore, since Si modifies the surface properties of iron (hydro)oxides as well as the availability of surface adsorption sites, Si may also likely affect the degree of retention of Se(IV) in the solid products after transformation.

Thus, the objectives of this chapter is to investigate how Se(IV) will behave during ferrihydrite transformation. In particular, this chapter investigates the release kinetics of Se(IV) during transformation as well as the degree of retention of Se(IV) in the crystalline phases following transformation.

4.2. Methods

4.2.1. Synthesis of Fe-Se-Si co-precipitates

The synthesis of Fe-Si-Se precipitates was carried out following the same procedures outlined in Chapters 2 and 3.

4.2.2. Sample Characterization

Se concentrations in solution after separation from the solids were determined by inductively coupled plasma atomic emission spectroscopy using a Shimadzu ICPE-9000 ICP-AES. The amount of Se taken up or retained by the solids was determined from the difference between the initial concentration of the precipitating liquid and the concentrations after co-precipitation / crystallization.

Solid samples both before and after transformation were characterized by powder X-ray diffraction using a Rigaku RINT2000 X-ray diffractometer, which operates at 40 kV and 40 mA and is equipped with a Cu target and graphite monochromator. Rietveld refinement using the commercial SIROQUANT software (Taylor and Clapp, 1992) was performed for the post-transformation samples to estimate the proportion of crystalline products. XRD patterns were indexed according to the *Pnma* and $R\bar{3}c$ space groups for goethite and hematite, respectively.

Refinement parameters include instrument zero, asymmetry factors, half-width and unit cell parameters and preferred orientation (Francisco et al., 2016).

To determine the partitioning of Se in the solid products both before and after crystallization, a series of chemical extraction experiments were conducted. The surface-bound fraction was extracted by finely disaggregating and dispersing the solids in 1.0 M Na_2HPO_4 (Kanto, 99%; pH ~9) for 12 hours. Due to the strong affinity of PO_4^{3-} anions to Fe-(hydro)oxide surfaces, PO_4^{3-} can easily exchange with surface-bound Se species. To ensure homogeneity, the suspensions were continuously agitated using a rotary mixer. The extracting solution was separated from the solids by centrifugal separation, filtered through 0.20 μm PTFE membrane filters and acidified for ICP-AES analysis. The remaining solids were washed with deionized water, freeze-dried then completely dissolved in 6.0 M HCl at 110°C using a heating block, with the acid being allowed to evaporate (Yokoyama et al., 1999). This dissolution procedure was repeated 3 to 4 times until all of the solids have been dissolved. The residues resulting from the evaporation of the acid were then re-dissolved in 4.0 M HNO_3 for analysis by ICP-AES.

4.3. Results

4.3.1. Solution Analyses

Analysis of solutions separated from the solids immediately after co-precipitation shows almost complete removal of Se(IV), with more than 90% of the starting Se being sequestered from solution. With increasing Si, the uptake of Se decreases slightly. For example, ~94% of Se was removed from solution, while only ~91% was removed if 1.25 x 10^{-3} M Si was present (Fig. 1). During transformation at 80°C, Se was released back into solution as indicated by the increase in the concentration of Se in the supernatants (Fig. 2). The rate of release is affected by the presence of Si. In the absence of Si, the concentration of Se increased rapidly, with the maximum concentration

being attained after 3 hours. In contrast, Se was released gradually in the presence of 1.25 x 10^{-3} M Si, with the maximum concentration being reached after about 18 hours. Furthermore, the maximum concentration of Se released increases with increasing Si. If no Si is present, the maximum concentration of Se in the solution is ~25 ppm. This increases to ~36 ppm in the presence of 1.25 x 10^{-3} M Si.

In all cases, the concentration of Se in the solution is always less than the starting concentration of 50 ppm, which indicates that some of the Se was retained in the solid phase. The retained fraction of Se was calculated based on the difference in the starting concentration and the concentration of released Se. With increasing Si, the retained fraction decreases from ~51 % in the absence of Si to ~27 % in the presence of 1.25 x 10^{-3} M Si (Fig. 1).

4.3.2. Solid Characterization

XRD characterization of the post-transformation solids shows that the resulting phase assemblage consists of a mixture of goethite and hematite (Fig. 3), similar to the results described in Chapters 2 and 3. Furthermore, the relative proportions of hematite increases with increasing Si, similar to the results reported in Chapter 2, although the percentage of goethite is higher compared to samples aged at similar times in the absence of Se described in Chapter 2. This is consistent with the findings reported in Chapter 3 that shows Se favors the crystallization of goethite.

4.3.3. Partitioning of Se(IV) in the Crystalline Phases

Results of the chemical extraction experiments show that Se is present both as phosphate-extractable and acid-extractable species (Fig. 4), consistent with the results presented in Chapter 3. While phosphate-extractable Se constitute only a small proportion of Se retained in the solid, a significant proportion can only be extracted by the total dissolution in acid. In the absence of Si,

there are approximately 0.26 mg/g and 3.59 mg/g of phosphate-extractable and acid-extractable Se, respectively. In the presence of 1.25 x 10^{-3} M Si, both species decrease to 0.18 mg/g and 1.14 mg/g, respectively.

4.4. Discussion

4.4.1. Delay in the Release of Se(IV)

As shown in the previous chapters, the transformation pathway of ferrihydrite to crystalline phases at pH 10 involves both dissolution / re-precipitation as well as solid-state rearrangement. The release of Se is associated with the dissolution pathway of the ferrihydrite. It can thus be inferred that the release of Se back into solution would be retarded if the dissolution of ferrihydrite were retarded. As shown in Chapter 2, this delay in the transformation is due to the inhibition effect of Si against ferrihydrite transformation. It is generally accepted that Si is present mainly as surface complexes on ferrihydrite (Seehra et al., 2004; Dyer et al., 2010; 2012). Inner-sphere Si complexes on ferrihydrite surfaces (Swedlund et al., 2009) passivates the surface against dissolution, which makes the ferrihydrite resistant to transformation. With the dissolution pathway being inhibited by the presence of Si, the release of Se during ferrihydrite transformation is then delayed.

4.4.2. Decreased Retention of Se(IV)

The retention of Se is strongly controlled by the presence of Si. To understand the effects of Si on the retention of Se(IV), it is necessary to understand its effects on both phosphate-extractable and acid-extractable forms of Se in crystalline phases. The phosphate-extractable fraction represents surface-bound species that is readily accessible to phosphate exchange. Thus, this fraction accounts for Se present as adsorbed surface complexes on goethite and hematite. Si is known to strongly

adsorb on the surfaces of iron (hydro)oxides, strongly competing for sorption sites with other oxyanions such as arsenate (Swedlund and Webster, 1999) and molybdate (Xu et al., 2006), to name a few. It has also been shown at neutral conditions (pH ~ 7) that Si strongly competes with Se(IV) for sorption sites in goethite and amorphous hydrous ferric oxides (Balistrieri and Chao, 1987).

The formation of Si surface complexes on iron (hydro)oxides may be described by the following surface complexation reactions:

$>FeOH + H_4SiO_4 \rightarrow >FeH_3SiO_4 + H_2O$ log K = 4.18

$> FeOH + H_4SiO_4 \rightarrow FeH2SiO_4^- + H^+ + H_2O$ log K = -4.32

The formation of Se surface complexes may be described by the following:

$>FeOH + H^+ + SeO_3^{2-} \rightarrow >FeSeO_3^- + H_2O$ log K = 15.25

$> FeOH + 2H^+ + SeO_3^{2-} \rightarrow >FeHSeO_3 + H_2O$ log K = 21.07

Based on the values of the log K for each surface species, the formation of Si complexes is significantly favored over the formation of Se complexes (Jordan et al., 2009). Thus, in the presence of both Si and Se in solution, it is reasonable to expect that Si surface species with iron (hydro)oxides will be more dominant.

To further check the competition between Si and Se for adsorption sites on goethite and hematite surfaces, a simple surface complexation model was constructed using REACT (part of the Geochemists' Workbench 10.0 program suite) based on the modified double-layer model and surface site density data of Dzombak and Morel (1990). Thermodynamic data for the surface species mentioned above were added to the FeOH+.sdat database. The results of the modeling (Fig. 5) show that in the absence of Si, up to ~10 - 19 % of the Se is adsorbed on the surface of goethite and hematite. In the presence of Si, the percentage of adsorbed Se drastically drops to ~2 - 3 %. The percentage of adsorbed Si, on the other hand, is significantly larger compared to Se, indicating that much of the available surface sites are occupied by Si. Based on the results of surface complexation modeling, the decrease in the phosphate-extractable Se in the crystalline phases may thus be

explained by the competition between Si and Se for surface sites. For both Si and Se, the adsorbed fractions are consistently smaller for goethite than for hematite, possibly due to the lower surface site density for goethite. This indicates that goethite may play a less significant role in the retention of Se by surface adsorption compared to hematite, consistent with earlier experimental studies (Rovira et al., 2006).

The acid-extractable Se species may represent Se that was either structurally incorporated into the crystalline phases or Se trapped within growing crystal aggregates. Given the uncertainty about the occupancy of this fraction of Se in the crystalline phases, the effect of Si may thus be interpreted in two ways. First, assuming that Se is structurally incorporated into the crystalline phases, such as in hematite (hematite is considered due to it being the dominant crystalline phase, as well as the phase most likely to incorporate Se because of its transformation pathway involving aggregation and solid-state rearrangement), the decreased retention of Se due to the presence of Si may also be understood to be due to competition for structural sites. The structure of hematite is characterized of Fe(III) octahedral following hexagonal closest packing (hcp) arrangement (Cornell and Schwertmann, 2003). In such an arrangement, vacant, interstitial tetrahedral sites that can accommodate Si are present. Occupancy of Si in such sites is expected to cause expansion of the lattice along the *c* direction (Asenath-Smith et al., 2015). As shown in Chapter 2, the *c* lattice parameter of hematite increases with increasing Si, indicating that Si is incorporated in interstitial tetrahedral sites in hematite. EXAFS results presented in Chapter 3 indicate that Se retains its trigonal pyramid configuration in the transformation products. This clearly indicates that Se is not in an octahedral site, although it is possible that it may also occupy vacant interstitial sites similar to Si. If Se is also in a tetrahedral site, then it may compete with Si for such sites, with the smaller Si^{4+} ion (0.26 Å) being favored over the bigger Se^{4+} ion (0.50 Å). Alternatively, assuming that the acid-extractable Se represents adsorbed Se that were trapped within aggregates of growing crystals, the decreased retention of Se with increasing Si may likewise be explained by competition for surface sites between Si and Se.

4.5. Conclusions

The presence of Si in iron (hydro)oxides has been shown to significantly affect the behavior of Se(IV) during ferrihydrite transformation to crystalline phases. Si has two principal effects on the behavior of Se(IV). Due to the inhibitory effect of Si on the transformation of ferrihydrite, the remobilization of Se(IV) is delayed with increasing Si. Furthermore, Si competes with Se for sorption and, possibly, structural sites, resulting in the decreased retention of Se(IV).

List of References

Asenath-Shmit, E., Hovden, R., Kourkoutis, L.F., Estroff, L.A. (2015) Hierarchichally structured hematite architerctures achieved by growth in a silica hydrogel. Journal of the American Chemical Society, 137, 5184-5192.

Balistrieri, L., Chao, T.T. (1987) Selenium adsorption by goethite. Soil Science Society of America Journal, 51(5), 1145-1151.

Balistrieri, L., Chao, T.T. (1990) Adsorption of selenium by amorphous iron oxyhydroxide and manganese-dioxide. Geochmica et Cosmochimica Acta, 54(3), 739-751.

Cornell, R.M., Schwertmann, U. (2003) The Iron Oxides: Structure, Properties, Reactions, Occurrences and Uses, 2nd ed., 703 p. Wiley-VCH, Weinheim.

Dyer, L., Fawell, P.D., Newman, O.M.G., and Richmond, W.R. (2010) Synthesis and characterisation of ferrihydrite/silica co-precipitates. Journal of Colloid and Interface Science, 348(1), 65-70.

Dyer, L., Chapman, K.W., English, P., Saunders, M., Richmond, W.R. (2012) Insights into the crystal and aggregate structure of Fe^{3+} oxide/silica co-precipitates. American Mineralogist, 97, 63-69.

Dzombak, D.A., Morel, F.M.M., 1990. Surface complexation modeling: hydrous ferric oxide. John

Wiley & Sons, New York, p. 393.

Francisco, P.C.M., Sato, T., Otake, T., Kasama, T. (2016) Kinetics of Fe(III) mineral crystallization in the presence of Si at alkaline conditions. American Mineralogist, in press, DOI:http://dx.doi.org/10.2138/am-2016-5589.

Jordan, N., Lomenech, C., Marmier, N., Giffaut, E., Eherhardt, J-J. (2009) Sorption of selenium(IV) onto magnetite in the presence of silicic acid. Journal of Colloid and Interface Science, 329, 17-23.

Jordan, N., Marmier, N., Lomenech, C., Giffaut, E., Eherhardt, J-J. (2009) Competition between selenium (IV) and silicic acid on the hematite surface. Chemosphere, 75, 129-134.

Jordan, N., Ritter, A., Schenoist, A.C., Weiss, S., Schild, D., Hubner, R. (2014) Selenium(IV) uptake by maghemite (γ-Fe_2O_3). Environmental Science and Technology, 48, 1665-1674.

Rovira, M., Gimenez, J., Martinez, M., Martinez-Llado, X., de Pablo, J., Marti, V., and Duro, L. (2008) Sorption of selenium(IV) and selenium(VI) onto natural iron oxides: Goethite and hematite. Journal of Hazardous Materials, 150(2), 279-284.

Seehra, M.S., Roy, P., Raman, A., and Manivannan, A. (2004) Structural investigations of synthetic ferrihydrite nanoparticles doped with Si. Solid State Communications, 130(9), 597-601.

Su, C., Suarez, D.L. (2000) Selenate and selenite sorption on iron oxides: An infrared and electrophoretic study. Soil Science Society of America Journal, 64, 101-111.

Swedlund, P.J., Webster, J.G. (1999) Adsorption and polymerisation of silicic acid on ferrihydrite, and its effect on arsenic adsorption. Water Research, 33(6), 3413-3422.

Swedlund, P.J., Miskelly, G.M., and McQuillan, A.J. (2009) An attenuated total reflectance IR study of silicic acid adsorbed onto a ferric oxyhydroxide surface. Geochimica Et Cosmochimica Acta, 73(14), 4199-4214.

Taylor, J.C., and Clapp, R.A. (1992) New features and advanced applications of Siroquant: A personal computer XRD full profile quantitative analysis software package. Advances in X-ray Analysis, 35, 49-55.

Xu, N., Christodoulatos, C., Braida, W. (2006) Adsorption of molybdate and tetrathiomolybdate onto pyrite and goethite: Effect of pH and competitite anions. Chemosphere, 62(10), 1726-1735.

Yokoyama, T., Makishima, A., Nakamura, E. (1999) Evaluation of the coprecipitation of incompatible trace elements with fluoride during silicate rock dissolution by acid digestion. Chemical Geology, 157, 175-187.

Zhang, P., Sparks, D.L. (1990) Kinetics of selenate and selenite adsorption/desorption at the goethite/water interface. Environmental Science and Technology, 24, 1848-1856.

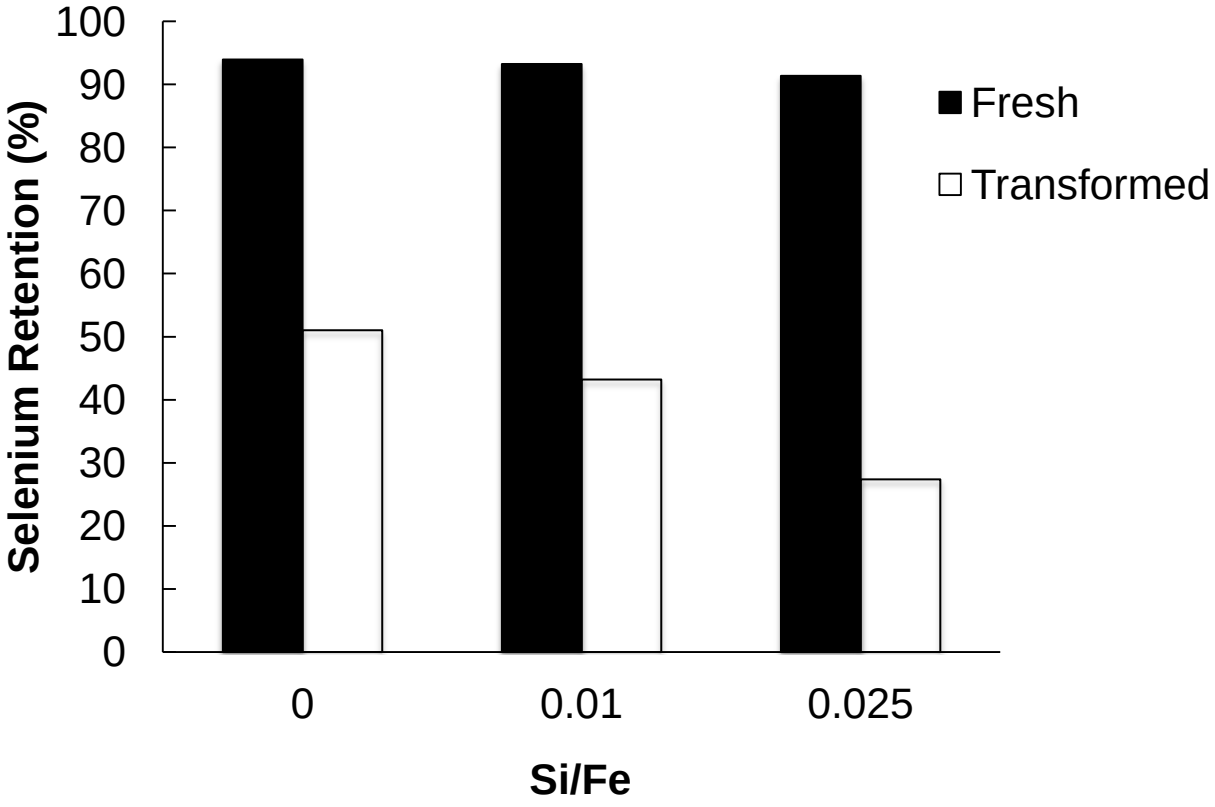

Fig. 1. Percentage of Se(IV) taken up by co-precipitation (black bar) and the percentage of Se(IV) retained after transformation (white bar) as a function of Si/Fe of precipitating solution. Transformation of ferrihydrite to crystalline phases results in the retention of only a fraction of Se(IV), which decreases with increasing Si/Fe.

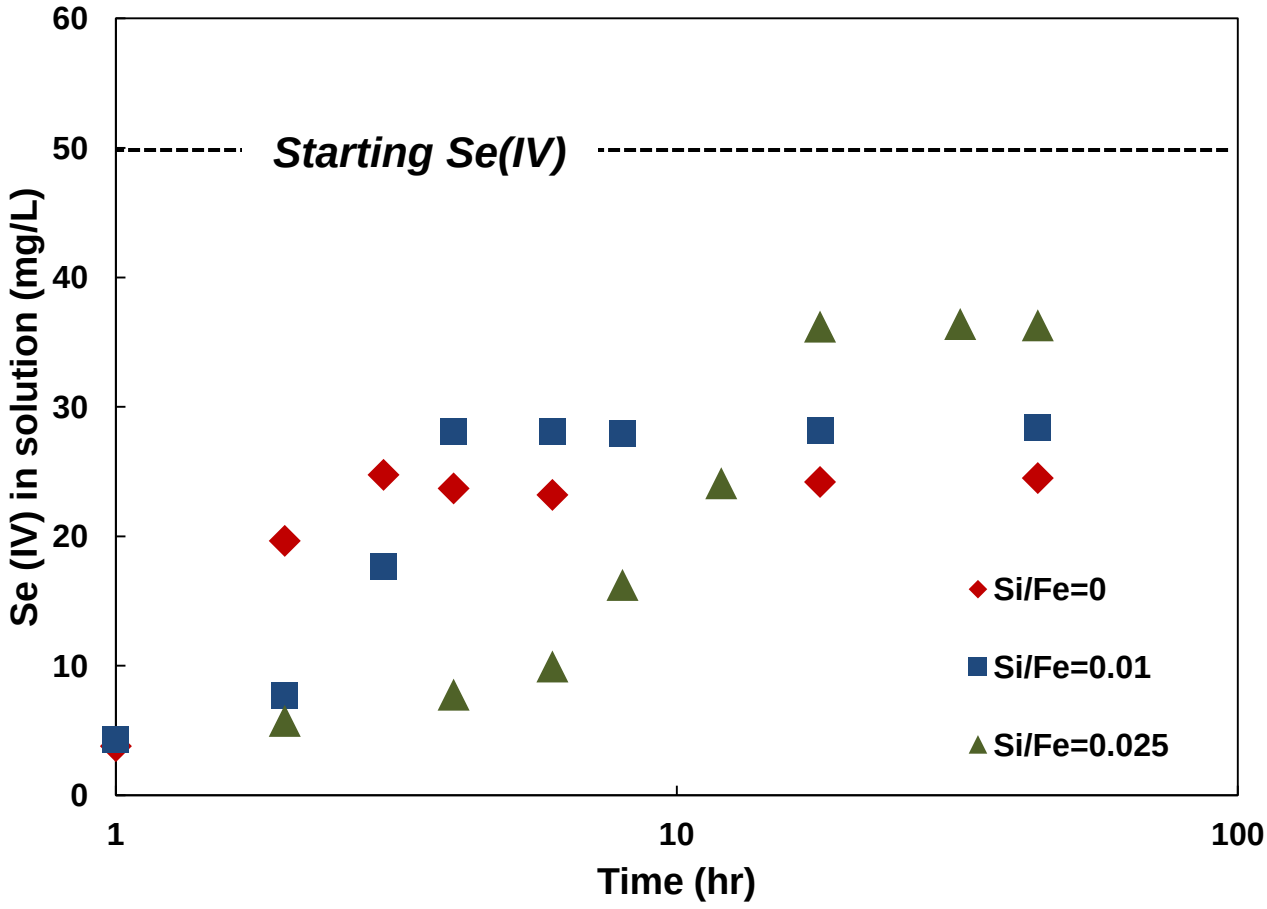

Fig. 2. Concentration of Se(IV) in bulk solution in contact with the solid. During transformation of ferrihydrite, Se(IV) concentration increases, indicating the release of Se(IV) back into solution. With increasing Si/Fe, the release becomes slower, but the released Se(IV) is also higher.

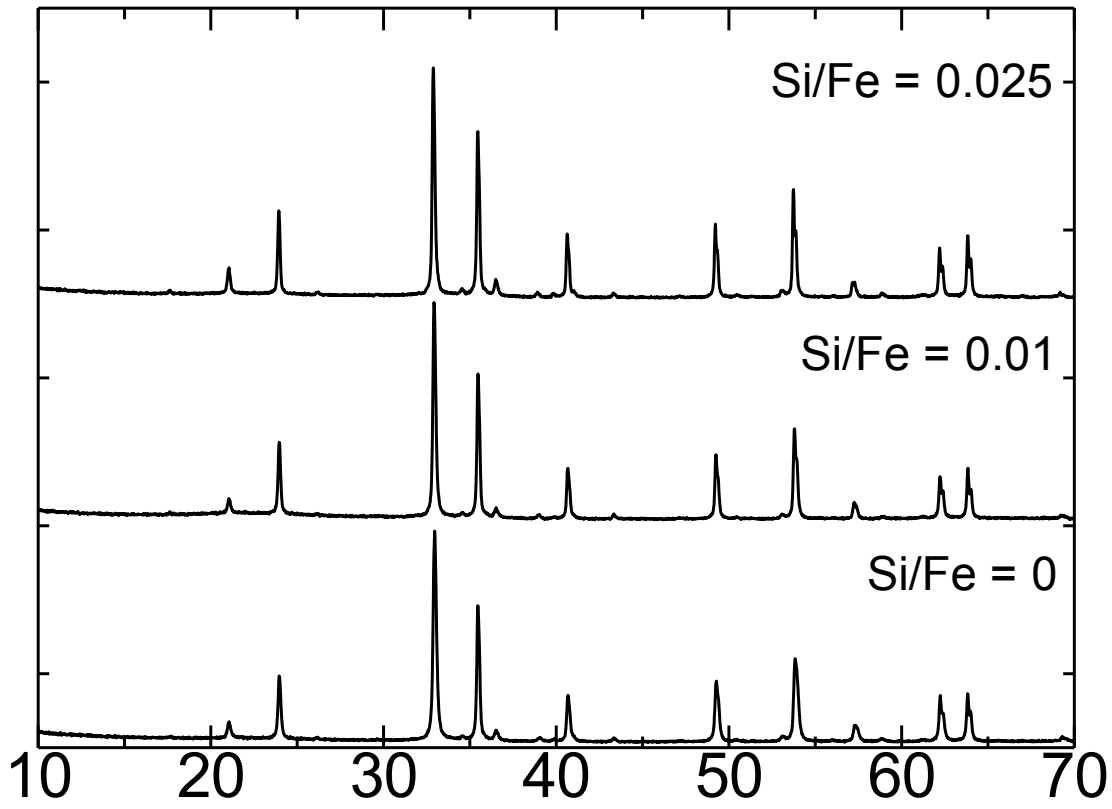

Fig. 3. XRD patterns of the crystalline, post-transformation solids formed in the presence of varying Si/Fe ratios.

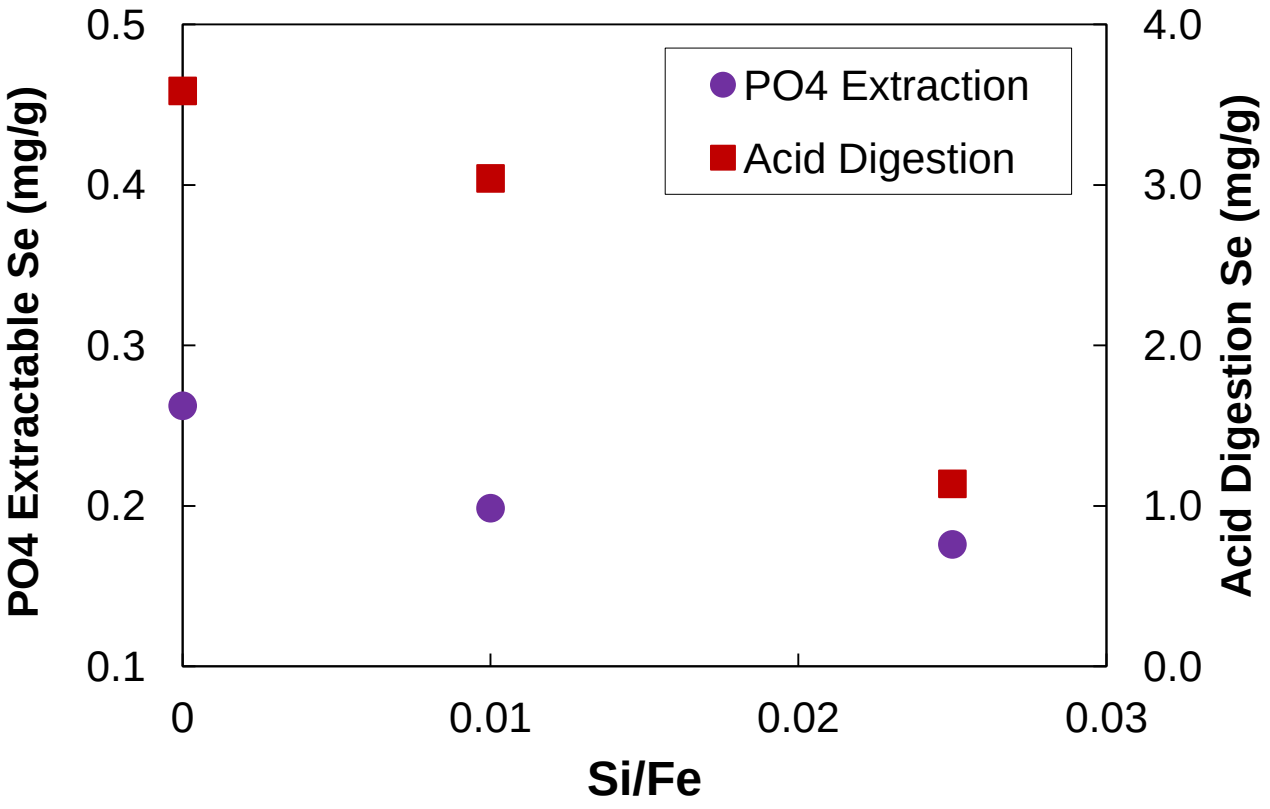

Fig. 4. Partitioning of Se(IV) in the crystalline phases. A significant percentage of Se(IV) retained in the solid can only be extracted by acid dissolution, although a small amount is present as phosphate-extractable, surface-bound species. Both forms of Se(IV) decrease with increasing Si/Fe.

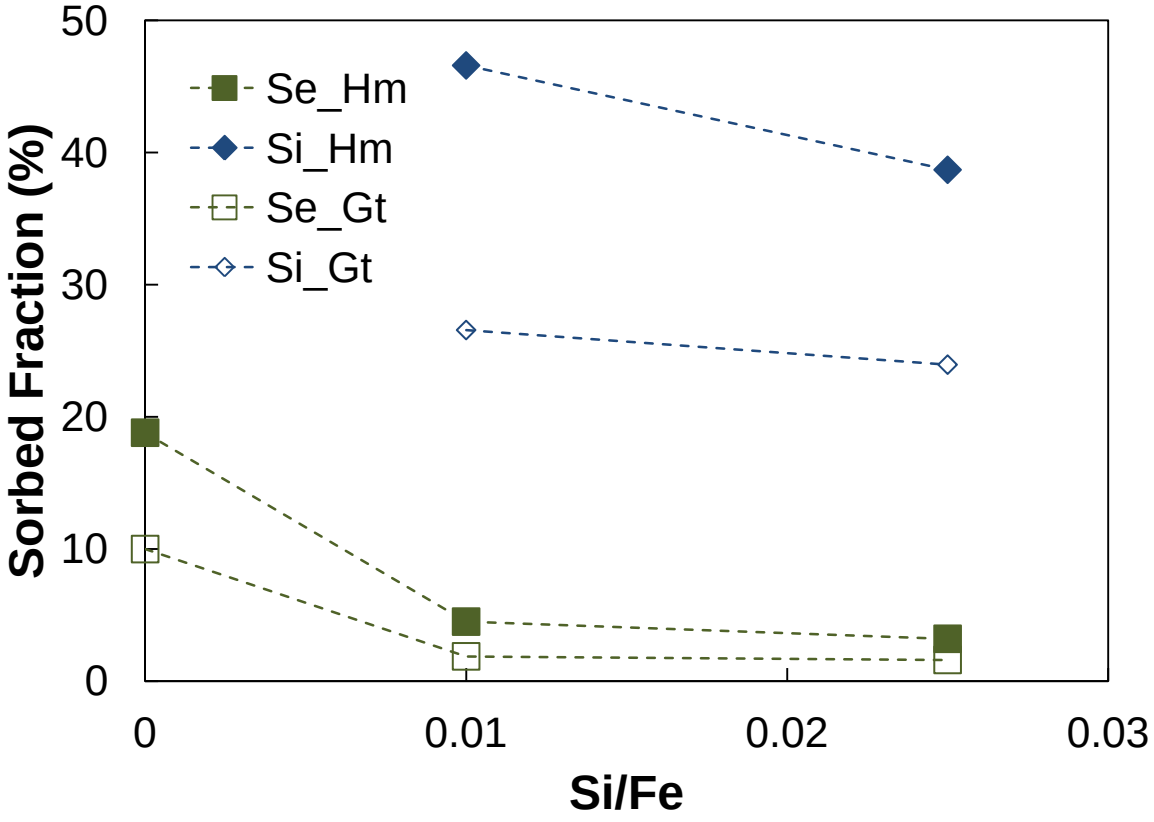

Fig. 5. Percentage of adsorbed Si and Se(IV) on the surface of goethite and hematite calculated using surface complexation modeling. The percentage of adsorbed Se(IV) drastically decreases in the presence of Si, which is significantly adsorbed on the surface of both goethite and hematite.

CHAPTER 5: General Conclusions

5.1. Summary of Results

The research presented in this dissertation tackles the transformation behavior of iron (hydro)oxides under alkaline conditions in the presence of foreign elements. Due to the ubiquity and highly reactive nature of these phases, they exert significant control on the geochemical behavior of hazardous elements (e.g. As, Se, etc). However, an overlooked aspect of hazardous element retention on iron (hydro)oxides is the impact of phase transformation on the eventual and long-term fate of hazardous elements. Different transformation pathways (e.g. dissolution / re-precipitation vs. aggregation, solid-state transformation) may have competing impacts on the remobilization of hazardous elements. It is therefore important to understand the factors that influence phase transformation and to investigate their impacts on the mobility of hazardous elements.

In this work, the influence on iron (hydro)oxide transformation of one of the most important impurity found in natural environments, as well as in geological disposal systems, was first investigated in Chapter 3. The presence of Si, derived from weathering of silicate rocks (in the natural environment) or from the dissolution of glass (in geological disposal systems) is shown to slow down the transformation rates of amorphous, metastable ferrihydrite. Furthermore, Si influences the transformation pathway by inhibiting ferrihydrite dissolution, indirectly leading to the formation of hematite, instead of goethite. The delay in the transformation induced by the presence of Si presents interesting implications on the stabilization of iron (hydro)oxides and for their long-term utility as sinks for hazardous elements. Previous investigations have clearly

The mobility of Se(IV) was next investigated during transformation to clarify how elements that were previously taken up by iron (hydro)oxides behave during phase transformation. Se(IV) is of particular interest due to its presence in high-level radioactive wastes (as ^{79}Se). Current

predictions of Se dose rates during the repository lifetime do not account for the sorption of Se onto potential sinks such as steel corrosion products and their eventual remobilization if these sorption substrates transform into thermodynamically stable phases. Results of the transformation experiments clearly show the remobilization of a fraction of Se(IV) during phase transformation. The release can be attributed to the dissolution pathway that resulted to the formation of goethite. Interestingly, depending on the pH, a fraction of the Se was retained, possibly locked between aggregates of crystalline phases. These results may suggest that during the lifetime of repositories, there may be a sudden spike in dose rates, corresponding to the liberation of Se from sorption substrates during phase transformation. Therefore, it is important to account for phase transformation in predicting the long-term behavior of hazardous elements both in nature and in engineered environments.

The results presented in Chapter 3 necessitates the understanding of factors that may contribute to the stabilization of iron (hydro)oxides, so that they can maintain their immobilizing control on hazardous elements. As seen in Chapter 2, the presence of Si greatly retards the transformation of ferrihydrite into crystalline phases. Specifically, Si passivates the surface of ferrihydrite against dissolution. The inhibition of the dissolution pathway, could delay the remobilization of Se during phase transformation. Indeed, as seen from the results presented in Chapter 4, Se(IV) was released more gradually in the presence of increasing amounts of Si. However, an interesting result is that less Se(IV) was actually retained during transformation in the presence of Si. Thus, while Si has the positive impact of retarding the remobilization of Se(IV), it also has the undesired effect of decreasing the retention capacity of crystalline phases for Se(IV). This can be attributed to the strong competitive effect of Si against other ions for sorption sites.

5.2. Implications

The results described in Chapter 4 present interesting problems for the mobility of hazardous elements in environments that are rich in Si. For example, at the interface of dissolving glass and steel in geological disposal systems for high-level wastes, the abundance of Si may lead to stabilization of sorption substrates in the steel corrosion products but at the same time, lead to the release of more amounts of hazardous elements. Furthermore, in the host rock, typically clays or crystalline igneous rocks, Si may inhibit the sorption of Se that may escape the near-field environment. These complex processes must therefore be taken into account in building predictive models for the long-term behavior of radionuclides of interest.

The insights obtained from the behavior of Se(IV) during iron (hydro)oxide transformation and the effects of Si can be useful in understanding the behavior of nutrients or other contaminants in natural environments. For example, in soils, the transformation of Si-stabilized ferrihydrite may prevent immobilized contaminants from being released to the biosphere. In streams, aqueous contaminants may adsorb onto suspended particles such as poorly crystalline iron (hydro)oxides, which may then aggregate and settle at the bottom of the stream. The presence of Si may stabilize such suspended particles and prevent remobilization of contaminants downstream.

Though the information on the behavior of Se(IV) presented in this work is useful in formulating predictive models an important, and challenging limitation is scaling up experimental observations to actual conditions. This may be a direction for future research. In particular, the levels of Si investigated here are significantly lower than the ones expected in actual repository conditions or in the natural environment. Thus, the reaction rates observed in this study are markedly faster (and timescales shorter) than what would be expected in actual conditions. However, information gathered in this study is useful in understanding the mechanisms involved. Thus, it can be expected that if the Si concentrations were scaled up, the trends observed in this study would become more pronounced. Other issues that will need to be addressed in the future is the exact retention mechanism of Se(IV) in the crystalline phases. This may be resolved by more advanced spectroscopic techniques.